Flexible Thin Films on Textiles for Solar Cells

Adel G Abdussalam Diyaf

Submitted for the degree of Doctor of Philosophy

Heriot-Watt University

School of Engineering & Physical Sciences

February 2014

ABSTRACT

In recent years, there has been an increase in studies about developing photovoltaic fabrics which can be used in different textile and clothing applications. The flexibility of the solar cells could be useful in many applications, for example providing power for small portable electronic devices such as personal digital assistants or on a larger scale for sunshades and canopies. In this work, we have taken the direct approach to deposit amorphous silicon cells directly onto fabrics. To achieve that, we have studied approaches to obtaining flexible conductive surfaces on polyester fabrics by using a double layer of metal and commercially available conductive polymer. Then both single and stacked metal contact layers and thin amorphous silicon films were built on glass and flexible substrates for optical and electric characterisation. It was shown by bending tests that the conductive fabrics retain both flexibility and electrical conductivity. Finally, complete n-i-p single junction a-Si:H cells were fabricated on different types of substrates such as glasses, polyester fabric and polytetrafluoroethylene fabric (PTFE). Several challenging aspects related to the fabrication and characterisation of solar cells on fabrics are highlighted. Cells on woven fabrics were shown to be active photovoltaic devices though with lower response than equivalent cells on rigid glass substrates.

ACKNOWLEDGMENT

*I would like to thank my supervisor **John IB Wilson**, **Robert Mather** and **Helena Lind** for their help, guidance and friendship during my study. Big thanks to **my family** especially **my wife** for their patience, continued support and encouragement during these years.*

Adel G Diyaf
Edinburgh, March 2014

ACADEMIC REGISTRY

Research Thesis Submission

Name*:*	Adel G Abdussalam Diyaf		
School/PGI:	EPS		
Version: *(i.e. First, Resubmission, Final)*	Final	Degree Sought (Award **and** Subject area)	PhD in physics

Declaration

In accordance with the appropriate regulations I hereby submit my thesis and I declare that:

1) the thesis embodies the results of my own work and has been composed by myself
2) where appropriate, I have made acknowledgement of the work of others and have made reference to work carried out in collaboration with other persons
3) the thesis is the correct version of the thesis for submission and is the same version as any electronic versions submitted*.
4) my thesis for the award referred to, deposited in the Heriot-Watt University Library, should be made available for loan or photocopying and be available via the Institutional Repository, subject to such conditions as the Librarian may require
5) I understand that as a student of the University I am required to abide by the Regulations of the University and to conform to its discipline.

* *Please note that it is the responsibility of the candidate to ensure that the correct version of the thesis is submitted.*

Signature of Candidate*:*		Date:	

Submission

Submitted By *(name in capitals):*	
Signature of Individual Submitting:	
Date Submitted:	

For Completion in the Student Service Centre (SSC)

Received in the SSC by *(name in capitals):*			
Method of Submission *(Handed in to SSC; posted through internal/external mail):*			
*E-thesis Submitted (**mandatory for final theses)***			
Signature:		Date:	

Please note this form should bound into the submitted thesis.

Updated February 2008, November 2008, February 2009, January 2011

TABLE OF CONTENTS

LISTS OF FIGURES AND TABLES

FIGURES

Chapter 1 Introduction

Chapter 2 Thin film silicon

Chapter 3 Experimental techniques and deposition methods

Chapter 4 . Contacts on polyester textile as a flexible substrate for solar cell

Chapter 5 Characterisation of solar cell layers

Chapter 6 Functional solar cells

TABLES

Chapter 1. Introduction

1.1 Silicon thin film solar cells

Worldwide concern about the security of energy supply increases continuously and due to the environmental problems of fossil fuel, renewable energies such as solar energy and wind energy are catching much more attention than ever before. Among these are photovoltaic devices based on silicon which directly convert sunlight to electric power. Although silicon is the most abundant natural element in the Earth's crust, it still brings new challenges. Usually extracted from silicates and oxides, it can be prepared in crystalline or amorphous form. Crystalline silicon (c-Si) is an indirect semiconductor with band gap energy around 1.12eV. It can be grown in cylindrical shape using different techniques such as Czochralski and Float Zone and then cut in circular or square wafers of various limited diameters and thickness depending on the applications [1]. Silicon wafer based solar cells dominate the PV markets with around 90% market share [2]. This leads to increased c-Si demand and as a consequence, there is a shortage in the crystalline form[3]. The industrial module efficiency for c-Si is about 25% at best [4]. On the other hand, there is thin film based technology which is built on thin hydrogenated silicon layers such as amorphous and microcrystalline silicon (a-Si:H and μc-Si:H). The amorphous silicon deposited as large area thin film uses low temperature plasma assisted methods where the main source of silicon is silane (SiH_4) or disilane (Si_2H_6). N-type and P-type doped thin film can be achieved by adding phosphine (PH_3) or diborane (B_2H_6) respectively. Because of its amorphous nature, a-Si:H material behaves as a direct semiconductor and has band gap varying between 1.7 eV and 1.9 eV, depending on deposition conditions. But so far efficiency of only 13.4% has been achieved by amorphous silicon cell [4]. The situation is partially improved by the presence of hydrogen atoms during the deposition process where the hydrogen atoms can share their electrons with the silicon, thus reducing the defects by passivating the unattached, dangling bonds. This may lead to form a crystalline phase within the amorphous tissue.

Amorphous silicon can be combined with elements such as germanium, oxygen, carbon and tin to form material with a band gap either above or below the one of pure amorphous silicon [5, 6]. Further, that opens the door to use a-Si:H in a variety of structures such as thin-film silicon multi-junction solar cells where it can be used as absorber, window or intermediate layer.

Thin film silicon solar cells can be fabricated on flexible substrates such as metallic or plastic foils [7, 8].

1.2 Flexible solar cells

Flexible substrates allow a reduction in cost when compared to transparent conductive oxide (TCO) coated iron-free glass, normally used as substrate coupled with the possibility of roll-to-roll deposition which could also lower production costs. Moreover, use of a lightweight and flexible substrate also allows a reduction in transport costs and broadens the range of applications where the use of rigid substrates would not be possible [9, 10]. Amorphous silicon (a-Si:H) has been successfully deposited onto different types of flexible substrate such as stainless steel and plastic sheets with roll-to-roll technique.

Organic solar cells can be used to produce flexible photovoltaic textiles in any scale from fibres to fabrics [11]. Organic thin film configurations can be deposited concentrically around the cylindrical surface of a fibre substrate by growth from solution or vapour phase and then coated with a conductive transparent electrode to form fibre-based PV cells. Figure (1.1a) shows a schematic of this device [12, 13]. Another approach is to build a solar cell configuration onto an optical fibre as a covering and then illuminate the fibre end. The light is then partially scattered sideways through the fibre to reach the coating as shown in figure (1.1b)[14]. These types of solar cells are called flexible fibre-shaped solar cells (FFSCs) [12].

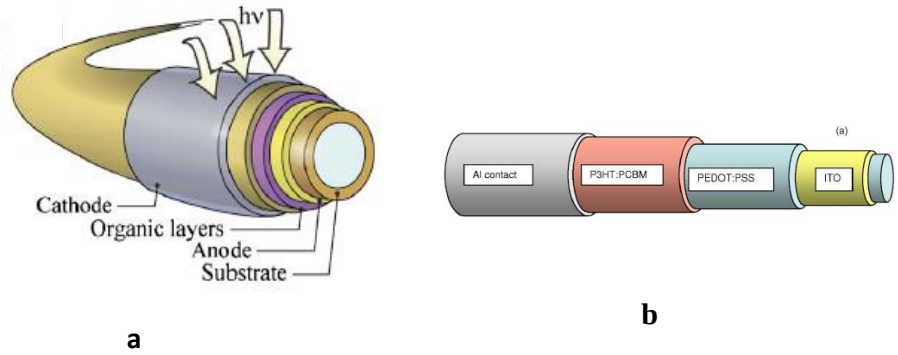

Figure 1.1 (a) Fibre-based PV cells [13]. (b) Solar cells on optical fibre[14].

In order to use these types of solar cells, there is need to develop woven cells with large area instead of the single fibre cell. So PV coated cotton fibres may be embroidered parallel to one another into cotton cloth leaving around 90% of the fabric exposed on one side. Alternatively, the PV fibres can be woven into fabrics as shown in Figure 1.2 [15].

However there are many disadvantages of the fibre based solar cells such as the weak adhesion between substrate and functional layers of the solar cells. Also the cells can crack during weaving and fabrication processes may lead to high electrical resistance [12, 16].

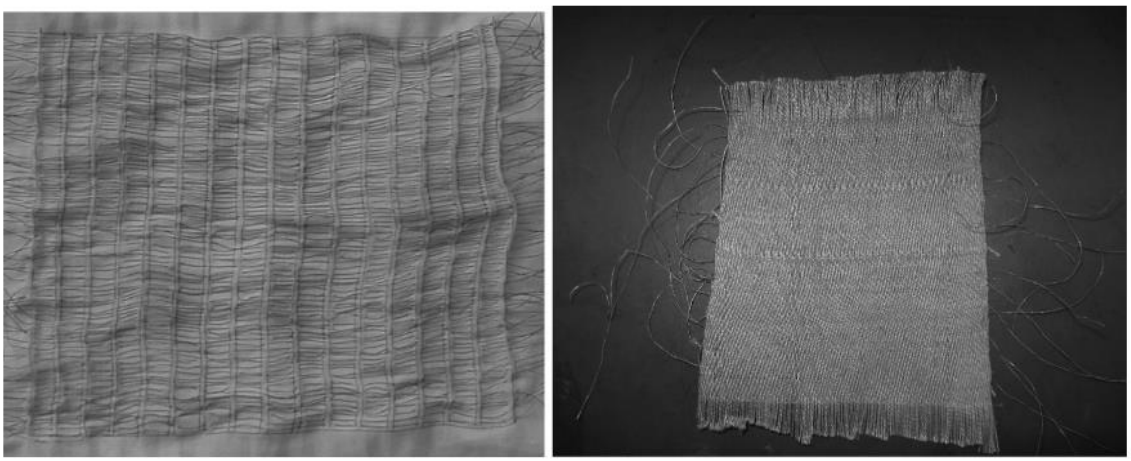

Figure 1.2. (a) PV fibres embroidered into cotton cloth (b) PV wires woven with textile thread [15].

In contrast to this arrangement, because of the possibility of depositing amorphous silicon onto different materials by low temperature plasma assisted methods, we are attempting to deposit amorphous silicon (a-Si) cells onto woven fabric. This can be done not by bonding or laminating conventional crystalline cells as is commonly done, but instead by directly depositing the cell layers on to the fabric itself. Flexible fabrics used as a substrate were coated with a conductive film to form back contacts and then n-i-p amorphous silicon cells were formed by the plasma enhanced chemical vapour deposition PECVD process. Transparent conductive oxide (TCO) film was used as a top contact. The target solar cell stack structure is shown in Figure 1.3.

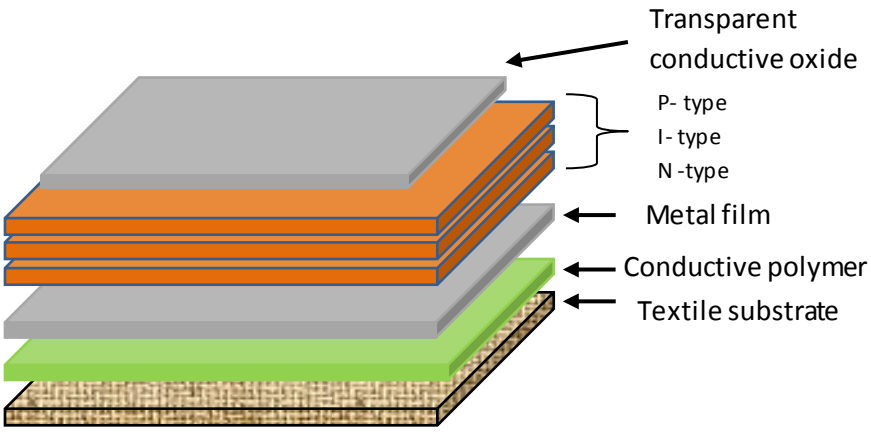

Figure 1.3. Schematic diagram of single junction PV cell deposited onto textile fabric.

1.3 Objectives and research plan

The aim of the research described in this thesis is to examine the possibility of building functional amorphous silicon solar cells directly onto textile. To achieve that target we:

- Study the electrical and optical properties of evaporated metal, which will be used to form back contacts together with sputtered TCO films for front contacts.
- Discuss the influence of the deposition conditions leading to the growth of the most suitable structure of sputtered TCO.
- Study the possibilities to obtain conductive surfaces on polyester fabrics by using one of two types of commercially available conductive polymers.
- Examine the electrical and optical properties of a-Si:H films individually in order to optimise their performance by adjusting the deposition conditions.
- Investigate the possibility of depositing amorphous silicon layers directly onto textile in comparison with glass substrates.
- Examine the performance of the solar cells on textile and glass substrates under solar simulator conditions.

Figure 1.4 illustrates the research work being carried out in this thesis. Alongside the cells on woven PTFE and polyester fabrics, the solar cell configuration was built on glass substrate so the functional properties of the latter can be used as reference. The performance of each element of the cell can be improved by monitoring the properties of the sample in each stage of the process.

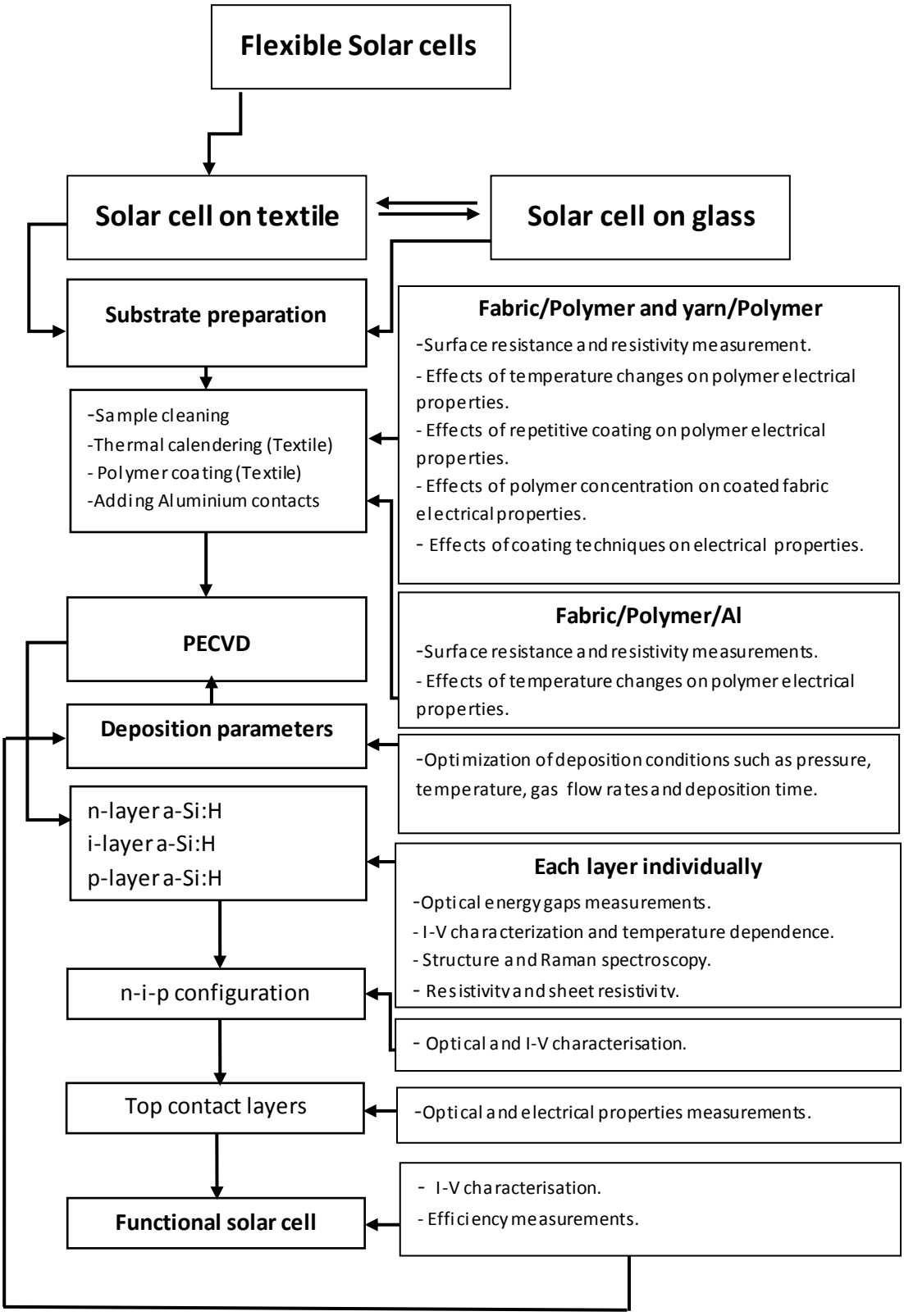

Figure 1.4. The research work being carried out in this thesis.

1.4 Outline of the thesis

Following this brief introduction, we move on to *chapter two* beginning with an overview of the history of amorphous and nanocrystalline hydrogenated silicon and the basic properties of the thin film silicon, including atomic structure, electronic structure, growth mechanisms and doping. The plasma-enhanced chemical vapour deposition techniques are presented. *Chapter three* briefly presents deposition techniques for all the thin film layers and characterisation setups used in this work. In *chapter four* we discuss the approaches to obtaining conductive surfaces on polyester fabrics by using commercially available conductive polymers, polyaniline and PEDOT: PSS which may then be coated with aluminium by vacuum deposition. We aim to use these surfaces as a back contact for solar cells (or other applications). In the first part of *Chapter five*, the types of substrates and cleaning procedure are briefly discussed. Then optical and electrical properties of metal and transparent conductive oxide contacts are reported. Finally, studies of intrinsic and doped layers of hydrogenated amorphous silicon forms the active solar cell in terms of electrical and optical properties as well as deposition conditions are presented. *Chapter six* describes fabrication of an n-i-p single junction a-Si:H cell onto different types of substrates, glass, polyester fabric and polytetrafluoroethylene fabric (PTFE). Then electrical performance of the complete solar cell is presented. Fabrication issues which have a major impact on the performance of the cells are discussed. Finally, a summary of this thesis is presented in *Chapter seven*. Future research directions based on this work are also suggested.

1.5 References

1. Colinge J-P and Colinge CA. *Physics of Semiconductor Devices*. New York: Springer; 2006.

2. Green MA. *Solar cells: Operating principles, Technology and system Applications*. New Jersey: Prentice-Hall; 1982.

3. Woditsch, P. and Koch, W., Solar grade silicon feedstock supply for PV industry. Solar Energy Materials and Solar Cells, 2002. 72(1–4): p. 11-26.

4. NREL. *Best research-cell efficiencies*. 2013; Available from: http://www.nrel.gov/.

5. Buehlmann P, Bailat J, Dominé D, Billet A, Meillaud F, Feltrin A, and Ballif C. *In situ silicon oxide based intermediate reflector for thin-film silicon micromorph solar cells*. Applied Physics Letters. 2007;91(14).

6. Chen T, Yang D, Carius R, and Finger F. *Aluminum doped silicon carbide thin films prepared by hot-wire CVD: Influence of the substrate temperature on material properties*. Thin Solid Films. 2011 May 1, 2011;519:4516-8.

7. Söderström T, Haug F-J, Terrazzoni-Daudrix V, and Ballif C. *Flexible micromorph tandem a-Si/μc-Si solar cells*. Journal of Applied Physics. 2010;107(1).

8. Söderström T, Haug F-J, Terrazzoni-Daudrix V, and Ballif C. *Optimization of amorphous silicon thin film solar cells for flexible photovoltaics*. Journal of Applied Physics. 2008;103(11).

9. Izu M, and Ellison T. *Roll-to-roll manufacturing of amorphous silicon alloy solar cells with in situ cell performance diagnostics*. Solar Energy Materials and Solar Cells. 2003;78(1–4):613-26.

10. Izu M, and Ovshinsky SR. *Roll-to-roll plasma deposition machine for the production of tandem amorphous silicon alloy solar cells*. Thin Solid Films. 1984;119(1):55-8.

11. Schubert MB, and Werner JH. *Flexible solar cells for clothing*. Materials Today. 2006;9(6):42-50.

12. Zou D, Wang D, Chu Z, Lv Z, and Fan X. *Fiber-shaped flexible solar cells*. Coordination Chemistry Reviews. 2010;254(9–10):1169-78.

13. O'Connor B, Pipe KP, and Shtein M. *Fiber based organic photovoltaic devices*. Applied Physics Letters. 2008;92(19).

14. Liu J, Namboothiry MAG, and Carroll DL. *Fiber-based architectures for organic photovoltaics*. Applied Physics Letters. 2007;90(6).

15. Lee MR, Eckert RD, Forberich K, Dennler G, Brabec C, Gaudiana RA, Calvert P, and Agrawal A. *Optical and Electronic Properties of Organic Photovoltaic Wires and Fabrics*. Journal of Macromolecular Science, Part A. 2009 2009/10/30;46(12):1238-46.
16. Wang H, Liu Y, Huang H, Zhong M, Shen H, Wang Y, and Yang H. *Low resistance dye-sensitized solar cells based on all-titanium substrates using wires and sheets*. Applied Surface Science. 2009;255(22):9020-5.

Chapter 2. Thin film silicon

2.1 Brief historical overview

Silicon is a material which may be obtained in a variety of solid forms, from its purest single crystalline phase, via a two-phase microcrystalline or nanocrystalline phase to disordered amorphous phase. By incorporating hydrogen into the network of the disordered phases to improve their electric and optical properties, each form of thin film material is a promising candidate for a wide range of applications. Hydrogenated silicon thin film thickness ranges from a few nanometers to several micrometers. The properties of the silicon thin films depend on their structure [1]. Among these films, Hydrogenated Amorphous Silicon (a-Si:H), and Hydrogenated nanocrystalline silicon (nc-Si:H) are reviewed below. Because hydrogenated nanocrystalline silicon (nc-Si:H) and hydrogenated microcrystalline silicon (uc-Si:H) are synonymous phases, differing in crystallite size (see Table below), all historical references for (uc-Si:H) will be identified as (nc-Si:H) [2].

Table2.1. Definition of various morphologies of thin film silicon material [1].

Identification	Abbreviation	Phases	Feature size
Hydrogenated Amorphous silicon	a-Si:H	Single phase amorphous	None
Hydrogenated nanocrystalline silicon	nc-Si:H	Two phase Amorphous and Crystalline (dual phase)	<20nm crystals
Hydrogenated Poly-crystalline silicon	Poly-Si:H	Single phase with grain boundaries	Up to 100nm

2.1.1 Hydrogenated Amorphous Silicon (a-Si:H)

Over the past 40 years there has been much research activity directed at amorphous silicon and its alloys. Sterling and Swann, 1965 were the first to report that they deposited silicon films from silane by using chemical vapour deposition promoted by R.F discharge [3]. The films were deposited on glass and other material substrates. Electron diffraction was used to indicate that their layer was amorphous and it showed extremely high resistivity, also as the film thickness increased the film lost its transparency. Although they expected that the preparation method would have a much wider application, they did not do any further measurement to assess their layers. Later, in 1969, Chittick and his colleagues used the same technique to deposit a-Si:H on glass from silane (SiH_4), and they found that when the layer was grown on glass substrate at room temperature the film is amorphous with short range order, and it had resistivity at 249K of about ($10^8\Omega$cm) which is too high for most devices. The amorphous layer had better photoconductive properties than that prepared by using vacuum evaporation and sputtering techniques. The silicon-hydrogen bonds were observed by using infrared vibration spectroscopy [4]. After that Spear and LeComber at University of Dundee, used a Chittick reactor and built amorphous layers which showed good electrical transport properties.

Furthermore, they managed successfully to dope (a-Si:H) both n-type and p-type by adding phosphine (PH_3) or diborane (B_2H_6) to the process gas mixture. This was significant because it was thought that a-Si:H could not be substitutionally doped [5]. Since then research on amorphous silicon has grown vastly and commercial activities in thin film transistors and solar cells are multi-billion dollar industries.

2.1.2 Hydrogenated nanocrystalline Silicon (nc-Si:H)

Between the fully amorphous hydrogenated silicon and polycrystalline silicon lies nanocrystalline hydrogenated silicon (nc-Si:H). It consists of grains of crystalline silicon with size of about 100 nm embedded in an amorphous silicon matrix [6].

In 1926 Günterschulze [7] sputtered As, Sb, and Bi by using glow discharge in hydrogen and in this work the source material was placed separately in a positive glow discharge column whereas in normal cathode sputtering method, the source should be connected with the cathode. In 1968 Veprek and Marecek used the same

idea to deposit the first hydrogenated nanocrystalline silicon (nc-Si:H) layers [8]. In their work, they have proved that the transport of silicon in low pressure hydrogen plasma takes place during deposition and the interaction is sustained by volatile hydrides of silicon which are formed as a result of the interaction between hydrogen plasma and silicon at 600^{o}C. This method is a special type of plasma-deposition technique, comprising chemical vapour transport and it offers a versatile approach for the study of the kinetics of the silicon-hydrogen system [9]. As a result of their work, they verified a possibility of Si and Ge hydrogen plasma transport, also the (nc-Si:H) layers are compact and well adhering to a glass substrate. The main advantage of that method is using pure silicon in low temperature, whereas the transport rate is small. Subsequently, Usui et al[10] investigated heavily doped silicon films prepared by plasma glow discharge decomposition of silane containing 10^{19}-10^{21} cm^{-3} phosphorus atoms. They reported that at the highest doping level the resistivity was found to be 0.01 Ω.cm at room temperature and the films had a microcrystalline structure rather than predominately amorphous phase [10]. After that, in 1983, Spear et al [11, 12] reported using radio frequency glow discharge to deposit (nc-Si:H) layers. Spear and his colleagues in 1983, confirmed the possibility of depositing (nc-Si:H) thin films directly in a glow discharge plasma although at a very low rate and also reported in some detail about the films in terms of electrical properties. The properties of the films are dependent on deposition parameters, such as gas flow rate, pressure, RF power level, doping gas ratio and substrate temperature.

Furthermore, films with different thickness show different properties even if they are deposited under the same conditions [10, 11]. Despite the huge research effort of hydrogenated nanocrystalline silicon films and devices are not fully understood and are open to further improvement.

2.2 Thin Film Physics

In this section, a brief overview of the structural and electronic properties of both a-Si:H and nc-Si:H is provided.

2.2.1 Crystalline silicon (c-Si) and amorphous silicon (a-Si)

Silicon is a group IV element semiconductors, which have diamond lattice structure where each atom has four nearest neighbours situated at the vertices of a tetrahedron. Crystalline silicon can be characterized by an array of silicon atoms that long range order. Each atom contributes four electrons in valence band, and it has an energy gap of about 1.1eV.

In contrast to c-Si, where the atoms are ordered in a periodic lattice, amorphous silicon (a-Si) lacks the long range order. Because of the absence of the periodicity in the amorphous network, it is much more difficult to determine the structure of the network and Bloch's theorem cannot be applied as in crystalline solids. The a-Si and the c-Si have the same number of bonding orbitals (3p4s). However, it was suggested that not all the bonds connect with the nearest neighbouring atoms, some of them are left dangling in the structure, see Figure 2.1 where A and B indicate dangling bonds.

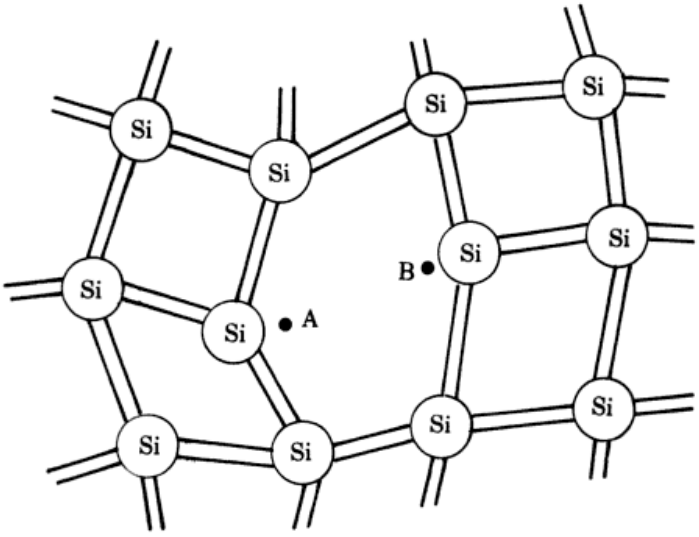

Figure 2.1. Disordered network of amorphous silicon [2].

The energy difference between the bonding and the anti-bonding orbital gives rise to the forbidden gap that indicated as a band gap. Figure 2.2 illustrates the density of states in c-Si and a-Si of the same conditions. In fact, the energies of the electronic states of a-Si are perturbed, causing the broadening of the bands in contrast to c-Si where the band edges are sharp. That deformation produces electronic states that can be characterized by exponentially varying valence and conduction band tails and the states associated with dangling bond defects lie near the middle of the gap. The band tail states have much lower carrier mobility than the extended states leading to a mobility gap. The dangling bond states lie in mid gap. Figure 2.3 illustrates a typical density-of-states (DOS) distribution for device-quality amorphous silicon. In the amorphous network, strained atomic bonds and dangling bonds act as traps for free electrons and holes, which is considered a drawback of pure amorphous silicon [2, 13].

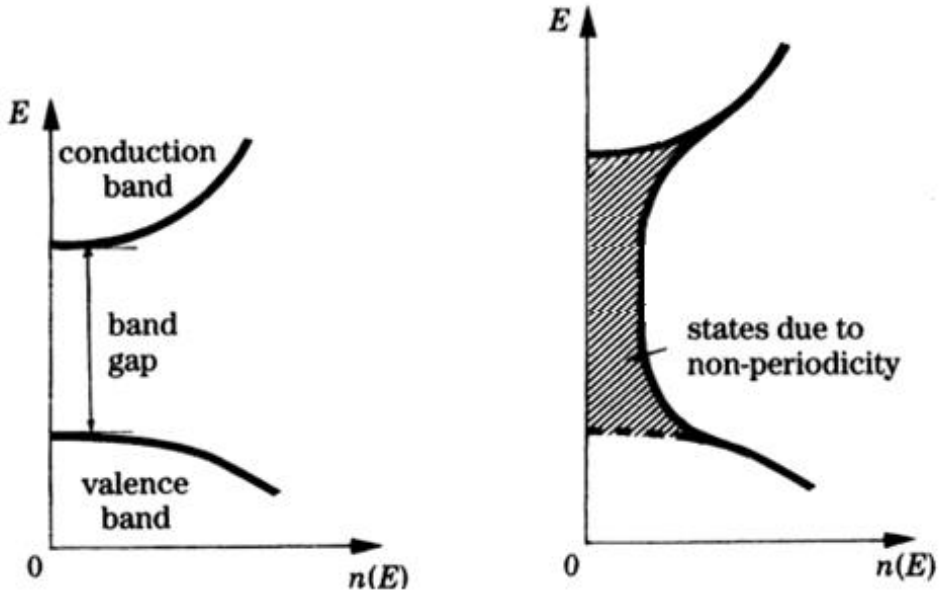

Figure 2.2. Density of states in crystalline (left) and amorphous material (right) of the same chemical composition [2].

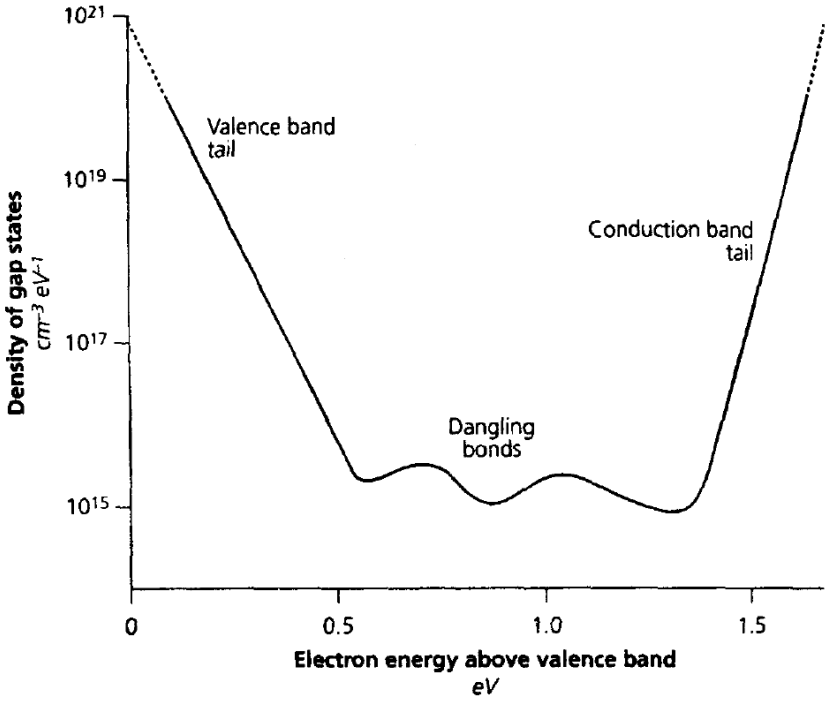

Figure 2.3. Density of electron states in the band gap of a-Si [14].

2.2.2 Hydrogen in amorphous silicon network

In 1974 Beyer and Stuke [15], Le Comber et al[16] and Lewis et al [17] realized that dangling bond states in a-Si can be passivated by bonding with hydrogen, which forms a strong Si-H bond, removing the defect state from the mobility gap. Moreover, hydrogen can insert into strained Si-Si bonds, forming Si-H bonds and relieving strain in the network. The incorporation of bonded hydrogen into a-Si can reduce the dangling bond density by several orders of magnitude, as shown in the density of states as determined by field effect measurements in Figure 2.4 [5, 18]. As a result the structure is relaxed and more ordered, also has sharper band tails and significantly lower density of dangling bond defects, improving the carrier concentration and the transport properties of the amorphous films [19].

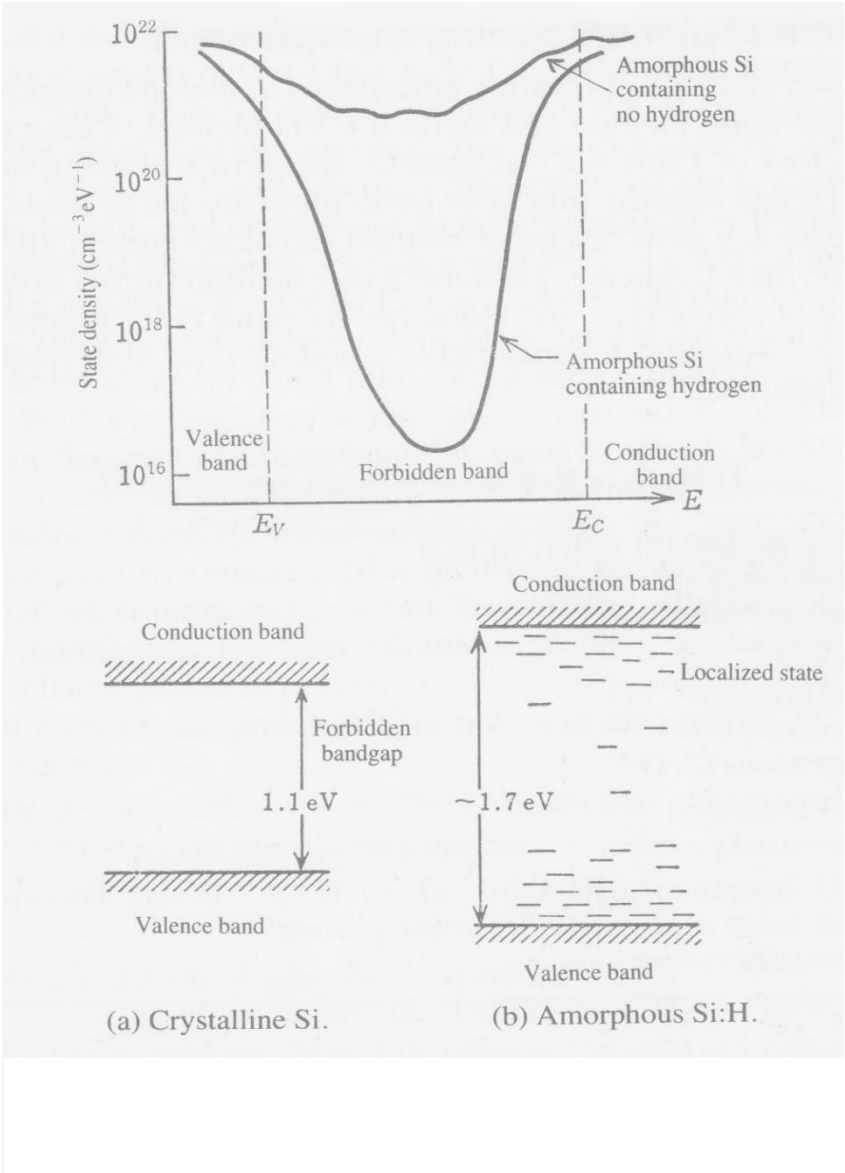

Figure 2.4. Hydrogen passivated mid-gap dangling bond defect states [20].

2.2.3 Hydrogenated nanocrystalline silicon (nc-Si:H)

Nanocrystalline hydrogenated silicon (nc-Si:H) is used as a general term for a mixed phase material consisting of varying amounts of c-Si nano-crystallites, a-Si:H tissue, cracks and voids[39]. In this part, the hydrogenated nanocrystalline silicon will be described in terms of its structure, properties and growth technique.

2.2.3.1 nc-Si:H microstructure

The structure of nc-Si:H can be described as a mixed-phase material of a-Si:H, embedded composed conglomerates of nanocrystallites. Figure 2.5 shows image of the nc-Si:H thin films, obtained by high resolution transmission electron microscopy (HRTEM). The nanostructural features of the nc-Si:H thin films can be discussed based on the variation in the chemical bonds between silicon and hydrogen. Figure 2.5 illustrates the nanocrystallites and the amorphous matrix in the nc-Si:H. Most of the hydrogen-silicon bonds are located at the surface of nc-Si:H thin films, and passivate the dangling bonds. The shape and size of the clusters are depending on the hydrogen content and the annealing condition [21].

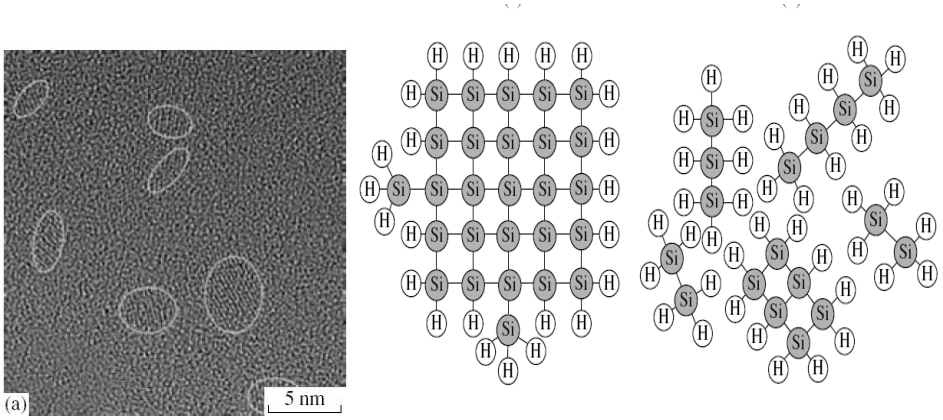

Figure 2.5. A silicon nanocrystallite in amorphous tissue [21].

2.2.3.2 nc-Si:H thin film growth

It is very important to understand the growth of nc-Si:H to predict the optimal conditions for obtaining nanocrystalline phase. There are many theories describing the mechanisms of nc-Si:H growth. According to Matsuda [22], there are three models of nc-Si:H growth: surface-diffusion model, etching model and chemical annealing model. In the Surface diffusion model, hydrogen atoms cover the film-growing surface and produce local heating as result of hydrogen exchange reactions, enhancing the surface diffusion of film precursors (SiH_3). These precursors adsorb on the surface, leading to the nucleus formation, finally epitaxial-like crystal growth takes place as shown in Figure 2.6. In the etching

model as shown in Figure 2.7, weak Si–Si bonds in the amorphous network are broken by atomic hydrogen provided on the film-growing surface. Each broken bond is replaced with a (SiH_3) precursor to create Si–Si and as result of that the crystalline structure forms in the network.

The last model is chemical annealing model which is proposed to explain a layer-by-layer growth of nc-Si:H . The amorphous phase changes to crystalline phase because of a large number of hydrogen atoms which are incorporated into the substrate. As a result of that, the amorphous network becomes more flexible. Figure 2.8 shows the chemical annealing model [22].

It is concluded that the surface diffusion model seems to be more logical than others and it is supported by experimental evidence, whereas the other models are insufficient to explain the formation process. In another study, Kondo et al [23] studied the film structure of nc-Si:H during deposition and they conclude that their result can be explained very well by assuming the surface diffusion growth model rather than the etching model.

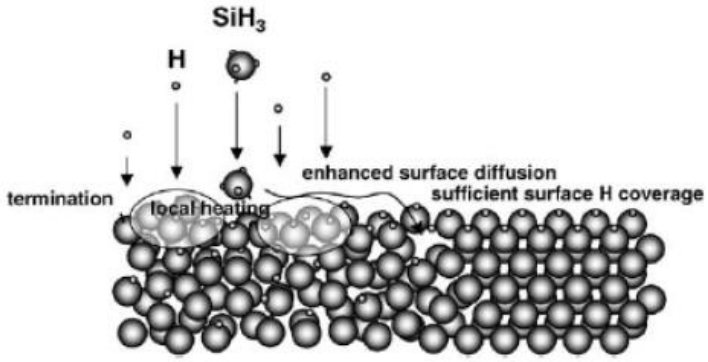

Figure2.6. Surface-diffusion model [22].

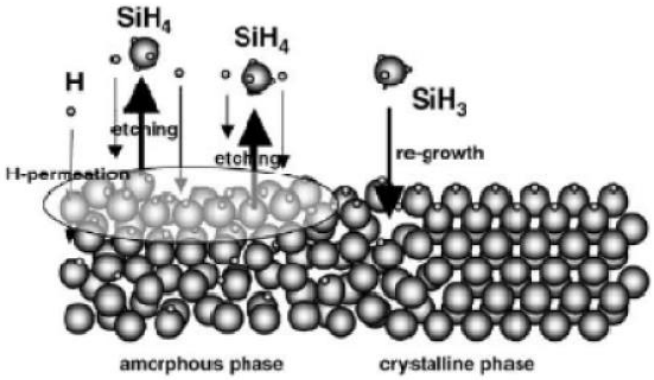

Figure 2.7. Etching model [22].

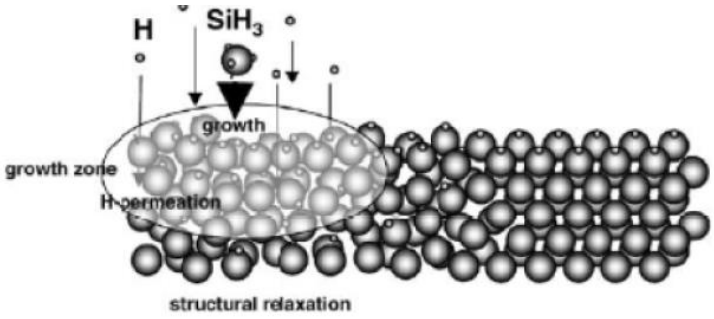

Figure 2.8. Chemical annealing model [22].

Typically nc-Si:H layers show inhomogeneity in the growth direction. During the growth, three phases can be seen; an amorphous hydrogenated silicon phase, a crystallize phase and a phase which includes some fraction of saturated crystals. Atomic hydrogen is believed to play an important role in structuring the Si-Si bonds towards a more crystallized matrix [24].

A common feature of all nc-Si:H deposition techniques is introducing hydrogen in order to control the material ranging from amorphous to highly crystallized nc-Si:H .

A wide variety of experiments such as X-ray diffraction and transmission electronic microscopy have been applied on nc-Si:H to get more information about its structure. As a result of those experiments, a schematic picture in Figure 2.9 is drawn and it illustrates the important structural features of

nanocrystalline silicon. It can be seen that there is a variety of material structure ranging from high crystalline volume fraction at the left side to complete amorphous structure at the other end. During the growth of the layer, the formation process starts with a nucleation phase which is strongly related to deposition conditions and also the substrate type. While increasing the film thickness, the diameter of columnar structures increases leading to conical shape. The columnar clusters have a diameter of about 200nm and are separated from each other by voids which allow impurities or atmospheric gases to diffuse along the column boundaries.

With decreasing crystalline volume fraction from left to right side in Figure 2.9, the columnar crystalline structure is interrupted and the amorphous contribution increases. This material is a transition phase between nanocrystalline and amorphous [25, 26].

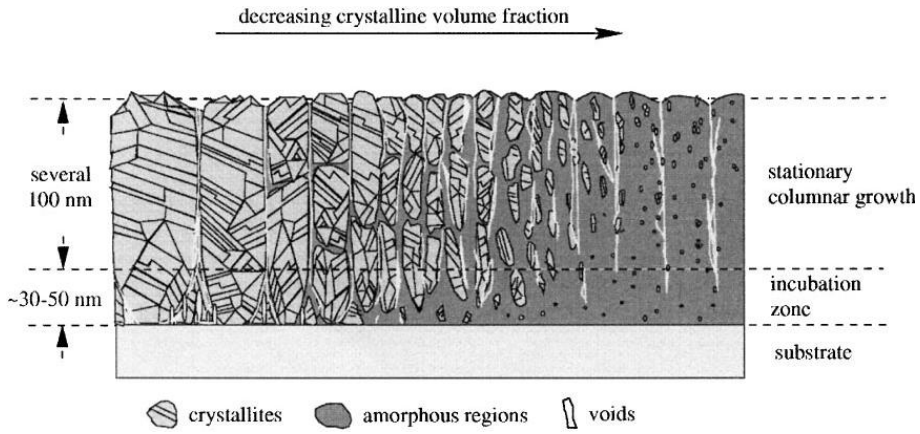

Figure 2.9. The important structural features of nanocrystalline silicon [25].

2.2.3.3 Density of defect states (DOS)

In order to obtain more insight into the electronic properties of nc-Si:H, it is important to determine the distribution of the trap states in the band gap. Shaw and Hack [27] presented an empirical density-of-states distribution model for amorphous silicon based on experimental evidence. In this model, the energy gap is broken into three parts. First part are deep states which are near midgap, and generally identified as dangling bond defects in the network. Second part are shallow states, also called tail states, which are below the mobility edge and attributed to disorder in amorphous networks due to compressed bonds. It is believed that the localized band tail states are monovalent, so they are occupied

by just one electron or hole. Last part is a linear transition region between donor and acceptor like states. The density of states in amorphous films varies continuously with energy.

The defects in nc-Si:H as well as in a-Si:H can be described as a typical density of defect states (DOS) distribution [27]. Figure 2.10 illustrates the (DOS) of an amorphous silicon material.

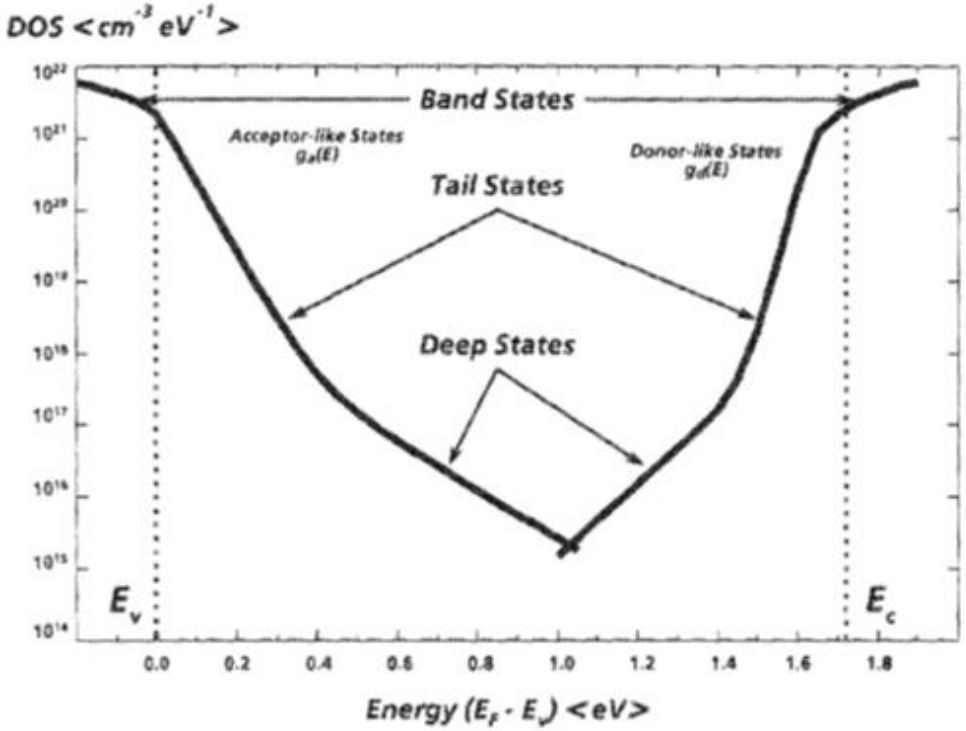

Figure 2.10. Density of states within the band gap of disordered materials [27].

2.2.3.4 Doping

Doping is used in order to manipulate the type of electrical conductivity by adding a controlled amount of impurity atoms. As in crystalline silicon, boron may be used for p-type and phosphorus for n-type doping.

Perhaps the first promising doping experiments were introduced by Chittick and his colleagues. Their experiment was carried out on amorphous silicon prepared by the glow discharge decomposition of silane and they found out that introducing phosphine to silane process gas could reduce the resistivity by a factor of 20 to 100 [4].

Later on, Spear and LeComber reported more thoroughly that amorphous silicon could be doped by addition of boron and phosphorus. This was a major

breakthrough in the field, since before they published their report, it was generally thought that a-Si:H could not be substitutionally doped. Their experiments were carried out on amorphous silicon and during the process they mixed the silicon source, silane (SiH_4), with phosphine (PH_3) or diborane (B_2H_6). As a result they found out that the conductivity of amorphous silicon increased by seven orders of magnitude, the conductivity activation energy decreased from about 0.7 eV in un-doped material to 0.15 eV in the phosphorus doped material and 0.3 eV in the boron doped material [5]. The effect of doping is shown in Figure 2.11.

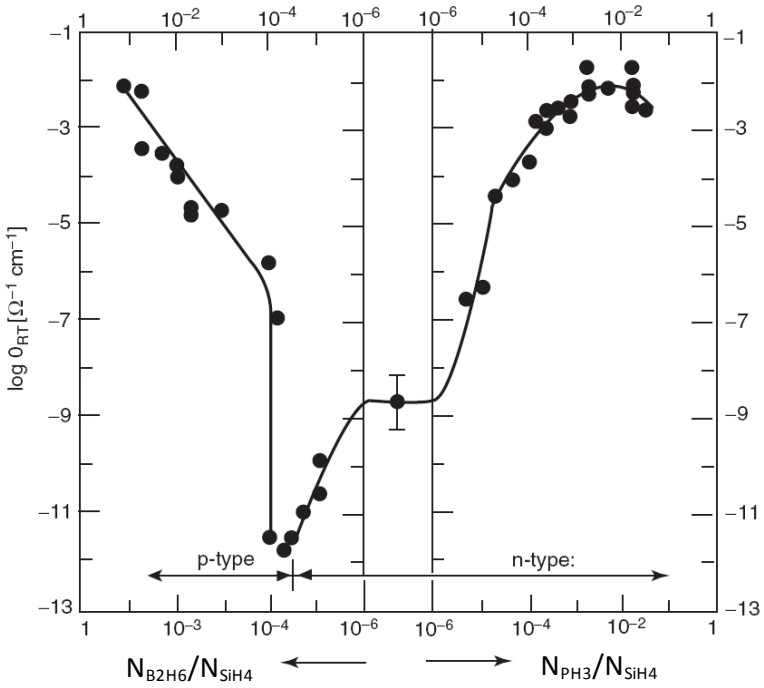

Figure 2.11. Room temperature conductivity of n and p-type amorphous silicon as a function of gaseous impurity ratio [5].

Doping the nc-Si:H not only improved the conductivity, but also affected the grain size and density. Many references reported that the structure and performance of the film can be changed by doping [28, 29]. With the increasing of the phosphorus content the grain size of the films decreases gradually and increases crystalline volume percentage whereas by increasing diborane content there is no obvious change in the grain size but the value of crystalline volume percentage is decreased [30].

2.2.3.5 Optical absorption and the optical band gap in thin- film silicon

The optical properties of thin- film are usually characterized by the absorption coefficient, the refractive index, and the value of the optical band gap.

The absorption coefficient occurs by transition of electrons and holes between filled and empty energy states such as those in conduction and valence bands. In some cases, because of strong phonon-electron coupling, self-trapping phenomenon can be seen. The optical absorption spectra of nc-Si:H, a-Si:H and c-Si are compared in Figure 2.12. As can be seen a-Si:H has the highest absorption coefficient and c-Si has the lowest, in the energy range E > 1.7eV [31].

Often the absorption spectra, which can be obtained by Constant Photocurrent Method (CPM), are used to obtain the optical band gap (E_g) and Urbach energy (E_o).

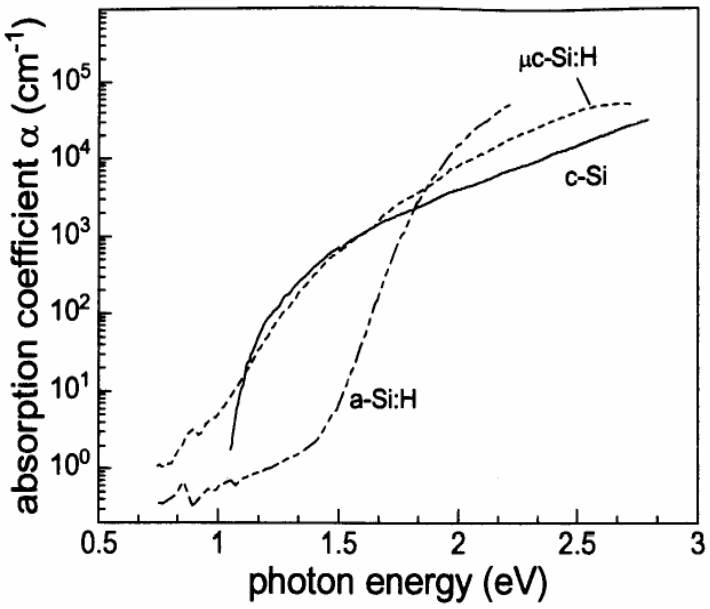

Figure 2.12. The absorption coefficients of c-Si, a-Si:H and nc-Si:H [31].

The typical absorption curves of amorphous materials can divided into three distinct regions A, B and C as illustrated in Figure 2.13. In the first region A, which has a small optical coefficient range, the optical absorption is controlled by the optical transition between defect states below E_f and conduction band. To some extent, Region A refers to density of defects in the material. In region B, the optical transition reflects the transitions from the localized tail states above

the valence band gap to extended states in the conduction band or the transition from extended states in the valence band to localized tail states below the conduction band. Thus it corresponds to a joint density of states. This region is called the Urbach edge and the absorption coefficient follows Urbach's rule:

$$\alpha = \alpha_0 \exp[(h\nu)/\Delta E] \qquad (2.1)$$

where ΔE is the Urbach width also called Urbach energy. By using above equation Urbach energy can be obtained from the plot of the absorption coefficient (α) versus photon energy ($h\nu$). Generally, the valance band tail is border than the conduction band and dominates ΔE.

In last region C, the absorption coefficient is due to transitions from extended to extended states and it is well described by Tauc's equation[40]:

$$\alpha h\upsilon = B(h\upsilon - E_{tauc})^m \qquad (2.2)$$

Where (α) is the absorption coefficient, B is constant proportional to the edge width parameter, $(h\upsilon)$ is the photon energy, and (E_{tauc}) is termed the optical band gap and usually used for defining the energy gap. The value of m depends on type of transition. The photon energy at which the absorption coefficient is about $10^{-4}cm^{-1}$ (E_{04}) is used the band gap in amorphous silicon.

For direct band gap, allowed transitions, an optical band gap can be obtained by plotting $(\alpha h\upsilon)^{1/2}$ versus photon energy [32]. Transmission data measured by photothermal deflection spectroscopy (PDS) technique.

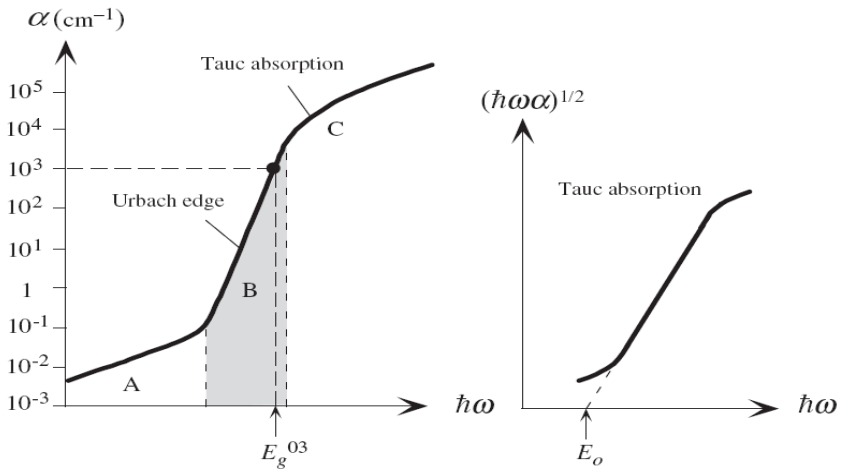

Figure 2.13. Typical spectral dependence of the optical absorption coefficient [32].

2.3 Thin film deposition techniques

Deposition of amorphous silicon thin films has been carried out via chemical vapour transport method [6], Plasma Enhanced Chemical Vapour Deposition (PECVD), Very High Frequency Plasma Enhanced Chemical Vapour Deposition (VHF PECVD) and Hot Wire CVD (HWCVD) [33, 34]. Compared to other methods, PECVD is widely used due to its high potential to prepare high quality material uniformly over large area substrates.

Industrial applications of plasma processes are mainly built on weakly ionized plasma discharges, which have the following properties: (***a***) the plasma is driven by electrical power, (***b***) the collisions between charged particles and neutral gas molecules are important, (***c***) there are boundaries at which surface losses are important, (***d***) ionization of neutrals sustains the plasma in the steady state and (***e***) electrons are not in thermal equilibrium with ions [35].

In this section we briefly review the fundamentals of PECVD and microwave plasmas.

2.3.1 Plasma Enhanced Chemical Vapour Deposition (PECVD)

Plasma enhanced chemical vapour deposition (PECVD) is also called glow discharge deposition, because of the light emitted by the excited species. Glow discharge can grow by inelastic electron impact processes, which start when electrons get enough energy. This energy can be provided by radio frequency (RF), very high frequency (VHF), and microwave frequency [33] fields.

In the case of radio frequency glow discharge, the plasma is driven by AC high frequency power supply, such type of plasma has a steady state discharge even with insulator coated electrodes. That means insulating layers such as glass, and polymers can be coated.

Figure 2.14 shows schematic diagram of a flat-bed or planar system in which the discharge occurs between two parallel plates. One of those plates is connected with RF generator through the impedance matching box which is used to couple the source power to the plasma to minimize the reflective power and ensure an optimal energy transfer to the discharge. The other electrode is usually connected to the ground [35].

Moreover, the specimen is attached to powered plate for etching purposes and to grounded plate for deposition. The grounded electrode is heated by a resistive heater coil.

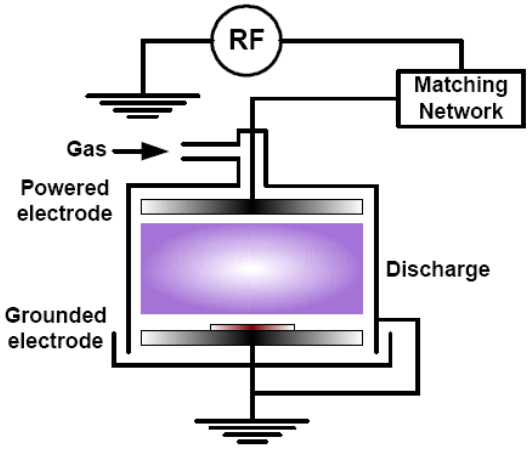

Figure 2.14. Shows schematic diagram of RF plasma reactor (After ref [35]).

The applied field, which is applied between two electrodes, accelerates electrons and ions within the plasma to high kinetic energy states. Because ions have a high mass they change their energy through collision processes with gas molecules. On the other hand, due to electrons' small mass they cannot share the energy gained from the electric field through elastic collisions with ions and other species, so electrons change their energy through inelastic collision such as excitation, dissociation and ionization. Plasma plays an important role to provide energy to help dissociation of silane. The dissociation starts by collisions with electrons which are accelerated by electric field. The rf plasma deposition can be described as a four steps process as shown in Figure 2.15 [36]:

1- As a primary reactions, SiH_4 molecules are decomposed by electron impact excitation and as a result of this reaction various neutral radicals, molecules, positive and negative ions, and electrons are generated.
2- As a second stage, those molecules, ions or radicals react together to form reactive species and may eventually form large silicon–hydrogen clusters. The reactive species move to the substrate surface where positive ions bombard the growing film, and negative ions are trapped within the plasma.

3- The third step is interaction of radicals with the surface of the growing film, such as radical diffusion, chemical bonding, and hydrogen sticking to the surface or abstraction from the surface.

4- The last step is subsurface release of hydrogen and relaxation of the silicon network.

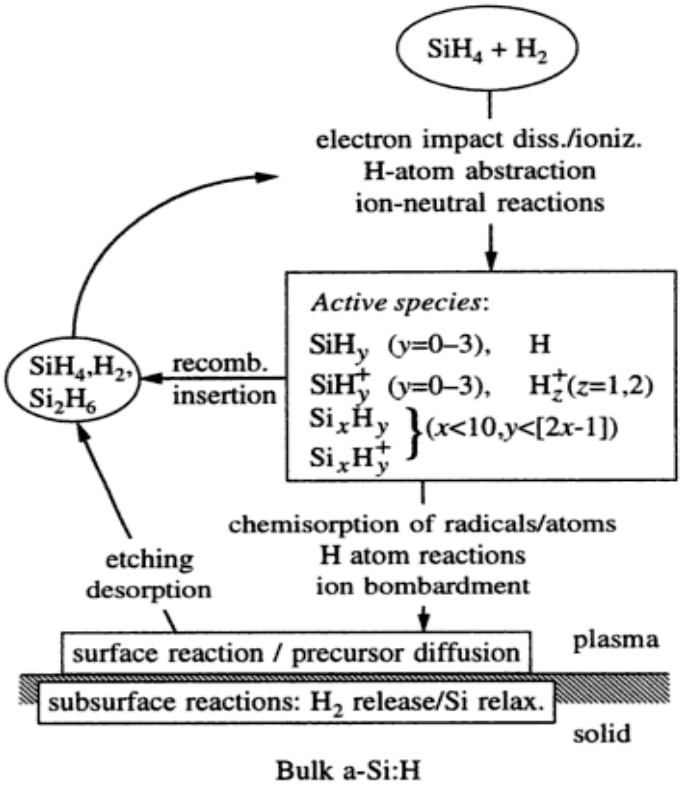

Figure 2.15. RF plasma deposition four steps process [36].

2.3.2 Microwave Chemical Vapour deposition

Microwave PECVD uses microwave radiation to initiate a plasma. In earlier researches, microwave discharge was produced by a discharge tube inside a waveguide or cavity at the location where the electric field is high.

Microwaves, at 2.45 GHz, are directed by the waveguide into the chamber where they excite the gas, forming a plasma above the substrate. The size of the plasma is controlled by some parameters such as the microwave power, and the gas pressure. As in rf plasma, the electron temperature is significantly higher than the atoms and molecules so the hot electrons interact with the gas creating the radicals needed for the deposition. The main difficulty with microwave systems is they are hard to scale up to coat large areas. Figure 2.16 illustrates

one type of Microwave Chemical Vapour Deposition system. The plasma system at Heriot-Watt University is provided with both RF and Microwave generators [37]. In this work we use the RF generator.

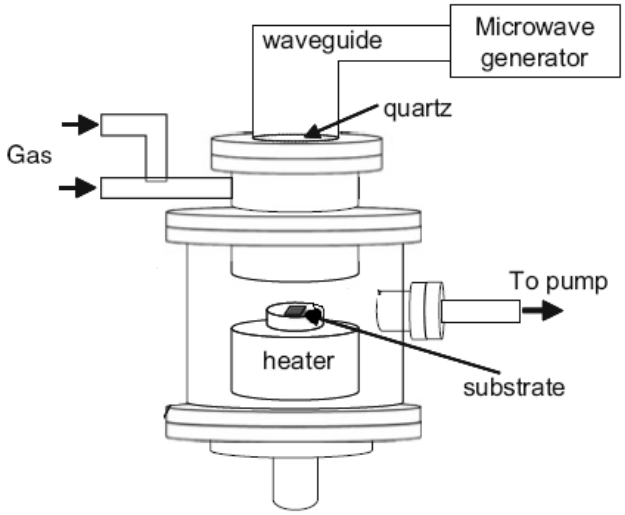

Figure 2.16. Schematic of Microwave Chemical Vapor deposition [38].

2.4 Conclusion

This chapter introduced a brief literature review on the history of thin film silicon. Then an overview of the structural and electronic properties of both a-Si:H and nc-Si:H is provided as well as a description of the thin film growth mechanism. Finally, thin film deposition techniques are presented.

Further experimental techniques used in this project are described in the next chapter.

2.5 References

1. Schropp REI, and Zeman M. *Amorphous and Microcrystalline Silicon Solar Cells: Modelling, Materials and Device Technology*: Norwell, MA: Kluwer Academic Publishers; 1998.

2. Bernard S, and C H. *Physics of Semiconductors*. New York: Springer Verlag; 1993.

3. Sterling HF, and Swann RCG. *Chemical vapour deposition promoted by r.f. discharge*. Solid-State Electronics. 1965;8(8):653-4.

4. Chittick RC, Alexander JH, andSterling HF. *The Preparation and Properties of Amorphous Silicon*. Journal of The Electrochemical Society. 1969 January 1, 1969;116(1):77-81.

5. Spear WE, andLe Comber PG. *Substitutional doping of amorphous silicon*. Solid State Communications. 1975;17(9):1193-6.

6. Wagner S. *Amorphous silicon: Vehicle and test bed for large-area electronics*. physica status solidi (a). 2010;207(3):501-9.

7. Gunterschulze A. Physik. 1926;36:683.

8. Vepřek S, and Mareček V. *The preparation of thin layers of Ge and Si by chemical hydrogen plasma transport*. Solid-State Electronics. 1968;11(7):683-4.

9. Webb AP, and Vepřek S. *Recativity of solid silicon with hydrogen under conditions of a low pressure plasma*. Chemical Physics Letters. 1979;62(1):173-7.

10. Usui S, and Kikuchi M. *Properties of heavily doped GD・Si with low resistivity*. Journal of Non-Crystalline Solids. 1979;34(1):1-11.

11. Lecomber PG, Willeke G, and Spear WE. *Some new results on transport and density of state distribution in glow discharge microcrystalline silicon*. Journal of Non-Crystalline Solids. 1983;59–60, Part 2(0):795-8.

12. Spear WE, Willeke G, and LeComber PG. *Electronic properties of microcrystalline silicon prepared in the glow discharge plasma*. Physica B+C. 1983;117–118, Part 2(0):908-13.

13. Street R. *Hydrogenated Amorphous Silicon. Cambridge*, UK: Cambridge University Press; 1991.

14. Richard B. *Photovoltaic Materials*. Singapore: Imperial College Press 1998.

15. Beyer W, and Stuke J. *Amorphous and Liquid Semiconductors*. Taylor and Francis Ed. 1974:251.

16. LeComber PO, Loveland RJ, Spear WE, andVaughan RA, editors. *Amorphous and Liquid Semiconductors*. Proc 5th Int Conf; 1974 1974; London: Taylor & Francis.

17. Lewis AJ, Connell GAN, Paul W, I.R. P, andTemkin RJ. *Tetrahedrally Bonded Amorphous Semiconductors*. Yorktown Heights1974.

18. Beyer W. Chapter 5: *Hydrogen Phenomena in Hydrogenated Amorphous Silicon*. In: Nickel N H, editor. *Semiconductors and Semimetals*: Elsevier; 1999. p. 165-239.

19. Tanaka K, Eiichi M, Toshikazu S, and Okamoto H. *Amorphous silicon*: Wiley; 1999.

20. Takahashi K, andKonagai M. *Amorphous silicon solar cells*: John Wiley & Sons Canada, Limited; 1986.

21. Shim JH, and Cho NH. *Structural and Chemical Features of Silicon Nanocrystallites in Nanocrystalline Hydrogenated Silicon Thin Films*. Glass Phys Chem. 2005 2005/07/01;31(4):525-9.

22. Matsuda A. *Growth mechanism of microcrystalline silicon obtained from reactive plasmas*. Thin Solid Films. 1999;337(1–2):1-6.

23. Kondo J, Tabata A, Kawamura T, and Mizutani T. *Dependence on substrate temperature of the film structure of μc-Si:H prepared by RF magnetron sputtering*. Vacuum. 2002;66(3–4):409-13.

24. Matsuda A. *Microcrystalline silicon.: Growth and device application*. Journal of Non-Crystalline Solids. 2004;338–340(0):1-12.

25. Vetterl O, Finger F, Carius R, Hapke P, Houben L, Kluth O, Lambertz A, Mück A, Rech B, and Wagner H. *Intrinsic microcrystalline silicon: A new material for photovoltaics*. Solar Energy Materials and Solar Cells. 2000;62(1–2):97-108.

26. Finger F, Klein S, Dylla T, Baia Neto AL, Vetterl O, and Carius R. *Defects in Microcrystalline Silicon Prepared With Hot Wire CVD*. MRS Online Proceedings Library. 2002;715.

27. Shaw JG, and Hack M. *An analytic model for calculating trapped charge in amorphous silicon*. Journal of Applied Physics. 1988;64(9):4562-6.

28. Wei W, andYan X. *Structural characterization of boron doped hydrogenated nanocrystalline silicon films*. Vacuum. 2009;83(5):787-91.

29. Wensheng W, Tianmin W, Chunxi Z, Guohua L, Hexiang H, and Kun D. *Preferred growth of nanocrystalline silicon in boron-doped nc-Si:H Films*. Vacuum. 2004;74(1):69-75.

30. Wang J-L, and Wu E-X. *Characterization of doped hydrogenated nanocrystalline silicon films prepared by plasma enhanced chemical vapour deposition*. Chinese Physics 2007;16(3):848-53.

31. Schropp REI. Chapter 5 - *Amorphous (Protocrystalline) and Microcrystalline Thin Film Silicon Solar Cells*. In: Soga T, editor. *Nanostructured Materials for Solar Energy Conversion*. Amsterdam: Elsevier; 2006. p. 131-66.

32. Shimakawa K, Singh J, O'Leary SK. *Optical Properties of Condensed Matter and Applications*. In: Singh J, editor.: Wiley; 2006. p. 47-61.

33. Lucovsky G, Wang C, Nemanich RJ, and Williams MJ. *Deposition of μc-Si and μc-Si-C thin films by remote plasma-enhanced chemical-vapor deposition*. Solar Cells. 1991;30(1–4):419-34.

34. Yin Y. *Nanocomposite thin films for solar energy conversion*. In: Zhang S, andAli N, editors. Nanocomposite Thin Films and Coatings: Processing, Properties and Performance: World Scientific Publishing Company, Incorporated; 2007.

35. Lieberman M A, and Lichtenberg AJ. *Principles of Plasma Discharges and Materials Processing*: Wiley; 2005.

36. Zeman M. *Advanced Amorphous Silicon Solar Cell Technologies*. Thin Film Solar Cells: John Wiley & Sons, Ltd; 2006. p. 173-236.

37. Lind AHN. *Deposition and Characterisation of Silicon and Conductive Layers on Woven Polyester*. PhD thesis. Edinburgh: Heriot-Watt University; 2013.

38. Hiramatsu, M. and Hori, M., *Carbon Nanowalls: Synthesis and Emerging Applications*. 2010: Springer.

39.L. Houben, M. Luysberg, P. Hapke, R. Carius, F. Finger, and H. Wagner, "*Structural properties of microcrystalline silicon in the transition from highly crystalline to amorphous growth*," Philosophical Magazine A – Physics of Condensed Matter Structure, Defects, and Mechanical Properties, vol. 77, No. 6, pp. 1447 – 1460, Jun. 1998.

40. Kasap, S., et al., *Optical Properties of Electronic Materials: Fundamentals and Characterization*, in Springer *Handbook of Electronic and Photonic Materials*, S. Kasap and P. Capper, Editors. 2007, Springer US. p. 47-77.

Chapter 3. Experimental techniques and deposition methods

3.1 Introduction

This chapter briefly presents deposition techniques for thin film layers and characterisation setups used throughout this work. Heat treatment calendaring process was applied on polyester fabrics to flatten and smooth the substrates. Textiles were prepared and coated with conductive polymer then coated with a thin film of aluminium to form a back contact. The main deposition technique is plasma enhanced chemical vapour deposition (*PECVD*) which was used to fabricate amorphous silicon layers. The back contact was made by evaporating aluminium onto the substrate whereas indium tin oxide ITO was sputtered directly onto the devices to form top contacts.

Semiconductor and conductive layers were characterised by different types of techniques. Four–point probe was used to measure surface resistivity and external quantum efficiency (EQE) current-voltage measurements (*IV*) enabled the efficiency of the cells to be measured. Raman spectroscopy was used to probe the crystallinity of the sample. Optical microscopy and scanning electron microscopy (SEM) were used to probe the surface of the samples. Optical spectrometry (*R,T*) and ellipsometry (*n* and *k*) were used to characterize the optical properties of our layers.

3.2 Substrates and Metal contacts

Different types of substrate were used in this project such as glasses, silicon wafers, polyester fabrics, and PTFE fabrics. All of these substrates need to be prepared to hold amorphous silicon solar cell configuration. Samples were cleaned to avoid any unwanted impurities and then transferred to the next stage where conductive contacts were introduced onto the substrates. Aluminium masks were used to pattern contacts onto substrates.

3.2.1 TCO and metal deposition

3.2.1.1 Aluminium evaporation

An Edwards E306A vacuum thermal evaporator unit was used to deposit metal contacts (Figure 3.1) from conventional resistance-heated filaments or boats. This process is used for various metals, from aluminium and copper to gold and platinum [1, 2]. Mainly aluminium was used in this project for its availability and good electrical conductivity.

A schematic diagram of the vacuum evaporation unit is shown in Figure 3.2. The evaporation process takes place in a glass chamber where samples are placed near the top of chamber. A Quartz crystal thickness monitor was located near the sample. At the bottom of the chamber, thermal evaporation sources face the sample and between them there is a shutter to prevent deposition during warm up and degassing of the source. The system employs two types of pumps; rotary and diffusion pumps which can provide base pressure in range of 10^{-7} Torr. See Appendix C.2 for evaporation procedure.

Figure 3.1. Edwards E306A thermal evaporator.

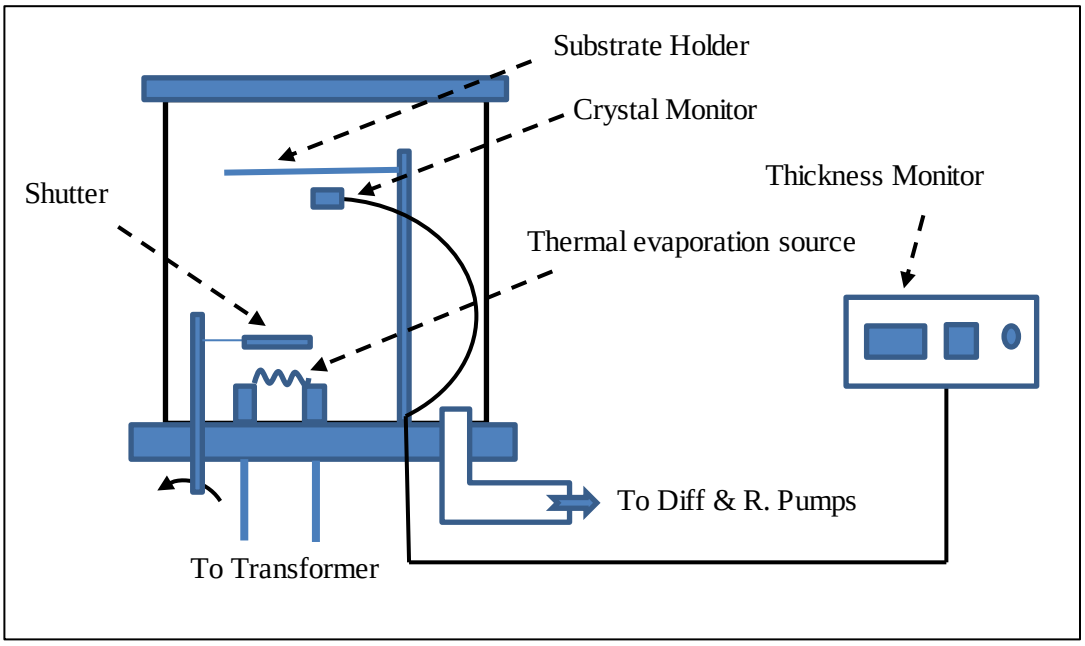

Figure 3. 2. Schematic diagram of the vacuum evaporation.

3.2.1.2 TCO sputtering

Transparent front contacts with sufficient electric conductivity and low reflectivity need to be deposited in order to be able to collect photogenerated current. Indium tin oxide (ITO), tin oxide (SnO_2), and zinc oxide (ZnO) have been widely studied and applied as transparent conducing oxides (TCOs) in thin-film solar cells [3-5]. These TCOs are also used between silicon and the metallic contact as a part of the back reflector to improve optical properties and to act as a diffusion barrier [5].

In our case, ITO deposition was performed employing Edwards Auto 306 RF-Sputter Coater using r.f. sputtering technique from an ITO target (99.9%). The sputtering system consists of a vacuum chamber, a target (cathode) and substrate holder (anode). Basically, a target is bombarded by energetic ions which are generated in a glow discharge plasma, occurring in front of the sputtering target. Because of this bombardment, target atoms are ejected toward the substrate and may then condense to form a thin film [6]. The scheme of the sputtering system is shown in Figure 3.3. See Appendix C.1 for sputtering procedure.

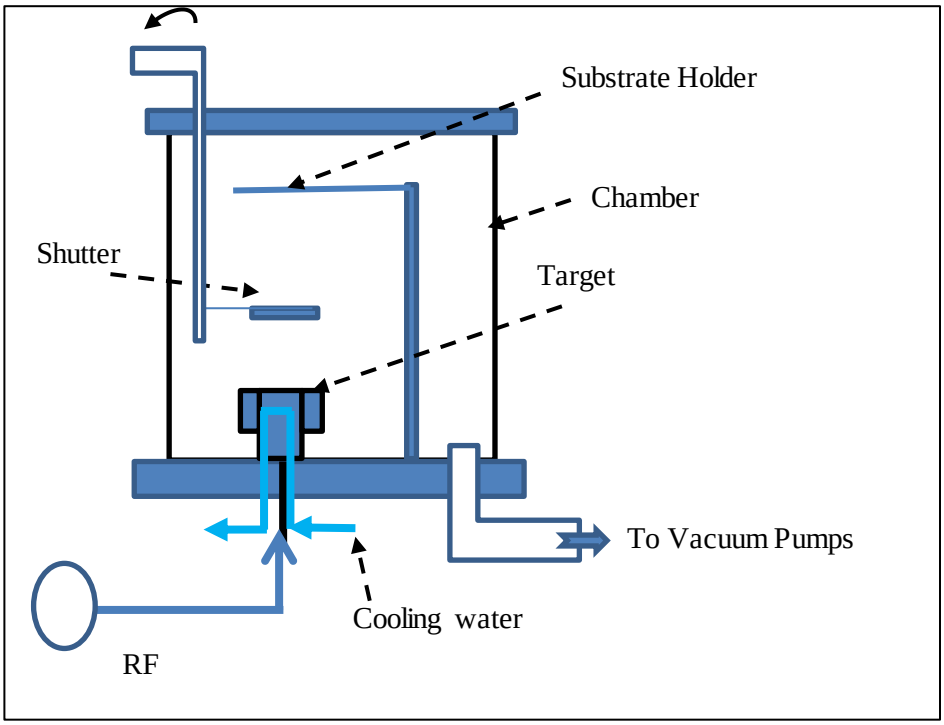

Figure 3.3. Schematic diagram of the sputtering system.

3.2.1.3 Masking

To define the area of each layer of the sample solar cells and avoid short-circuiting, different designs of aluminium masks were made. These masks were used to pattern both conductive contacts and semiconductor configurations at the top of the substrate. Many types of patterns were designed in this work. For example, a back aluminium electrode was deposited through a metal mask with different patterns. Figure 3.4 (middle) shows a sample of aluminium mask used to form contacts with silicon layers on polyester fabrics (right). The left side of the same figure shows masks used to form aluminium dots for electrical measurements.

Figure 3.4. An example of Aluminium mask (middle) used to pattern solar cell devices (Right). Mask used to form aluminium dots with different sizes (left).

3.2.1.4 Fabric calendaring and liquid coating

Heat treatment calendaring process was applied on polyester fabrics to flatten and smooth the substrates. The process was carried out using a Roaches single head (Figure 3.5a), large plate 8"x8" heater where the textile sample was placed in-between two plates at about 240^{o}C, the top plate having a weight of about 4kg which provides appropriate pressure on fabrics. The process was carried out for 1 minute. Our research used a wet coat process for a conductive polymer applied by simplified method of knife-over-table as shown in Figure 3.5b. (See Appendix B)

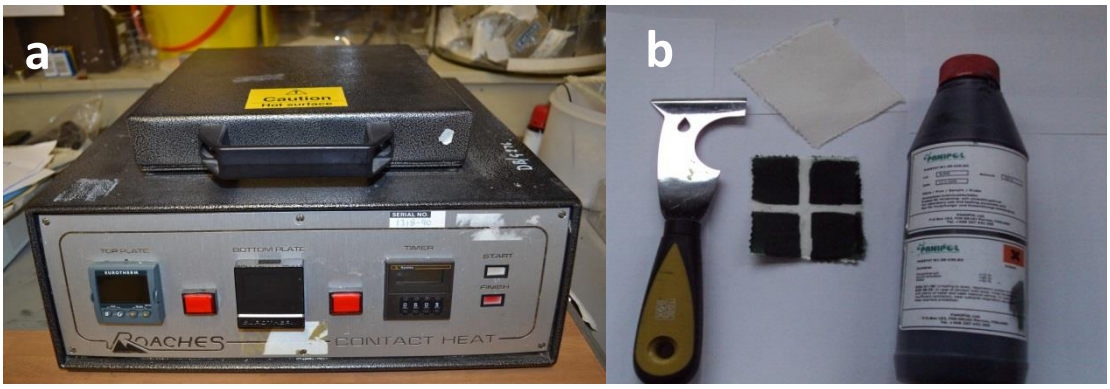

Figure 3.5. (a) Roaches single head calendaring equipment (b) knife-over-table coating technique.

3.3 Growth of a-Si:H films

3.3.1 RF-PECVD system

The most common technique of depositing a-Si:H films for solar cells is plasma enhanced chemical vapour deposition (PECVD) as described in section 2.3.1 [7]. The deposition system at Heriot-Watt University is shown in Figure 3.6. The system (Figure 3.7) consists of several major parts:

- Gas delivery system that includes gas cylinders, pressure regulators, mass flow controllers, purifiers and various valves.
- The deposition chamber that has gas inlet, substrate holder, substrate heater, electrodes, thermocouple probe and RF power feed-through.
- Pressure control system that has a throttle valve linked to pressure gauges.
- Pumping system that has rotary and diffusion pumps.
- Exhaust system with provision for inert gas purging.

- A control panel that monitors and controls the chamber pressure, deposition chamber temperature, gas flow rate, and RF input power.

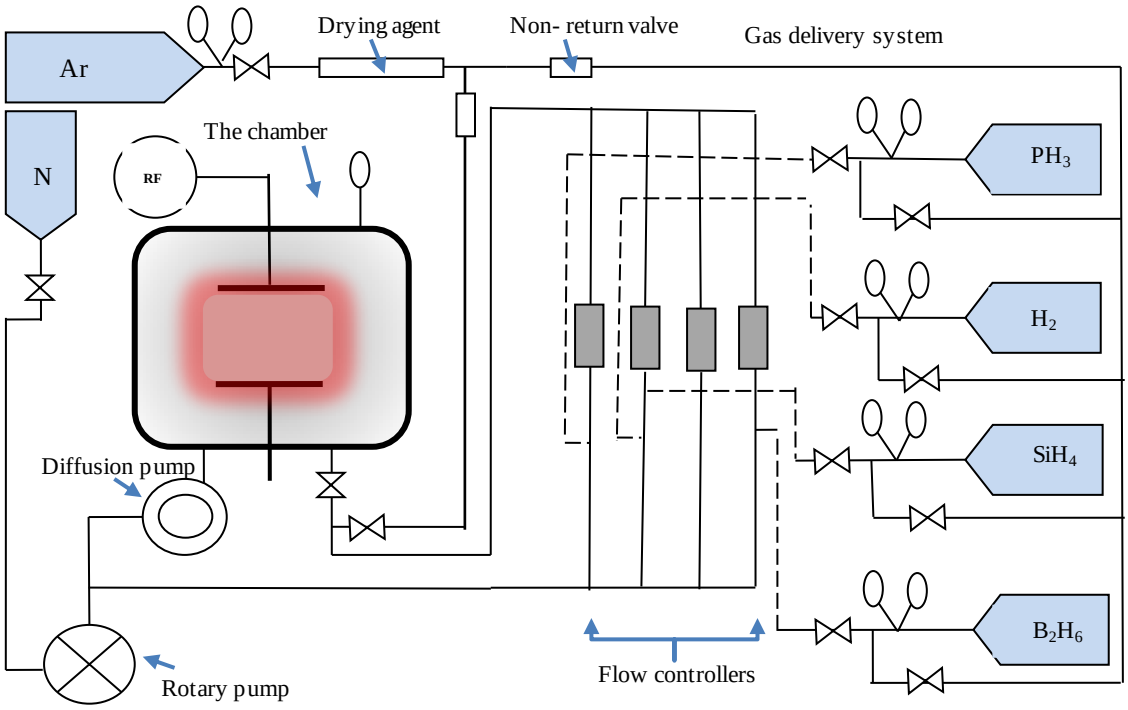

Figure 3.6. Diagram of gas delivery system used at Heriot-Watt University.

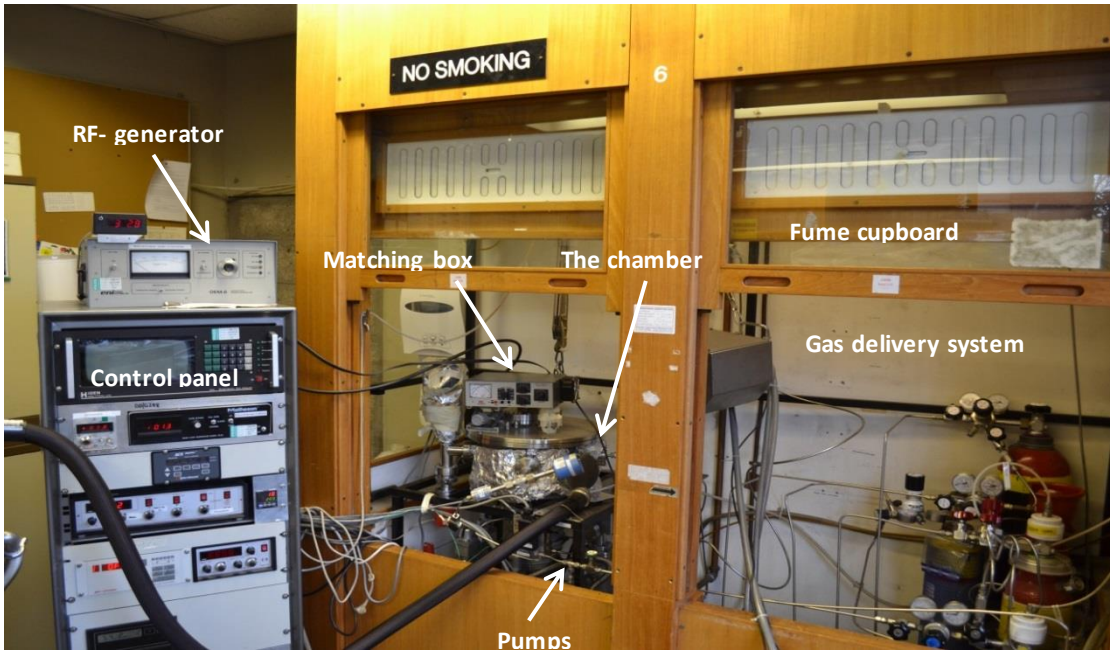

Figure 3.7. Photograph of PECVD system at Heriot-Watt University.

3.3.2 Deposition parameters

The PECVD growth conditions have a direct impact on the quality of the silicon film. Deposition parameters can be concluded as following:

- Chamber Pressure: most important parameter to sustain the plasma. At the high pressure, higher silane species, or dust, will form in the chamber and the rate of growth of thin film will increase significantly [8].
- Substrate temperature: High temperature substrate provides a large amount of energy to SiH_x adatoms which in turn increases their adatom mobility. Because of extra mobility, the adatoms can diffuse across the substrate and find the lowest free energy position. However, high temperature substrate leads to loss of hydrogen from the surface. Thus from research it has been shown that the optimum substrate temperature for thin film growth is in the range of 200^{o}C to 300^{o}C [8, 9].
- RF Power density: High power density above 100mW/cm^2 introduces a higher electric field which causes the positive ions to bombard the sample surface. Thus the dangling bond density in the deposited film increases. Furthermore, high power density leads to formation of powder. It is observed from experimental results that the optimum power density value ranges between 10 to 100 mW/cm^2 [8].
- Gas flow rate: It is another important parameter in deposition process. The residence time of heavy and short life times radicals in the plasma increase by decreasing the gas flow rate. That increases their contribution toward the thin film growth which causes a poor structure and poor film quality. In contrast, at high flow rates the gas utilization rate is low.

3.3.3 PECVD System Deposition Process

Key steps in the CVD process for silicon films are given as follows (described in the thesis of S. Jardine [10]):

- Samples are loaded into the chamber.
- Argon gas is used to purge the chamber and gas lines. The purge cycle is an important process to remove any air contamination before deposition takes place.
- Reactor pressure controller is set so the pressure can be stabilised during deposition.
- Substrate temperature is set on the temperature controller.
- Cooling water is supplied to the RF power generator and the impedance matching box fan switched on.
- Nitrogen purge is applied to the pump exhaust.
- The feedstock gas cylinders are opened.
- Flow rate of precursor gases is set from the flow rate controller.
- Once substrate temperature is reached, deposition is started by switching on radio frequency generator to initiate plasma in the reactor and the power output is set.
- While the deposition is taking place the following parameters are recorded on the form (see Appendix D): substrate temperature, chamber pressure, gas flow rates, RF power and plasma stability.
- When the deposition is complete, RF-power is turned down to zero and power generator is switched off.
- The feedstock gas cylinders and regulators are closed
- Substrate heater is switched off.
- Feedstock gases are evacuated.
- Feedstock networks and the deposition chamber are purged with Ar and pumped out; Nitrogen purge off.
- The chamber is vented to atmospheric pressure and the samples are taken out then stored in single containers.

3.4 Measurement techniques

In this part, some tools used to characterize the thin films will be described. Structural, electrical and optical properties were analysed as they all bring some additional insight into the material features.

3.4.1 Electrical characterisation of thin films

3.4.1.1 Four point probe

A collinear four–point probe array is the most common way to measure a semiconductor material's resistivity [11]. Refering to Figure 3.8, the four probes arranged in a line measure the resistivity of samples by passing a constant current through the two outer probes and measuring the voltage drop across the inner probes with a digital multimeter. The distance between the contact points (*s*) must be the same. By taking into account the following two aspects, reliable results can be obtained. Firstly, the contact areas should be small compared with the distance between the probes. Secondly, sample thickness (*t*) should be smaller than the distance between the probes. However, undoped a-Si:H layers are too resistive to be measured by this setup.

The resistance *R* can be obtained by plotting the *I-V* data and the resistivity ρ is then calculated from the following equation:

$$\rho = \frac{\pi}{\ln 2}\frac{dV}{dI} \qquad \rho = 4.5324\, t\, R \;\; \text{if} \;\; s \gg t \qquad (3.1)$$

The sheet resistivity ρ_s can be calculated as follows:

$$\rho_s = \frac{\rho}{t} \implies \rho_s = 4.5324R \;\; (\; \Omega \blacksquare^{-1} \;) \qquad (3.2)$$

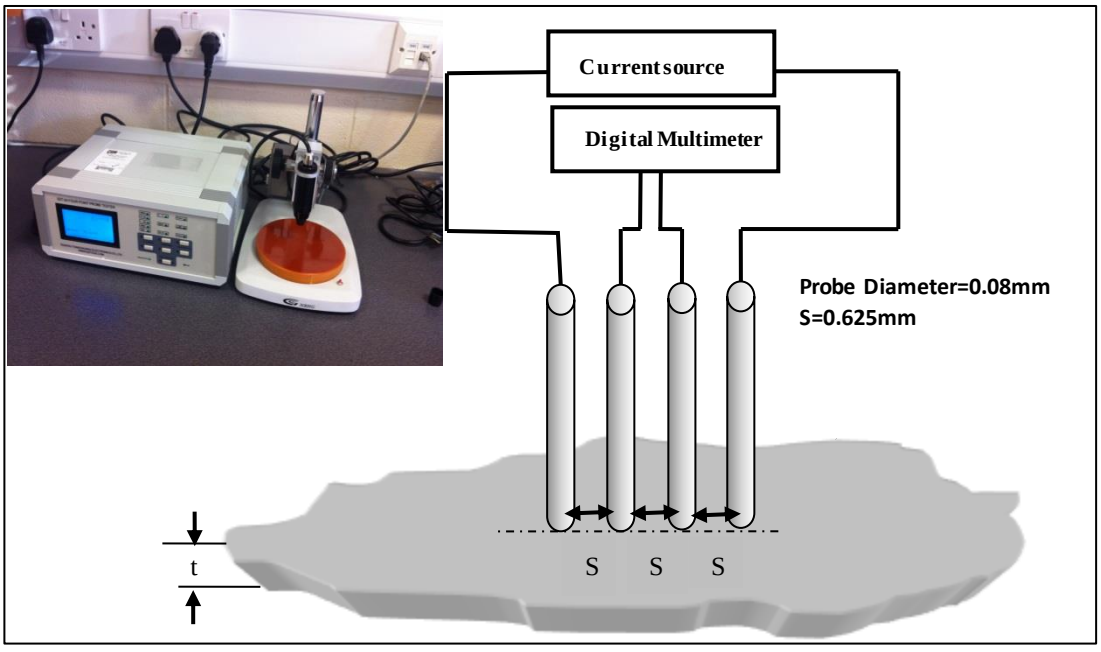

Figure 3.8. Schematic illustration of the measurement of a four–point probe.

3.4.1.2 I-V probe station

Figure3.9 shows a schematic diagram of the probe station used for I-V characterization of deposited layers. I-V data were collected through the sample by using the Wentworth Labs probe station connected to an HP 4140B picoammeter/DC voltage source. This set up was controlled by HPVEE program to collect current and voltage data. Wentworth Labs probe set-up consisted of a sample holder, which can be heated by controlled heater, microscope and two adjustable electrical probes.

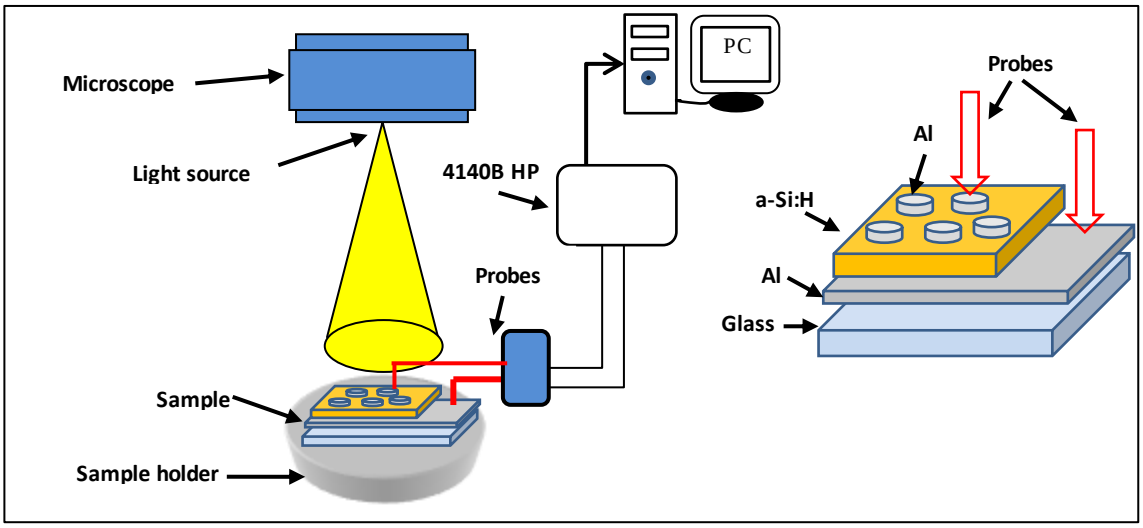

Figure 3.9. Schematic diagram of experimental setup used for dark I-V characterization.

I-V data can be used to obtain the resistivity of silicon layer using:

$$\rho = R\frac{A}{l} \qquad (3.3)$$

Where R is the resistance, l is the distance between contacts (sample thickness), and A is the top contact area. Temperature dependent *I-V* characterization was carried out to calculate the activation energy E_a from the temperature dependence of the dark conductivity σ_d expressed by

$$\sigma_d = \sigma_0 \exp\left(-\frac{E_a}{KT}\right) \qquad (3.4)$$

where σ_0 is the conductivity prefactor, and K is the Boltzmann constant. The activation energy E_a is given by the difference between the average energy of the conducting electrons and the Fermi energy. A voltage was applied over the sample and current through the layer between electrodes was measured as function of temperature from

room temperature to 100°C in increments of 5°C. Thereafter an Arrhenius plot of dark conductivity data versus the reciprocal temperature (100/T) was done and E_a was calculated from the slope of the graph.

3.4.1.3 Current density -voltage J(V) measurement

Current density–voltage measurement is a fundamental electrical characterisation technique used to determine solar cell performance. This characterisation was carried out with ABET sun 2000s solar simulator which has a spectrum AM 1.5 and intensity equal to 100 mW/cm^2.

Figure 3.10 shows the solar simulator setup at Heriot–Watt University. The main part of the simulator is the light source unit, consisting of a white light source and a set of filters that simulate the solar irradiance. Illuminated *I-V* characteristics of the cells were measured using computerised Keithley 2400 source meter.

Typical current –voltage curve of a solar cell under illumination is shown in Figure3.11. The short circuit current I_{sc} and open circuit voltage V_{oc} are indicated as well as maximum power point P_{max} . The short circuit current is measured when the voltage is equal to zero whereas the open-circuit voltage is measured when no current flows through the solar cell. Fill factor can be defined as [12]:

$$FF = \frac{J_{mp}\ V_{mp}}{J_{sc}\ V_{oc}} \qquad (3.5)$$

Where J_{mp} and V_{mp} are the current density and voltage corresponding to the maximum power produced by the solar cell and J_{sc} is short circuit current density.

The efficiency of the solar cell η is the ratio of the maximum power generated by the solar cell to the total incident power per unit area P_{in} which is equal to 100 mW/cm^2

$$\eta = \frac{J_{sc}\ V_{oc}\ FF}{P_{in}} \qquad (3.6)$$

Shunt and series resistance were also extracted from the solar cell *I-V* characteristics. Shunt resistance was calculated from the inverse slope of the *I-V* curve when a negative bias is applied to the solar cell. Series resistance was found from the inverse slope for positive applied voltages.

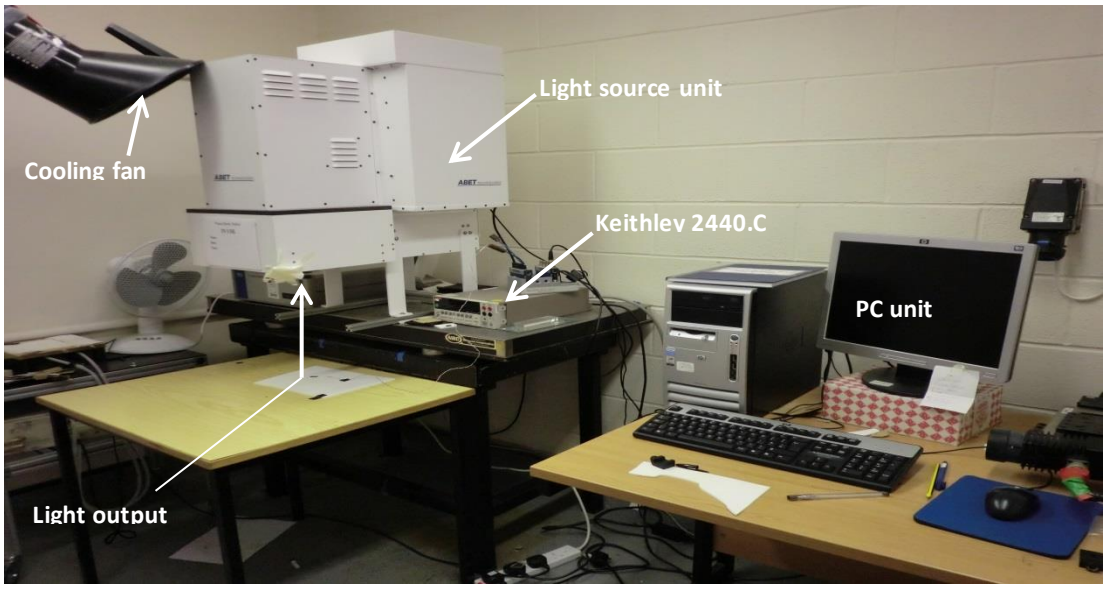

Figure 3.10. The ABET sun 2000s solar simulator setup at Heriot –Watt University.

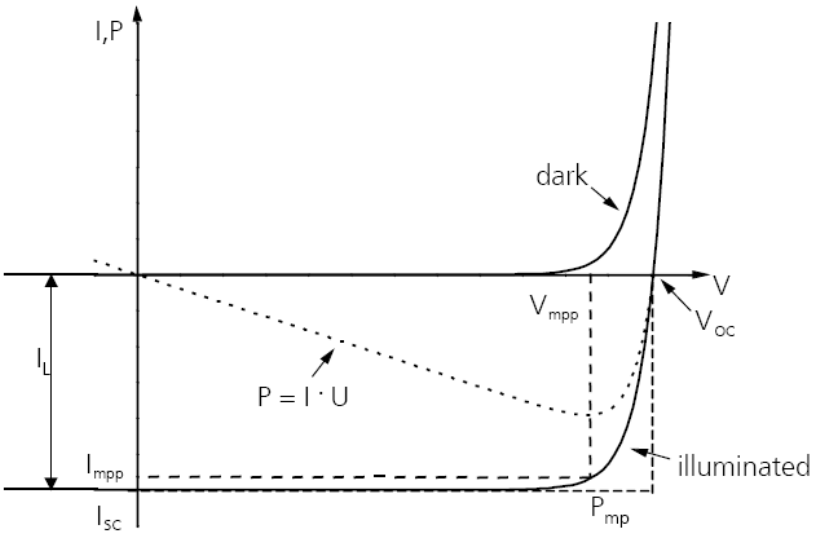

Figure 3.11. Typical I-V characteristic of a solar cell under illumination [13].

3.4.1.4 External quantum efficiency (EQE)

External quantum efficiency (*EQE*) was measured to determine wavelength dependent collection of photogenerated charge within the amorphous silicon solar cell. It can be defined as the number of electrons obtained outside the device divided by the number of incident photons. Figure 3.12 illustrates the external quantum efficiency set-up at Heriot–Watt University. A light source illuminated a single grating monochromator that selected a specific wavelength. Then this light passed through a chopper rotated at 13Hz. A set of optical filters and lenses was employed in the optic path to block undesired diffraction modes. In order to convert device current to voltage, a transresistive pre-amplifier was employed and attached to the sample probes. A lock-in amplifier integrated the output signal from the pre-amplifier and the signal from the chopper. EQE can be determined from voltage reading data obtained from the lock-in amplifier for an a-Si:H solar cell alongside a reference c-Si photodiode with a known quantum efficiency

EQE can be calculated with:

$$EQE = EQE_{ref}\left(\frac{V_{device}}{V_{ref}}\right) \qquad (3.7)$$

where $V_{devices}$ is voltage reading data obtained from the lock-in amplifier for an a-Si:H solar cell, V_{ref} is voltage reading for 0.5x0.5 cm^2 c-Si photodiode cell, and *EQE* ref is the quantum efficiency of c-Si photodiode.

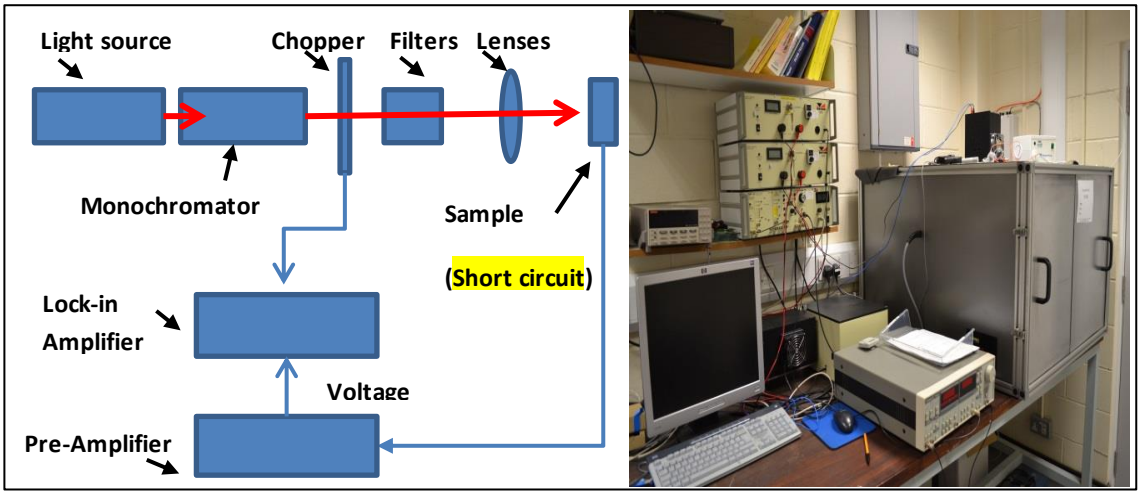

Figure 3.12. Diagram of the external quantum efficiency apparatus.

3.4.2 Optical characterisation of Thin films

3.4.2.1 FTIR – Fourier Transform Infrared Spectroscopy

Spectroscopy can be defined as the uses of the absorption, emission, or scattering of electromagnetic radiation by atoms or molecules to study physical process. Fourier transform infrared spectroscopy is one of those tools. It is a powerful tool for identifying types of chemical bonds in a molecule by producing absorption spectra that result from chemical bond oscillation. The molecular bonds vibrate with frequencies that correspond to the infrared energy range. The oscillation can interact with a beam of infrared directed onto the sample so this interaction can translate as a difference between intensity of incident and transmitted IR beam. Figure 3.13 shows schematic diagram of basic parts of an interferometer. FTIR spectra of pure compounds are generally so unique that they are like a molecular "finger print". Transmission data and film thickness are used to determine the absorption coefficient through following equation:

$$\alpha(\omega) = \frac{1}{d}\left[ln\frac{1}{T}\right] \qquad (3.8)$$

where T is the transmission and d is the film thickness.

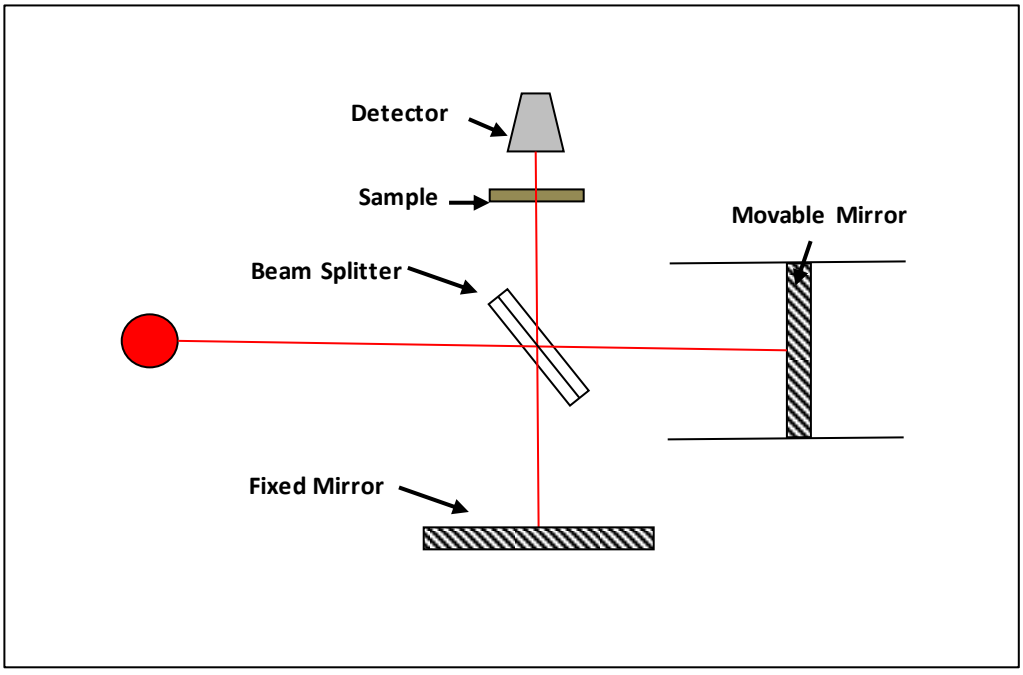

Figure 3.13. Schematic diagram of the basic optical parts of an interferometer.

3.4.2.2 Ultra-violet, visible, and near infrared spectroscopy

Optical characteristics such as absorbance, transmittance, and reflectance are analysed by Shimadzu UV-3101-PC Spectrophotometer. A simplified diagram of the principal optics system used for a spectrophotometer is shown in Figure 3.14. The spectrophotometer consists of the source lamp, the deuterium or halogen lamp, combined with a monochromator to generate near ultraviolet and visible light. This light is split into two beams by a beam splitter. First beam goes through the sample, the other through the reference sample. A glass substrate is used as reference to compensate the path difference of light for the film on a substrate. Then the two beams are collected into photo detectors, which are connected with a computer to calculate a difference absorbance between the sample and reference spectra.

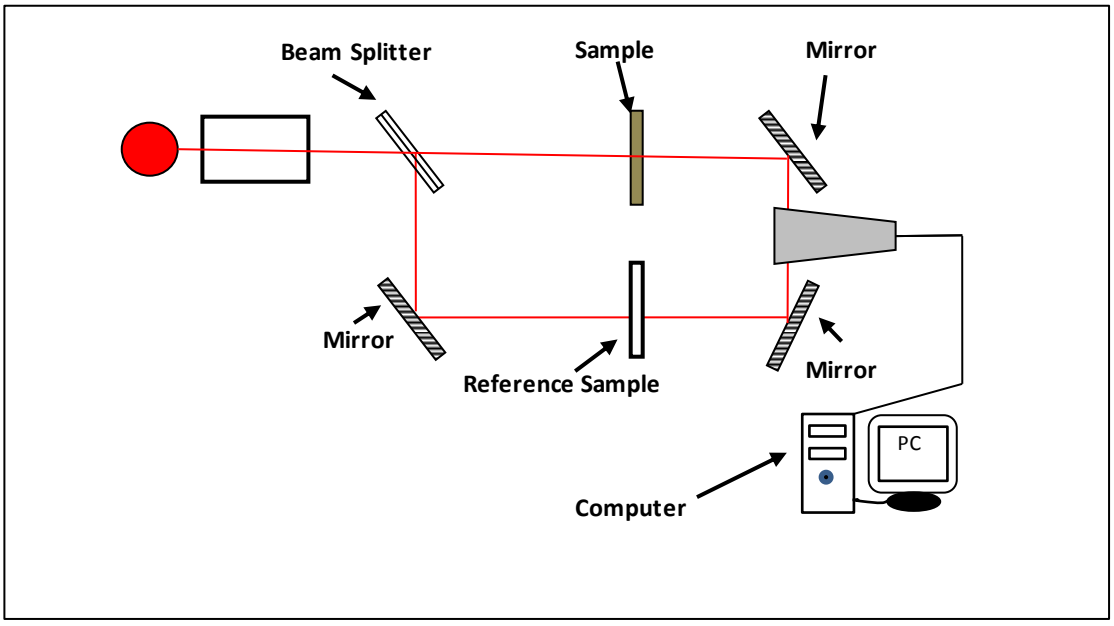

Figure 3.14. Schematic diagram of the basic optical parts of a spectrophotometer.

3.4.2.3 Variable Angle Spectroscopic Ellipsometry (VASE)

The variable angle spectroscopic ellipsometry VASE (Figure 3.16) technique measures the polarization state change for light reflected from or transmitted through a material structure. As shown in Figure3.15, the electrical field of polarized incident light can be resolved into two orthogonal components. One of them is p-polarized electric field component E_p which is parallel to the plane of incidence. The other is s-polarized component E_s that is perpendicular to the plane of incidence. These components behave differently when they are reflected from the sample which can be a bulk material or complex structure with several layers. Ellipsometry measures two values Ψ and Δ. Ψ represents the amplitude ratio of Fresnel coefficients R_p and R_s for the light wave polarized in the planes p and s respectively. Δ is the phase difference between the two planes p and s.

The ellipsometry parameters Ψ and Δ can be defined as [14] :

$$\rho = \tan\left(\Psi e^{i\Delta}\right) = \frac{R_p}{R_s} \qquad (3.9)$$

Where ρ is reflectivity of the film. These coefficients contain desired information related to material optical properties and physical dimensions. As example the measurement of the phase (Δ) is particularly sensitive to the thickness of the layers.

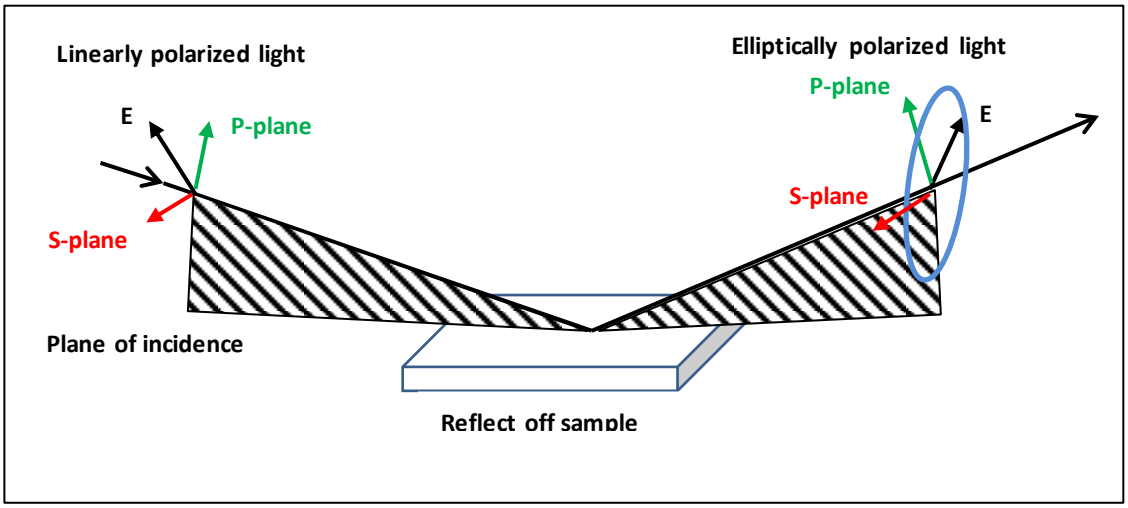

Figure 3.15. Schematic diagram of the interaction of polarized light with a sample. After ref [14].

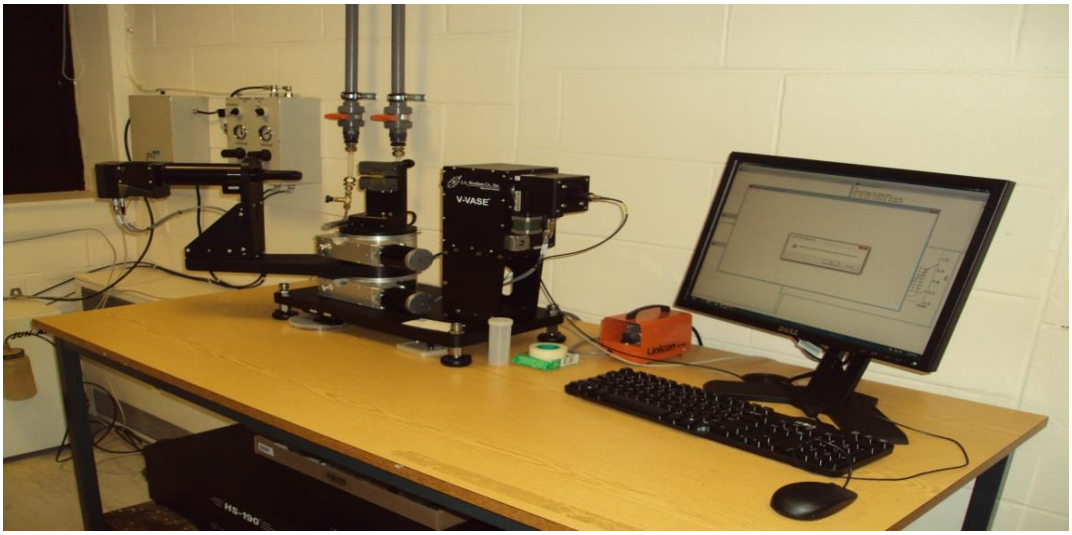

Figure 3.16. The J. A. Woollam Co Variable angle spectroscopic ellipsometry (VASE).

3.4.3 Structure and Surface Morphology

3.4.3.1 Scanning electron microscope (SEM)

The scanning electron microscope SEM employs a beam of electrons to create magnified images of samples [15]. Figure 3.17 is a simplified schematic diagram showing the main components of a SEM: the microscope column is a vacuum chamber that contains a specimen chamber, outside which are the computer, monitor, and control unit for specimen position. An essential part in the column is an electron gun that provides a stable beam of primary electrons of adjustable energy. The electrons are usually accelerated to energy between 1 and 30 KeV. A series of condenser and objective lenses guide and control the diameter of the electron beam as well as focus the beam exactly on the sample. In order to move the focused beam to scan the sample, a set of scanning coils is fitted near the bottom of the column.

At the bottom of the vacuum column is a moving stage for the samples, signal detectors for the backscattered and secondary electrons, and an X- ray detector. As soon as electrons hit the specimen, low energy secondary electrons and high energy backscattered electrons are emitted toward the detectors, which count electrons and send signals to an amplifier. Then the last stage is image processing where secondary (SE) and backscattered electrons (BSE) are used to form images. Figure 3.18 is a photograph of the SEM instrument at Heriot-Watt University that was used in this work.

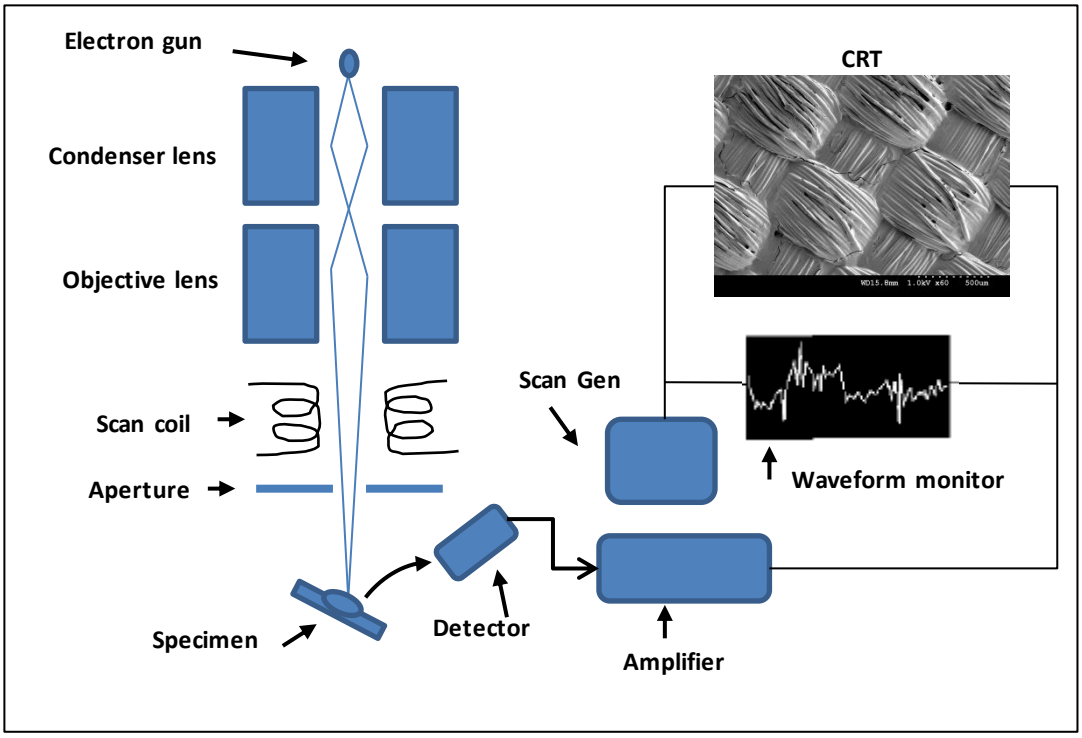

Figure 3.17. The main components of SEM (After ref [15]).

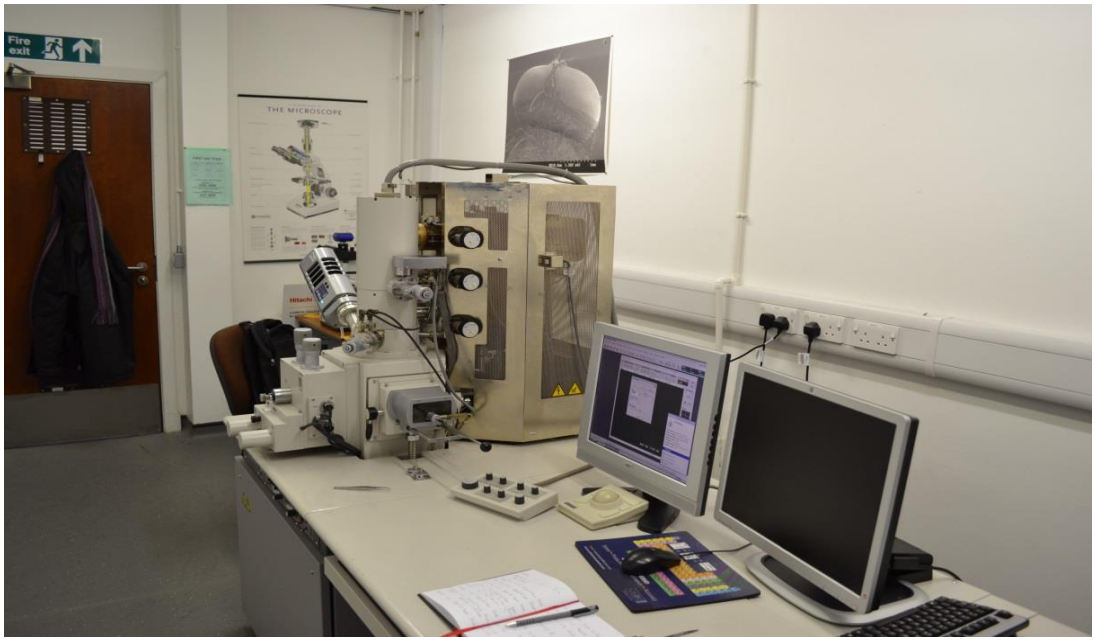

Figure 3.18. Photograph of the Hitachi S-4700 FE-SEM instrument at Heriot-Watt University.

3.4.3.2 Raman spectroscopy

The Raman effect is observed when electromagnetic radiation interacts with vibrational and/or rotational motions of molecules or atoms in a material and can be characterised by a change in energy between the incident and scattered beam. Raman scattering is an inelastic scattering process where the scattered photon has a different energy and wavelength than the incident photon. This excitation is a result of interaction between the incident photon and the bonds of a molecule. The energy from photons causes ground state electrons to be excited into virtual states. After that, an excited electron returns to ground state and another photon with different energy will be emitted.

The photons reflected from the specimen are collected through a lens then guided through filters which stop photons at the wavelength of the incident beam. Photons passed through the filters have either been shifted to a lower frequency, which is called a Stokes shift, or to a higher frequency, which is known as an anti-Stokes shift. Figure3.19 shows an energy level diagram for Stokes and anti-Stokes scattering. In the system used for this investigation, a Renishaw inVia Raman microscope as shown in figure 3.20, the sample is illuminated with 514 nm laser, beam magnification of 50x and 10µm spot diameter.

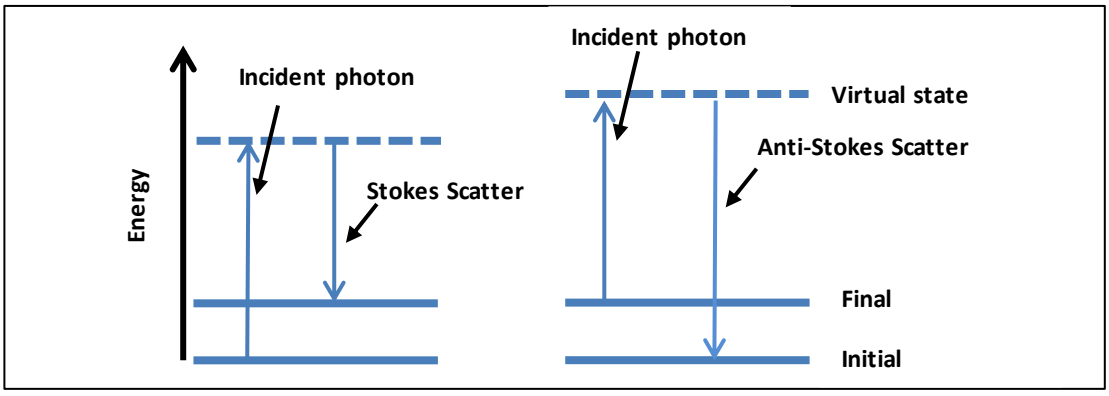

Figure 3.19. Energy level diagram. (Left) Stokes scattering and (Right) anti-Stokes scattering.

Figure 3.20. Photograph of Renishaw inVia micro-Raman Spectroscope at Heriot-Watt University.

3.4.3.3 Optical microscopy

Optical microscopy is a tool for studying morphology of samples at micron and submicron level. In reflection mode, the basic idea is that a sample is illuminated by a light source and then the fine information of surface shape can be magnified by an objective and eyepiece so that it can be seen by eyes or optical detector such as a camera. As shown in Figure 3.21, the objective lens forms the real intermediate image near the eyepiece and then eyepiece and eye form a real image on the retina. For photography, the intermediate image can be recorded directly as a real image onto a camera [16]. For small sample details to be seen by a microscope, the resolution of the system needs to be either equal or less than the size of the surface details. The resolution of a conventional optical microscope can be defined as:

$$\rho = \frac{0.61\lambda}{NA} \qquad (3.10)$$

where λ is the wavelength of light and NA is the numerical aperture of the objective. Depending on the objective aperture and the dispersion medium between the sample and the objective lens, the value of NA changes from 0.1 to 1.4.

A Leica DM600M optical microscope was used to analyse the surface of the samples in this work (see Figure 3.22).

This system has 200× magnification (ocular: 10×, objective: 20× 0.40 BD, Leica PL Fluotar). Images are recorded with a color CCD camera (ColorView8, Soft Imaging Systems GmbH,M¨ unster, Germany) and the Analysis 5.0 software (Olympus Soft Imaging Solutions GmbH, M¨ unster, Germany).

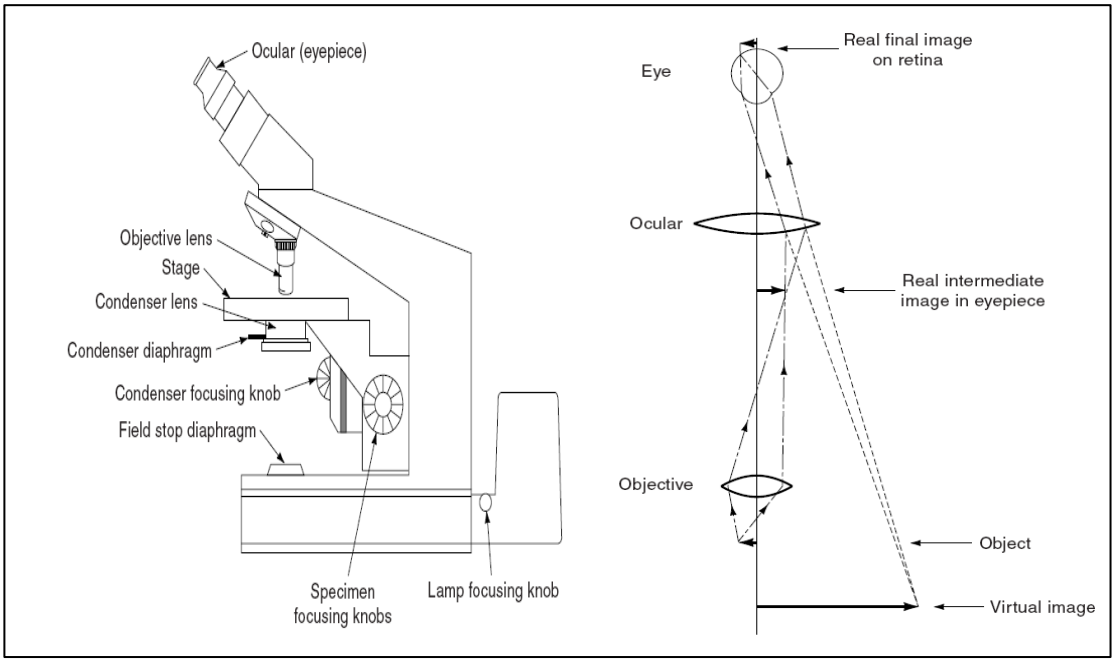

Figure 3.21. The compound light microscope (left) and perception of a magnified virtual image of a specimen in the microscope (right) [16].

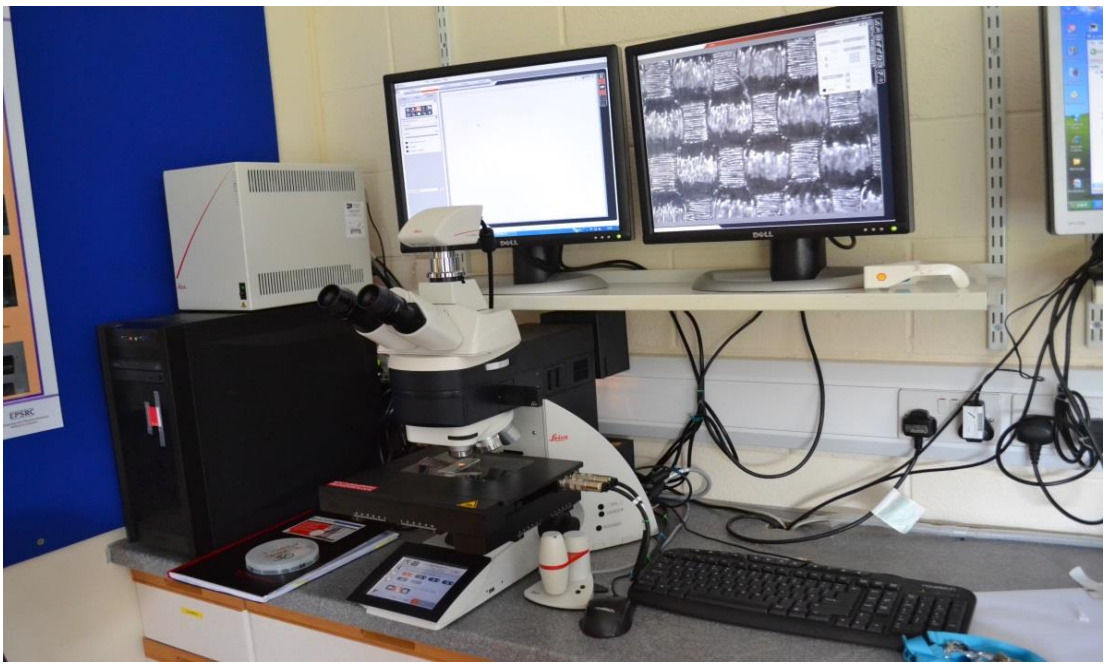

Figure 3.22. Photograph of the Leica DM600M optical microscope at Heriot-Watt University.

3.5 Conclusion

This chapter presented a brief description of methods for fabrication and characterisation of thin films. Techniques were presented for evaporating and sputtering conducting layers and for growth of a-Si:H films.

3.6 References

1. Wasa K, and Hayakawa S. *Handbook of Sputter Deposition Technology*. New Jersey: Noyes; 1992.

2. Stuart RV. *Vacuum Technology, Thin Films, and Sputtering*. New York:: Academic Press; 1983.

3. Carlson DE. *Amorphous-silicon solar cells*. Electron Devices, IEEE Transactions on. 1989;36(12):2775-80.

4. Iida H, Shiba N, T.Mishuku, H.Karasawa, A.Ito, M.Yamanaka., and Y.Hayashi. *Efficiency of the a-Si:H Solar Cell and Grain Size of SnO Transparent Conductive Film*. IEEE Electronic Device letters 1983;4(5):157.

5. Müller J, Rech B, Springer J, and Vanecek M. *TCO and light trapping in silicon thin film solar cells*. Solar Energy. 2004;77(6):917-30.

6. Rossnagel S. Sputter Deposition. In: Sproul WD, and Legg KO, editors. *Opportunities for Innovation: Advanced Surface Engineering*. Switzerland: Technomic Publishing Company; 1995.

7. Chittick RC, Alexander JH, and Sterling HF. *The Preparation and Properties of Amorphous Silicon. Journal of The Electrochemical Society*. 1969 January 1, 1969;116(1):77-81.

8. Guha S. *Multijunction Solar Cells and Modules*. In: Street R, editor. *Technology and Applications of Amorphous Silicon*: Springer Berlin Heidelberg; 2000. p. 252-305.

9. Van den Donker MN, Rech B, Schmitz R, Klomfass J, Dingemans G, Finger F, Houben L, Kessels WMM, and Van de Sanden MCM. *Hidden parameters in the plasma deposition of microcrystalline silicon solar cells.* Journal of Materials Research. 2007;22(07):1767-74.

10. Jardine S. *Thin Film Silicon on Textiles by Microwave Plasma Chemical Vapour Deposition*. PhD thesis Edinburgh: Heriot-Watt University 2006.

11. Zemel JN. *Nondestructive evaluation of semiconductor materials and devices*. Zemel JN, editor. New York: Plenum Press; 1979.

12. Streetman, B.G. and Banerjee S.K. *Solid State Electronic Devices* .Upper Saddle River United States: Prentice-Hall; 2005.

13. http://www.keithley.com/solar_cell. *Typical forward biased I-V characteristic of a solar cell.*

14. J.A. Woollam Company I. *Guide to using WVASE32*. Lincoln, NE,68508: J.A. Woollam Co., Inc; 1994-2010.

15. Goodhew P, Humphreys J, and Beanland R. *Electron Microscopy and Analysis*. London: Taylor & Francis; 1988.

16. Murphy DB. *Fundamentals of Light Microscopy and Electronic Imaging*. New York: Wiley-Liss 2001.

Chapter 4. Contacts on polyester textile as a flexible substrate for solar cells

4.1 Introduction

In recent years, there has been an increase in studies about developing photovoltaic fabrics which can be used in different textile and clothing applications. The flexibility of the solar cells could be useful in many applications for example providing power for small portable electronic devices such as personal digital assistants, mobile phones, mp3 players, and notebook computers. Energy harvesting textiles can be formed by integrating solar cells into textile structures or making a textile structure itself from photovoltaic materials. Integration of flexible solar cells into textile fibres and fabrics, in which cells are positioned in particular arrangements, can extend the photovoltaic applications from military and space applications to lighting and the provision of power for consumer electronics in daily usage[1].

The disadvantage of coating the fabrics directly with metal to form conductive fabrics is that the metallic coating is brittle and has poor abrasion resistance so is easily cracked. Coating of conducting polymer on to a flexible substrate, such as a textile fabric, can retain both flexibility of the fabric and the electrical conductivity of the polymers, which by themselves are insufficiently conducting for solar cell contacts [2-5].

The idea is to bridge micro-cracks in the metallic film and maintain conductivity by applying polymer layers under the metallic film. In the present work we have studied approaches to obtaining conductive surfaces on polyester fabrics by using commercially available conductive polymers: polyaniline and PEDOT: PSS which may then be coated with aluminium by a vacuum process. Then in the next stage amorphous silicon layers were deposited directly to form a flexible solar cell [6, 7].

The preparation process involved by cleaning the fabrics to remove manufacturing impurities, and then heat treatment (calendaring) was carried out to flatten and fuse the fibrous fabric surface. A plasma surface treatment was applied to each fabric to enhance its wettability so the conductive polymer could adhere more strongly to the fabric surface. An aluminium thin film was then evaporated on top of the polymer to form the cell back contact. Several electrical, thermal and mechanical tests were carried out at each stage.

4.2 Materials

The textile substrates were plain weave, 100% polyester with 210 filaments in warp and weft and a total loom-state weight of 250gm^2. Yarn diameter is about 0.1mm, supplied by J&D Wilkie Limited, Scotland. Two commercial conductive polymers were used: Polyaniline (Panipol W, 6 to 10 wt-% in water) supplied by Panipol Oy, Finland (Appendix A.2) and Poly (3,4-ethylenedioxythiophene)-poly(styrenesulfonate), known as (PEDOT:PSS) supplied by Heraeus Clevios GmbH, Germany (Appendix A.1).

4.3 Experimental

4.3.1 Textile substrate preparation

It is widely believed that substrates are a major source of impurities in the reaction chamber, and because of that, substrate cleanliness is one of the most important parameters in the semiconductor deposition process. Moreover, a less clean surface would result in lower surface energy, which reduces the adhesion between the film and textile and gives inconsistency in any coating process.

The uncleaned, un-treated polyester fabric has a spin finish over it. The spin finish helps to protect the newly formed filaments during the stretching (drawing) process and also provides protection as they pass through the loom during weaving. Spin finishes contain a variety of ingredients. For weaving polyester, spin finishes are often emulsions of various surface-active agents, lubricant oils, antistatic agents and biocides; they therefore possess complex formulations.

The polyester fabric samples were placed in a solution of 1% detergent (Decon) in deionised water for 30 minutes in an ultrasonic bath. Then the samples were rinsed in running (deionised) water for about 15 minutes before being dried in a flow of hot air.

4.3.2 Calendaring

Thermal calendaring is introduced in textile working to adjust the thickness and modify the surface characteristics such as smoothness, gloss, density, and opacity so fabrics can be coated uniformly [8]. In our case, by partial melting it reduces movement of each yarn or filament against its neighbours to provide a continuous surface for the flexible devices which we aim to build on top. The process was carried out using a Roaches single head, large plate 8"x8" heater where the textile sample was placed between two plates at about 240^{o}C, the top plate having a weight of about 4kg which provides appropriate pressure on fabrics. The process was carried out for 1 minute.

4.3.3 Plasma Treatment of fabric Surfaces

A plasma process can modify the surface characteristics of a material while retaining its bulk properties. The non-polar surface characteristics of polyester manifest themselves in several ways, including low wettability. Fibres have a non-polar surface due to the presence of O-H groups and if the surface could be modified to become more polar, the polymer- polyester fabric adhesion could be improved and refined [9-11].

Low pressure plasma treatments were performed in our plasma deposition chamber at room temperature for 2,5,and 10 minutes and 13.56MHz of RF power, with the air remaining inside the chamber after it was pumped down from atmospheric pressure to 0.2667 mbar.

0.01ml droplets of the water soluble polymer were placed on plasma treated and untreated polyester fabrics. The time required for the droplet to penetrate completely into the fabric was measured by using a stopwatch giving a measure of the time for the liquid to wet the fabric.

4.4 Coating of the textile

In this stage, fabrics were first coated with a layer of conductive polymer then coated by a thin film of aluminium, prior to the silicon deposition process.

4.4.1 Polymer coating

A wet coat process was used to apply conductive polymer to the fabric. Four method were tried on a laboratory scale. That can be done by one of four methods. The first, knife to table, is a simplified method of knife –on- roller by spreading the coat like butter onto the textile surface and curing the coated substrate in hot oven. The second is immersing the sample in a bath of polymer. The third method involved applying the polymer onto the fabric with a sponge. The fourth method is using a brush to coat the sample. A series of samples with different numbers of conductive coating layers was then made. In our work, knife to table is used.

4.4.2 Metal coating

Once the polymer layer had been added, approximately 100nm of aluminium was evaporated on the polymer coated sample using an Edwards E306A vacuum evaporator with tungsten filament. The base pressure generally used in this work was about 10^{-6} mbar.

4.5 Samples description

All samples were cleaned then heat treated and plasma treated and coated either with polyaniline or PEDOT:PSS. Samples were divided into two groups, group (A) were fabrics coated with different numbers of Panipol layers, and group (B) were PEDOT:PSS coated fabrics.

4.6 Electrical properties

A major parameter is the electrical resistance of the polymer coated textile. The most common technique for measuring the electrical properties of conductive films is the four- point probe measurement. However, on an irregular sample such as a piece of textile, it seemed more appropriate to use a fabric surface resistance technique. There are at least two standard methods that could be used: BS6524 and AATCC Test Method 76, 84-2005 [12-14]. These are the same in principle, and in both methods, the resistance is measured by placing an electrode assembly on the fabric, and directly measuring the electrical resistance between the two electrodes with an ohmmeter.

4.6.1 Measuring resistances of fabrics

The concentric ring electrode method is particularly useful, in that is non-destructive. The electrode can be placed on fabric samples of any size. Textile samples coated with a conductive polymer of different thicknesses were measured by a concentric probe in conjunction with a resistance meter (see Figure 4.1) [12, 14].

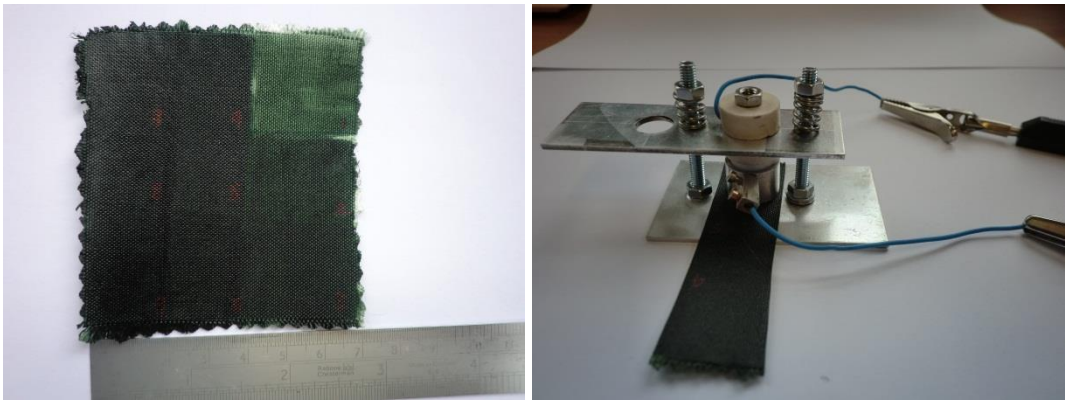

Figure 4.1. Conductive polyester fabric with different thicknesses of polymer coating (left). Concentric ring probe for measuring surface resistivity (Right).

4.6.2 Measurement of yarn resistance

In order to measure the resistance of the yarns, they were fixed on the surface of glass plates in parallel different lengths (5 to 250 mm) with enough space for coating and measuring the resistance of the yarns, as shown in Figure 4.2. Yarns were coated with different polymer concentrations by brushing.

Figure 4.2. Yarns resistance measurement setup.

4.6.3 Thermal annealing tests

In order to study the effects of temperature changes on polymer electrical properties, thermal annealing measurements were performed by using a standard concentric ring probe technique [15] according to the fixed schedule as follows:

- A polymer coated fabric was placed on the controlled heater inside the vacuum chamber (0.27mbar) in contact with the concentric ring probe (see Figure 4.3).
- The sample was heated up from room temperature to 200^0C, and at the same time the resistance was measured continuously by a computerised high resistance tester.
- When the thermal treatment temperature was reached, the sample was held at this temperature for 2400 seconds. After that the heater was switched off.
- As the sample was allowed to cool to room temperature, resistance and temperature were both recorded.

For the concentric probe, surface resistivity ρ_s is a function of the ratio between the inner and outer ring diameters as shown in the following formula:

$$\rho_s = \frac{(d_1 + d_2)}{(d_2 - d_1)} \pi R_m \qquad (4.1)$$

where d_1 and d_2 are inner and outer ring diameters respectively, R_m is measured resistance in ohms.

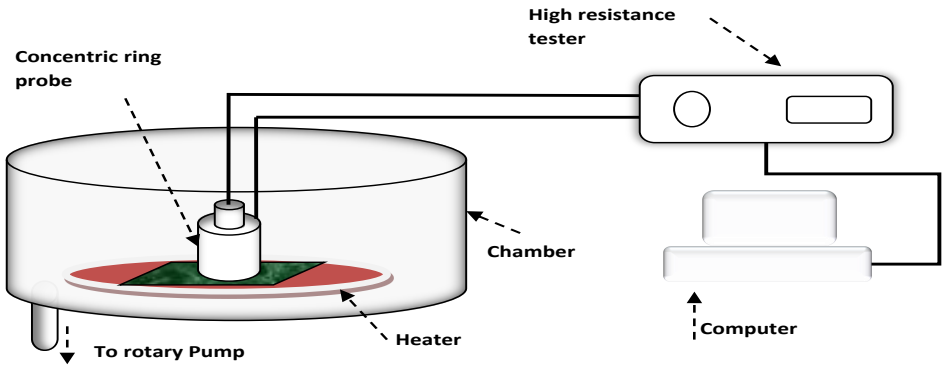

Figure 4.3. Set up for in-situ resistance measurements during thermal treatment tests.

4.6.4 Contact resistance

Contact resistance measurement of the metal-coated polymer was performed by using the transfer length method (TLM)[16]. As shown in Figure 4, identical aluminium contacts with different spacings were deposited on polymer coated fabric to form a linear TLM test sample. In this test, resistance measurements are performed between each adjacent pair of strips and contact resistance is calculated using the general formula [17]:

$$R = 2R_c + \frac{R_s}{w} L \quad [\Omega] \qquad (4.2)$$

Where R is resistance between strips, w is front contact length, R_c is a contact resistance and L is width of contacts. Sheet resistance R_s, contact resistance and transfer length L_T were calculated from the linear regression.

The TLM testing structure consisted of eight identical contacts of aluminium. Each contact was of rectangular shape with width equal to 5mm and length equal to 20mm. The distances between each pair of contacts were marked: L_1=0.001m, L_2=0.002m, L_3=0.006m, L_4=0.010m, L_5=0.015m. Figure4.4 shows The TLM testing structure on the right side and typical graphic method used to determine factors as well as real picture for patterned sample.

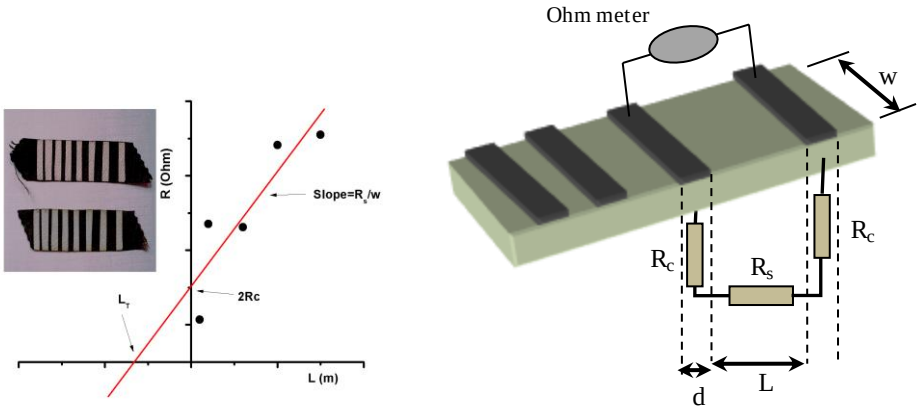

Figure 4.4 (Left) Typical graphic method used to determine factors (L_T,R_c) and real picture for patterned sample. (Right)Transmission line model (TLM) test structure.

4.6.5 Long term stability test

A longer term stability test for polyaniline and PEDOT:PSS coated fabrics was performed in room temperature by measuring surface resistivity for a period of time of 2 to 3 days. Resistance was measured by using a UNI-T 60 computerised digital multimeter.

4.7 Bending test

Two types of bending test were performed. The first type was to bend the sample vigorously while measuring its surface resistivity. The other test was to bend the sample systematically through various angles, at the same time measuring its resistivity.

4.7.1 Vigorous bending test

In this test we tried to test the electrical properties of the sample under aggressive bending conditions. To achieve that, 1cm x 4cm of aluminium strip was deposited on the polymer coated fabric. Then repeatedly, the sample was bent for 100s before bending was stopped for a further 100s. At the same time the resistance between the slides of the strip was measured continuously by a computerised high resistance tester.

4.7.2 Systematically bending test

To test the durability of the polymer coated fabrics in a systematic way under stressed conditions, we carried out the measurement of sheet resistance at different bending angles. The systematic bending test was carried out by placing the sample loosely between two boards which were then tilted against each other along a common edge to cause the bending, and sheet resistance measurements were performed at various bending angles.

4.8 Analysis of surface morphology

Scanning electron microscopy (SEM) and Energy-dispersive X-ray Spectroscopy (EDS), were used to study the deposition of PEDOT:PSS on the surface of polyester fabrics. Uncoated samples were sputtered with approximately 1 nm of gold prior to scanning electron imaging. An Olympus optical microscope with magnifications from 5 to 100 was used to monitor the surface of the fabrics and yarns.

4.9 Results and Discussion

4.9.1 Surface morphology

All fabrics were cleaned, calendared, and plasma treated. Then we systematically analysed the effects of each preparation stage on surface morphology and visual appearance of fabrics, which allowed the detection of any possible contamination. An optical image of an uncleaned yarn shows a tiny layer of finishing agent covering the yarn (Figure 4.5a), whilst it is clear that the cleaning process is sufficient to remove most of the contamination (Figure 4.5b) and the surface remained clean after calendaring (Figure 4.5c).

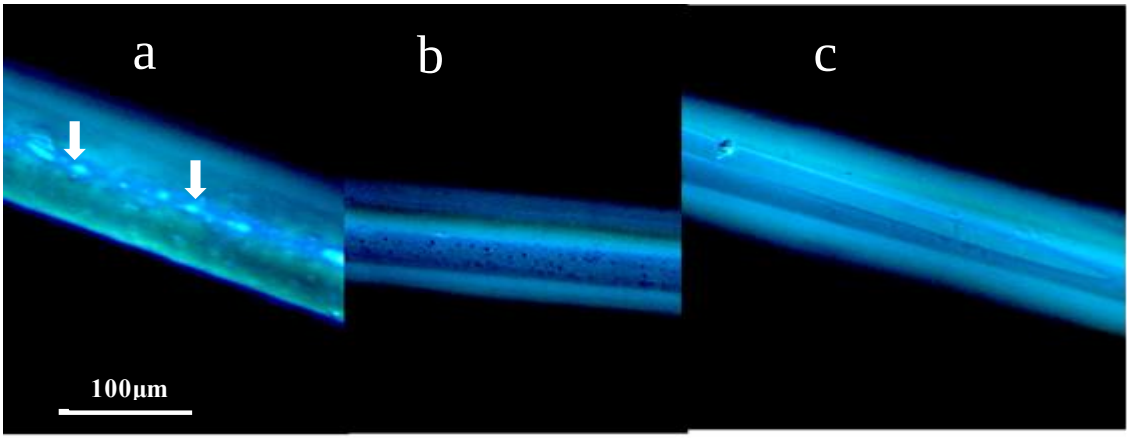

Figure 4.5. Optical images of (a) un-cleaned, and untreated yarn (b) cleaned yarn (c) heat treated yarn. The scale has magnification of x100.

Samples of polyester textiles were treated in the plasma chamber under a pressure of about 0.27 mbar for different exposure times. In the case of untreated polyester fabrics, polymer drops did not spread on the filament fabric; however, they spread significantly on the plasma treated sample, showing an improvement in surface wettability, as seen in Figure 4. 6.

In order to optimise the surface hydrophilicity of the fabrics an investigation of the effect of the plasma exposure time on the absorption of polymer droplets was performed [9]. Figure 4.7 presents the variation of plasma treatment time, the time required for the droplet to penetrate completely into the polyester fabrics, and polymer spot area (feathering spot area). The time for absorption is dramatically decreased by increasing

plasma treatment time, and the minimum polymer droplet absorption time is reached at about 5 minutes of plasma exposure. Moreover the absorption area reached a maximum value corresponding to around 6 minutes of plasma treatment.

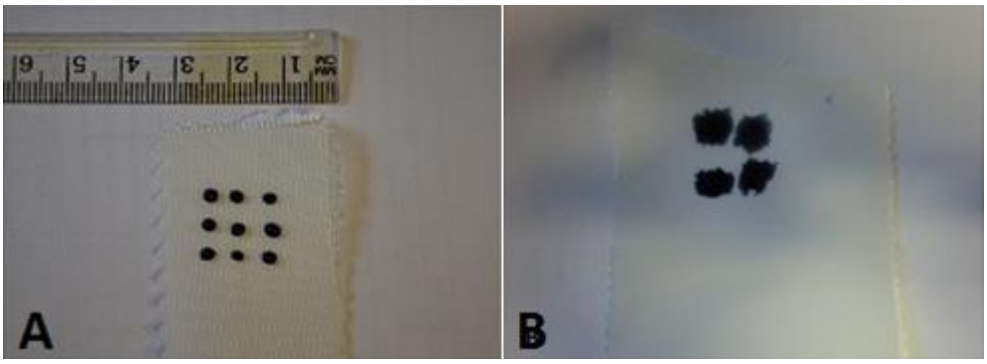

Figure 4.6 Optical images of (A) untreated fabrics (B) plasma treated fabrics.

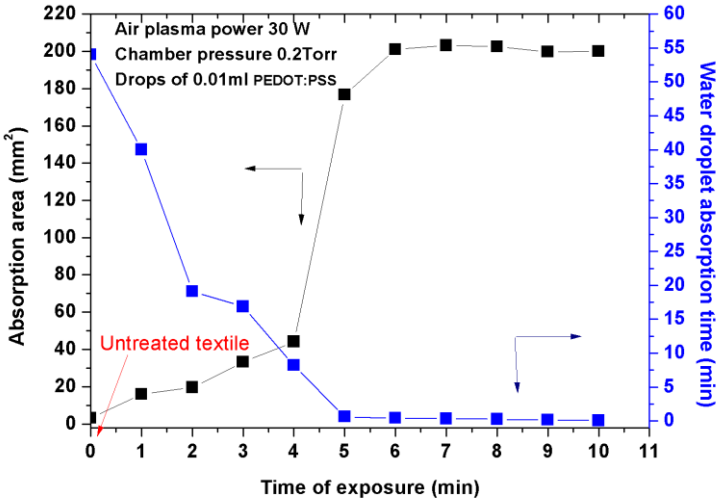

Figure 4.7. Droplet absorption area and time as a function of plasma exposure time for a polyester fabrics.

As can be seen in the SEM micrographs in Figure 4.8, the surfaces of the cleaned untreated fabrics appear smooth. Neither SEM images of fabrics nor EDS analysis of the same samples showed any level of impurities, an indication that the cleaning process was effective. Some marks can be seen on the surface of fabrics due to the thermal calendering process (Figure 4.9). The small amount of oxygen detected on the fabrics can be attributed to oxidization in the heat treatment process.

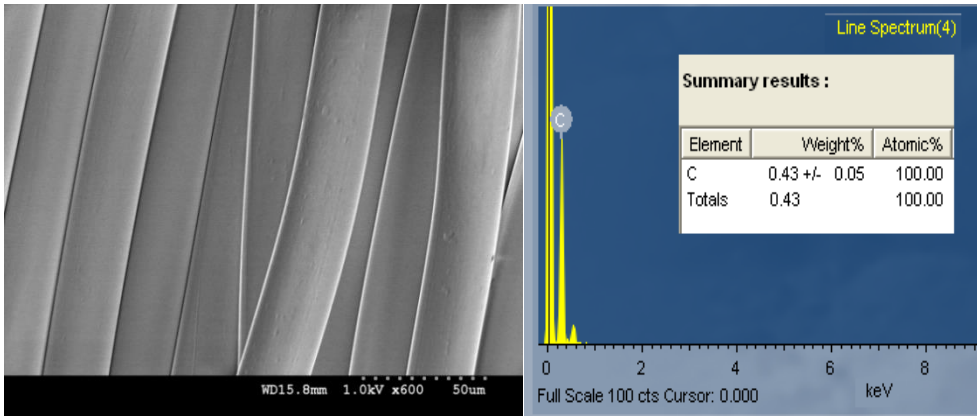

Figure 4.8. SEM for cleaned, untreated fabrics(left) and EDS analysis for the same sample (Right).

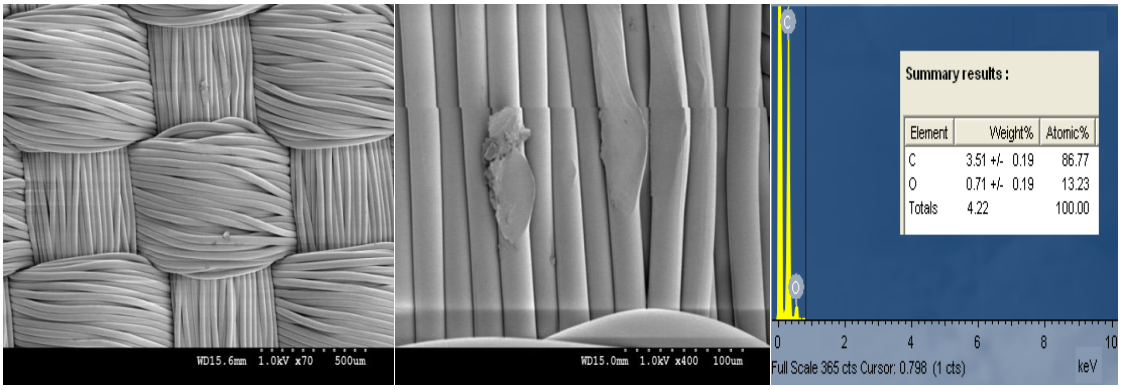

Figure 4.9. Left and middle)SEM for Cleaned, heat treated fabrics. (Right) EDS analysis for Cleaned, heat treated fabrics.

It has been observed that the degassing of the polymer solutions before coating the fabric results in reduced bubble formation, indicating a relationship between the presence of air in liquid polymers and bubble formation in coatings. The Polymer was therefore subjected to degassing process, to remove the bubbles. Degassing polymer can be performed by application of vacuum where polymer exposed to the vacuum in the chamber. The absence of micro-bubbles in the polymer reduces the number of undesired defects which cause cracking problems[18]. Figure 4.10 shows Panipol coated fabric without degassing process (right) and degassed Panipol (left). On the other hand, the fabrics coated with PEDOT:PSS did not show any bubble formation, probably due to the lower viscosity of PEDOT:PSS.

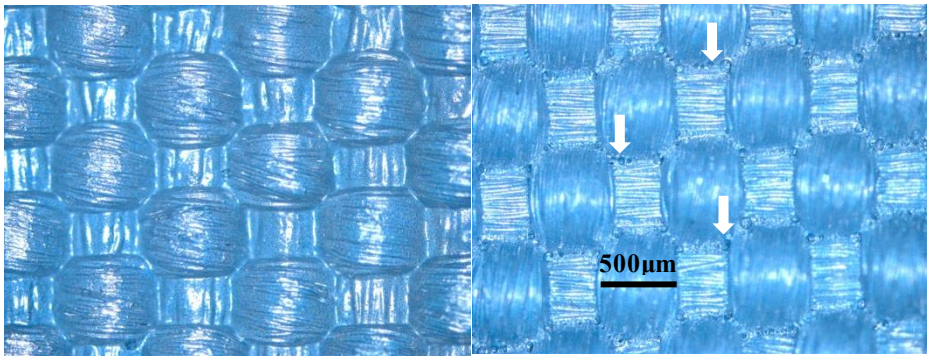

Figure 4.10 Optical photos of conductive coatings by using a microscope at 5×. (Left) degassed Panipol. (Right) un-degassed Panipol.

4.9.2 Electrical properties

4.9.2.1 Analysis of yarn results

Yarns were coated by two different types of conductive polymer: polyaniline and PEDOT:PSS. First, yarns which were fixed on a glass plate were coated individually with different numbers of Panipol layers, from one to seven. After drying, the resistance for each yarn was determined from 5 mm to 220 mm in length increments of 5mm. The left graph of Figure 4.11 shows the behaviour of coated yarn resistance with changing yarn length. In general, for Panipol coated yarn resistance increases as expected with increasing length but in a non-linear manner for the longer and thinner coatings. The right graph in the same figure shows the yarn's surface resistivity against number of coating layers, and it can be seen that the yarns reach almost constant resistance after three coats; this is therefore the optimum number of coating layers.

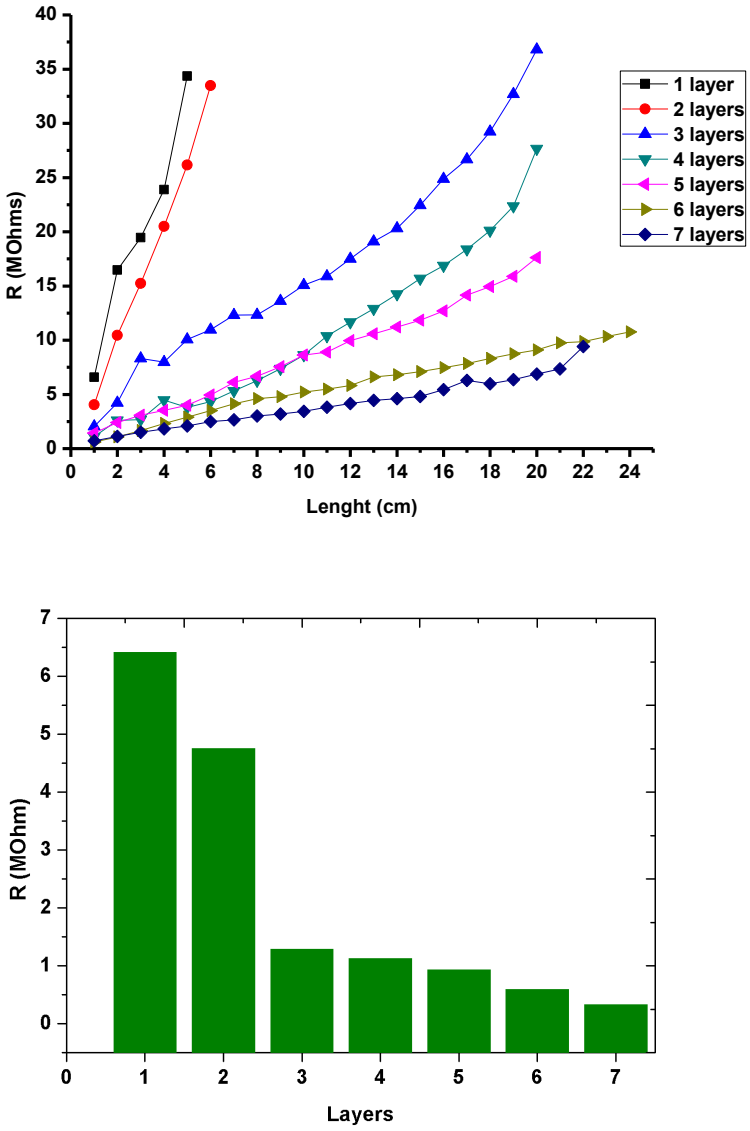

Figure 4.11. (Top) Length of yarns versus Panipol coated yarns resistance. (Bottom) Panipol coated yarns surface resistivity versus number of coating layers.

Secondly, similar yarns were coated with PEDOT:PSS and similar results obtained where yarn resistance decreased with increasing numbers of polymer coating layers as shown in Figure 4.12. By using PEDOT:PSS as conductive polymer, a near saturation level was reached after four coatings. Moreover, PEDOT:PSS has lower resistance than Panipol.

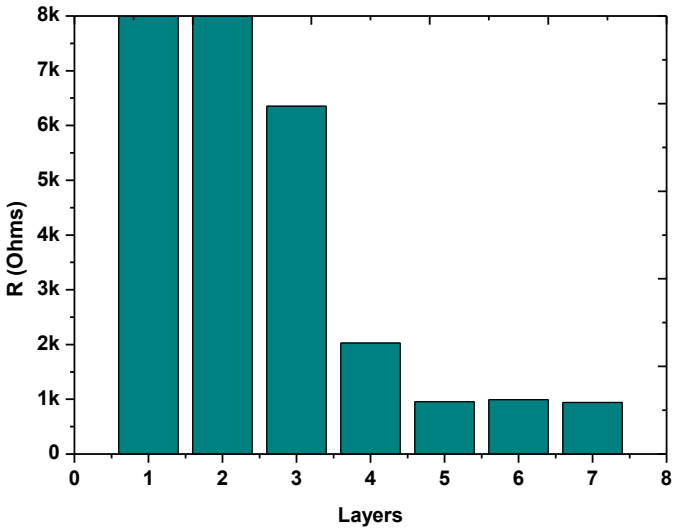

Figure 4.12. PEDOT:PSS coated yarns resistance versus number of coating layers.

4.9.2.2 Analysis of fabric results

Two groups of samples were prepared for this test. The first group consisted of fabrics coated with different number of layers of Panipol (from one to nine) and the other group consisted of those coated with PEDOT:PSS. After the fabrics were dried, surface resistivity was measured by using a concentric probe.

By applying each layer successively, the surface resistivity of panipol-coated fabrics dramatically decreased as showed in Figure 4.13. The limitation in this case is that we cannot apply too many layers on the fabrics because of the high viscosity of the polymer, so the optimum number of layers is two or three unless using a liquid polymer with low concentration.

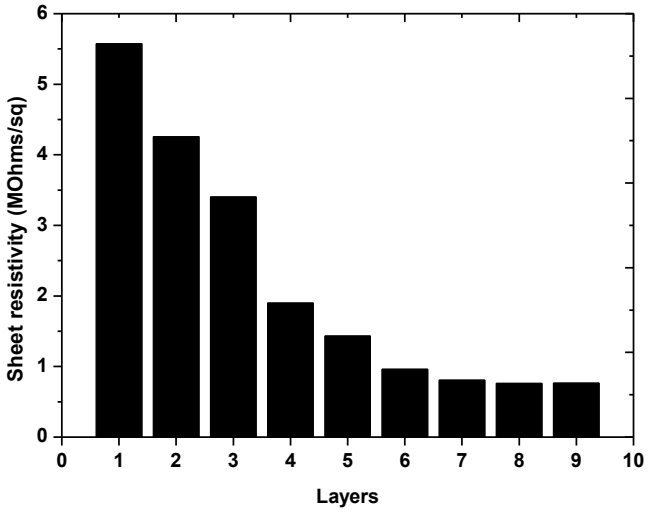

Figure 4.13. Surface resistivity of fabrics coated with different numbers of layers of Panipol .

Figure 4.14 shows the relation between the number of coating layers and surface resistivity for PEDOT:PSS coated fabrics. In general, surface resistivity is not as high as with Panipol, and as can be seen in the figure it reaches a low value after just 3 layers whereas it needs about 6 layers with Panipol.

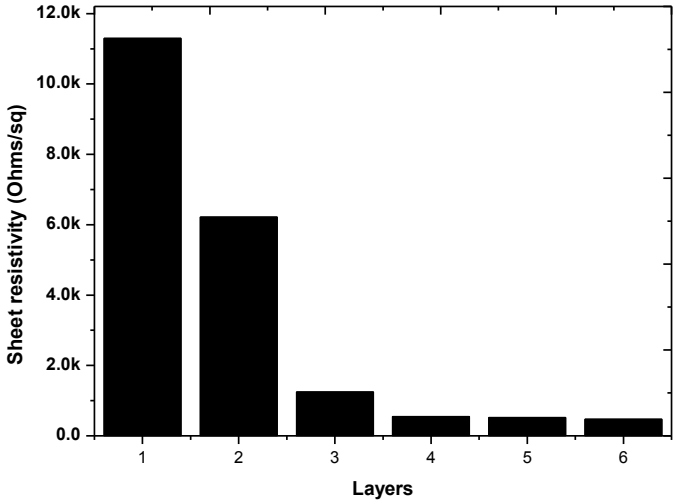

Figure 4.14. Sheet resistivityof fabrics coated with different layers of PEDOT:PSS .

4.9.2.3 Thermal annealing tests

This study evaluates the effect of temperature on the resistance of polymer coated conducting textiles. In terms of electrical properties, the fabrics must survive the silicon deposition process which requires the sample to be heated up to 200^{o}C and then maintains this temperature during deposition times of many minutes. The test was carried out in the vacuum chamber under Ar gas pressure of about 0.27 mbar. The results from this work will determine which polymer can maintain its electrical properties during the silicon deposition process.

4.9.2.3.1 Panipol coated fabrics

Changes in the resistance exhibited by the Panipol coated textiles during complete thermal cycling to 200^{o}C and back to room temperature are shown in Figure 4.15. The black and blue lines indicate one and two layer Panipol coating respectively. An initial improvement in the conductivities of the fabrics was observed for all samples, but as soon as the temperature was stabilized at 200^{o}C, the resistivity of the samples increased dramatically. It seems reasonable to say that the changes in Panipol resistance are related to thermally induced morphological changes and that the thin layer of Panipol tends to degrade quickly during the thermal treatment cycle. This is in agreement with the study by Chandrakanthi [19]. There has been improvement in the conductivity of conductive fabrics by applying a thicker layer of Panipol .

In order to evaluate the electrical behaviour of Aluminium/Panipol/fabric structures, samples are subjected to a similar resistance/thermal test. From Figure 4.16 it can be seen that the resistivity of sample fluctuated at temperature around 200^{o}C, but the aluminium film prevented the degradation of Panipol layers and the resistivity decreased to initial value as soon as the sample cooled down to the room temperature.

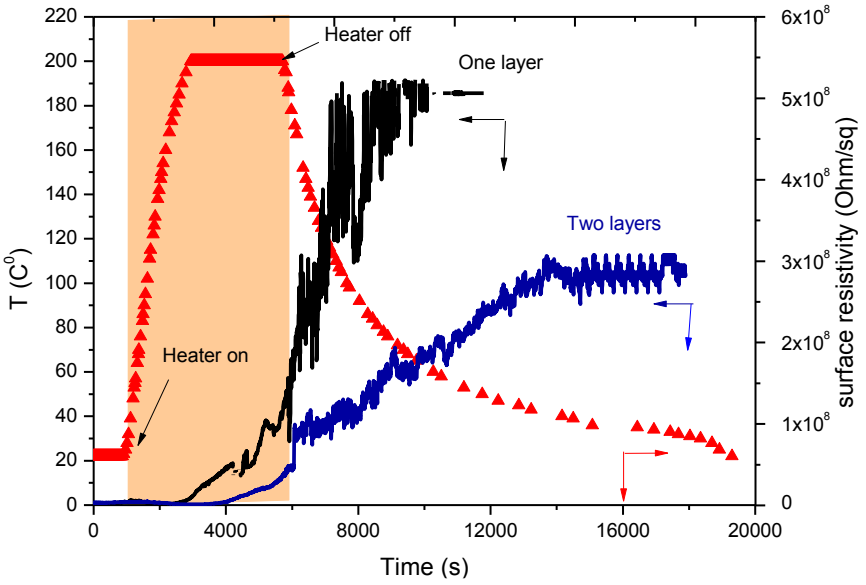

Figure 4.15. Surface resistivity changes for one and two layers of Panipol coated fabric during complete thermal treatment cycle to 200 ºC.

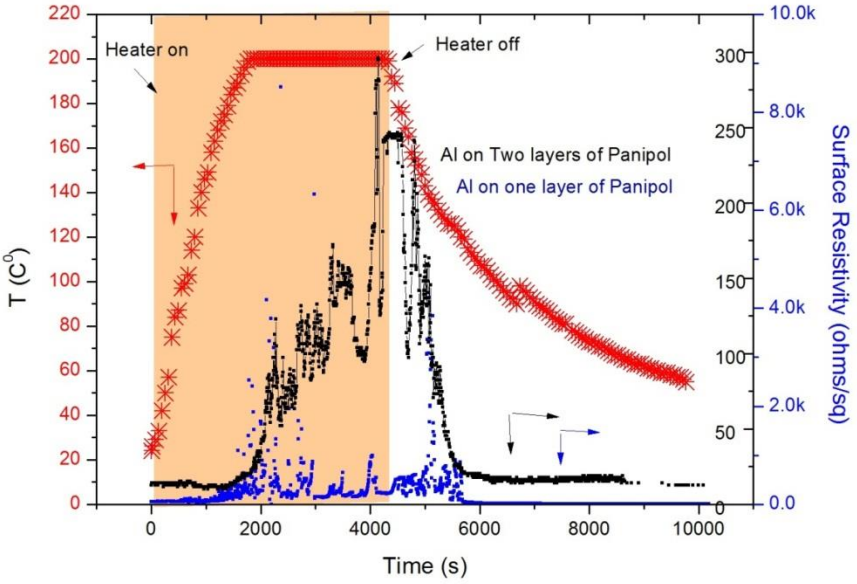

Figure 4.16. Surface resistivity changes for Aluminium on one and two layers Panipol coated fabric during complete thermal treatment cycle to 200 ºC.

4.9.2.3.2 PEDOT:PSS coated fabrics

The dependence of the PEDOT/PSS film conductivity on the treatment time at 200^{o}C in Ar is reported in Figure 4.17 (left). Despite the fluctuation of resistivity during heating, the resistance decreased dramatically as soon as the heater was switched off . This result indicates that the heating cycle to 200^{o}C does not affect the electrical properties of PEDOT:PSS. Another remarkable feature of the heat treatment can be observed from Figure 4.17 (right). The final resistance compared with the resistance prior to the thermal treatment gives an indication of the ability of the PEDOT:PSS to survive the heating cycle and maintain the conductivity of aluminium films. It has been reported that heating PEDOT:PSS up to 200^{o}C activates charge carriers and increases the crystallinity in the film, which leads in turn to improved conductivity of the polymer. However, if the temperature exceeds 250^{o}C, the film can be degraded and its resistivity increases [20, 21]. Moreover, the presence of the polymer in between the fabric substrate and aluminium film leads to improved stability of the dual contact layer during the complete thermal treatment cycle.

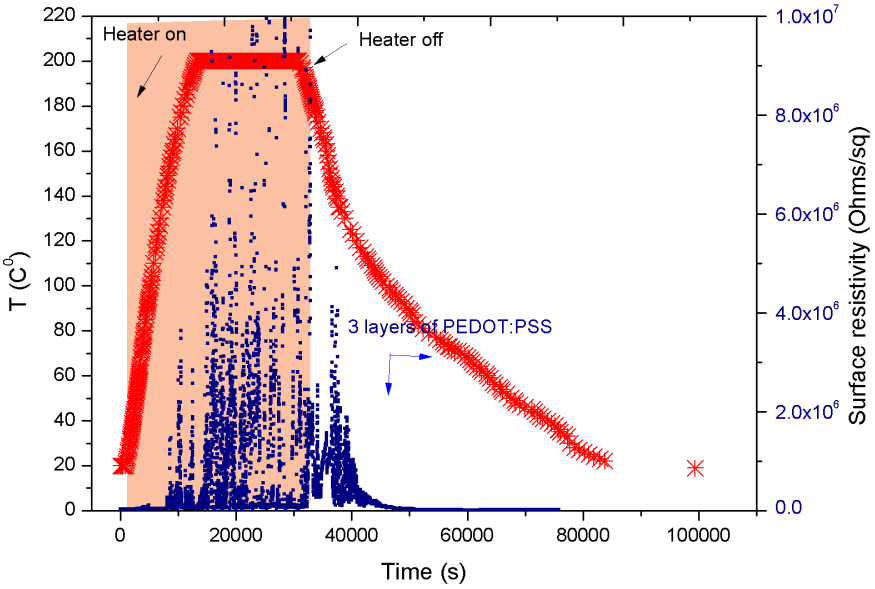

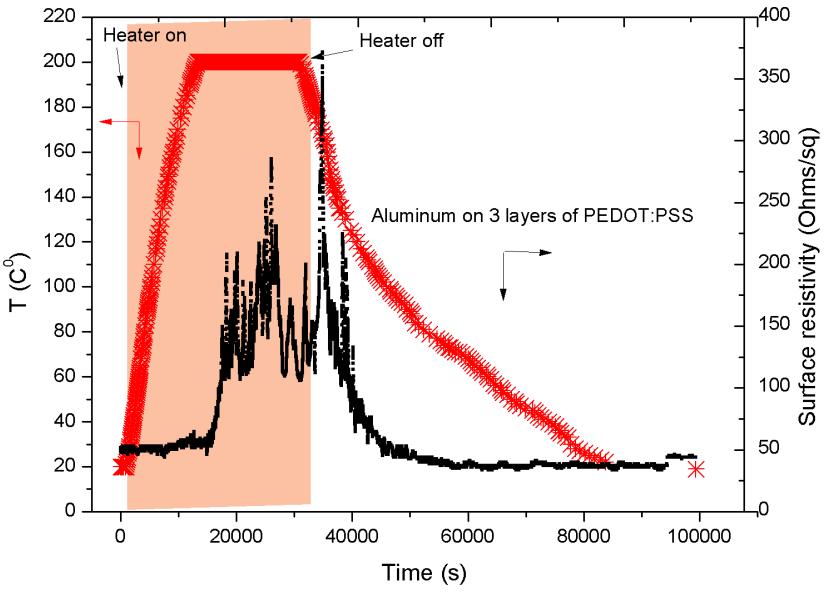

Figure 4.17. Surface resistivity changes for two layers PEDOT:PSS coated fabric, without and with aluminium, during complete thermal treatment cycle to 200 °C.

4.9.2.4 Polymer/metal contact resistance

The values obtained for contact parameters deduced from TLM are presented in Tables 4.1, and 4.2 ,where R_s, R_c are sheet resistance and contact resistance respectively and L_T is transfer length . The latter is a characteristic distance over which the current transfers from the metal contact pad to the semiconductor sheet or vice versa. Figure 4.18 shows the resulting characteristic curves (fitted lines) for the TLM structure; Al/Panipol coated fabric (right) and Al/PEDOT:PSS coated fabric(left). It can be seen that Al/Panipol contact resistance is very high compared to that of Al/PEDOT:PSS. Moreover, the measurements imply a lack of uniformity of sheet resistance across the sample due to the nature of the polymer structure and coating technique. The effects of the numbers of conductive coating layers on Al/polymer contact resistance are shown in Figure 4.19. As a result, contact resistance is improved by applying more layers of polymer.

Table 4.1. Values of electric parameters of selected Panipol coated samples.

Sample No	Layers	R_s(Ω/□)	R_c(Ω)	L_T(cm)	ρ_c(Ωcm^2)
G1-1	1	600K	167.7K	0.559	167.7K
G1-2	2	400K	123.03K	0.615	123.03K
G2-1	3	200K	101.88K	1.0188	207.6K

Table 4.2. Values of electric parameters of selected PEDOT:PSS coated samples.

Sample No	Layers	R_s(Ω/□)	R_c(Ω)	L_T(cm)	ρ_c(Ωcm^2)
G1-4	1	8.32K	640.6	0.15	640.6
G1-7	2	7.99K	86.45	0.0216	86.45
G2-8	3	36.66	46.3	2.33	216.17
G1-13	4	19.04	27.88	2.93	163.3

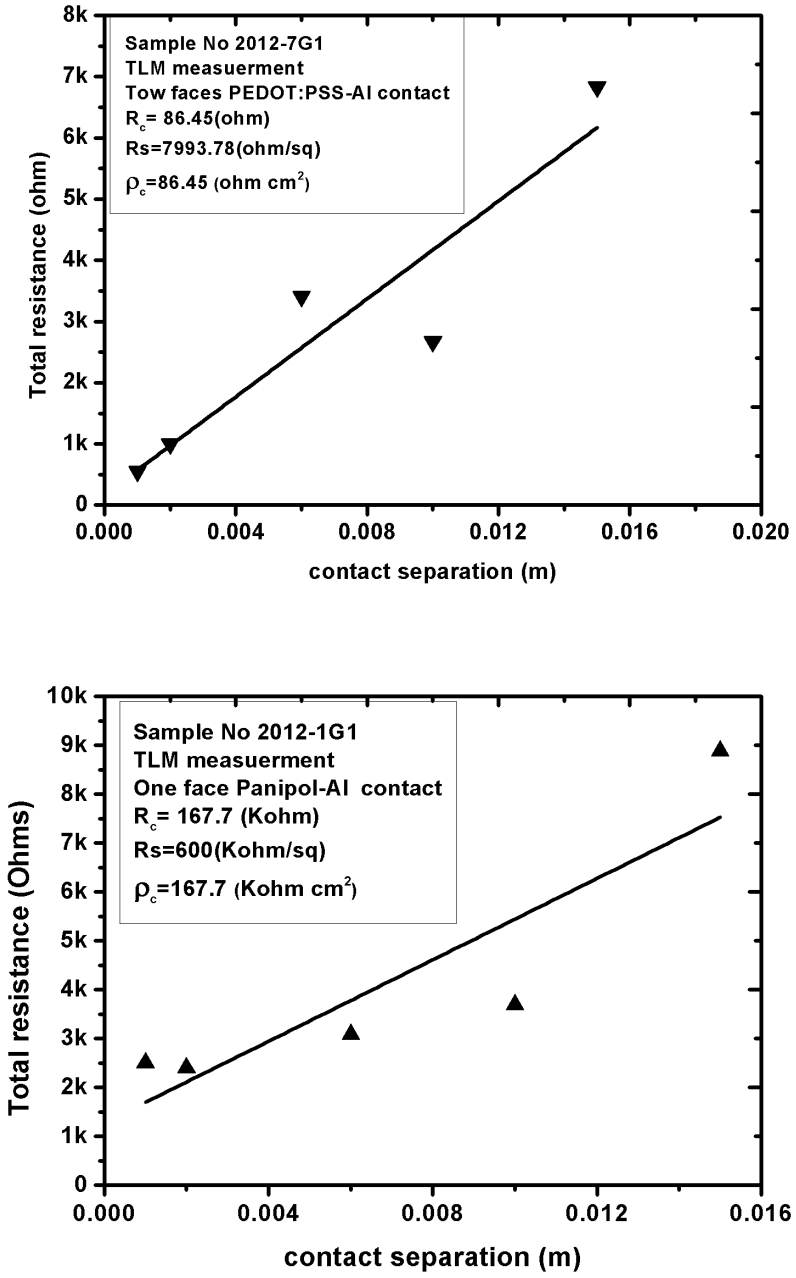

Figure 4.18. Resistance versus distance for PEDOT:PSS coated sample (Top graph) and Panipol (Bottom graph), (example).

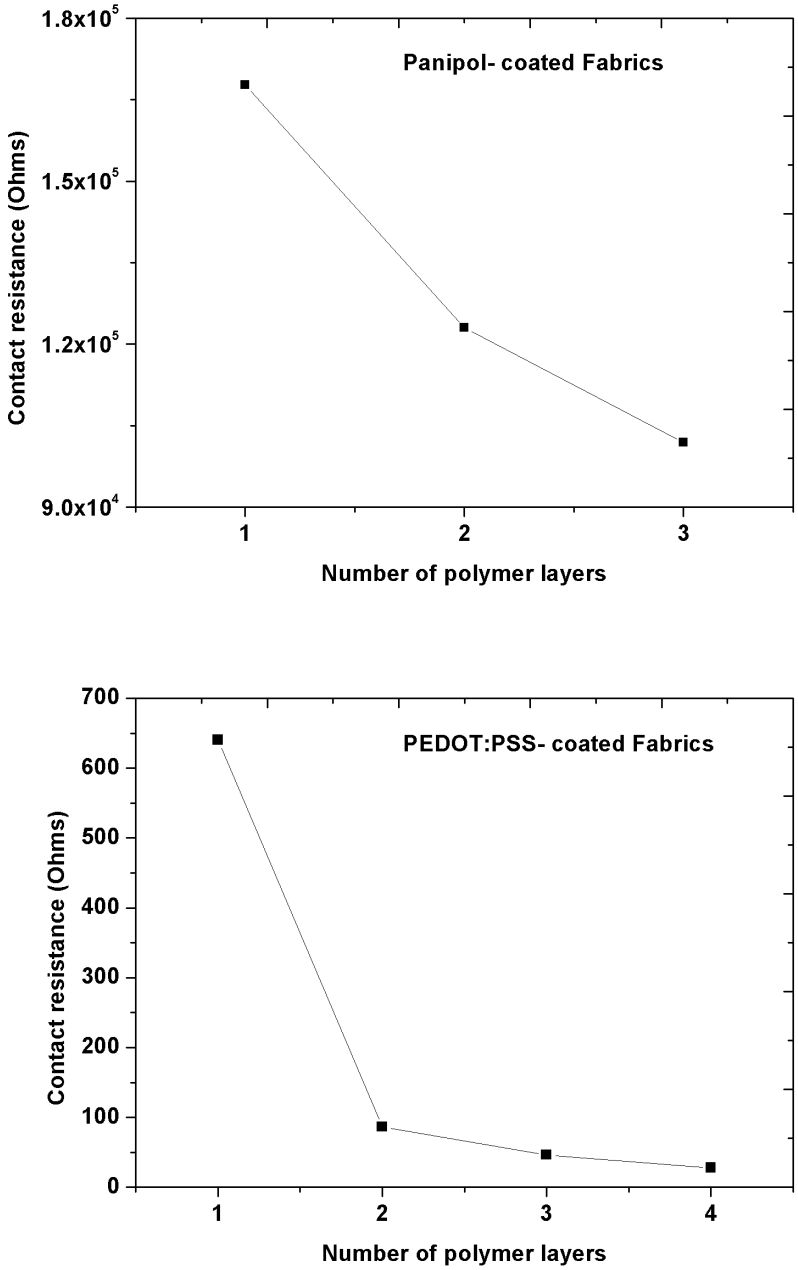

Figure 4.19. Aluminium / polymer contact resistance versus number of polymer layers for PEDOT:PSS (top garph) and Panipol (bottom graph).

4.9.2.5 Long term Stability test

The dependence of resistance on time at room temperature must be considered when using or even storing devices that use conductive polymer on a flexible substrate. It is also clear from our results that sheet resistivities of Panipol coated fabrics decreased dramatically over the first day test. After that, resistivities climbed back gradually to initial value during the second day of the test, as it can be seen in Figure 4.20. In

general, PEDOT:PSS showed good environmental stability over the period of the test as shown in Figure 4.21.

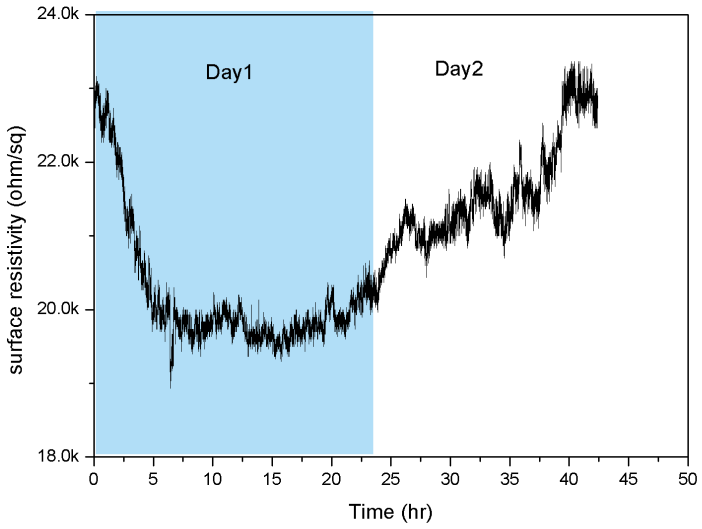

Figure 4.20. Time variations of surface resistivity of 2 layers of Panipol coated fabric in air ambient at room temperature.

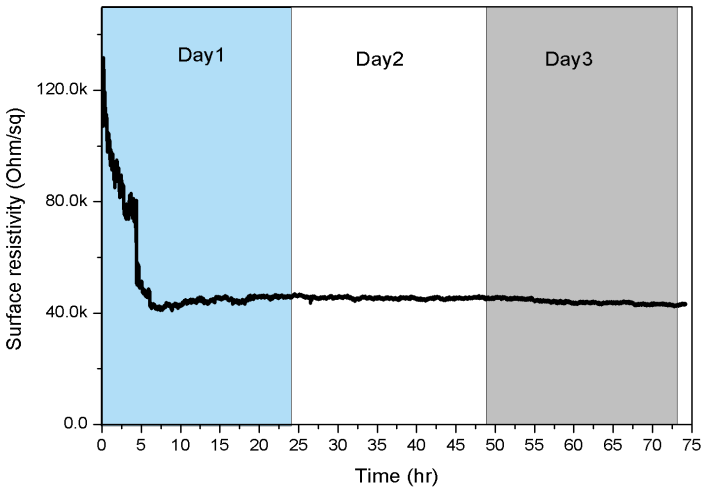

Figure 4.21. Time variations of surface resistivity of 3 layers of PEDOT:PSS coated fabric in air ambient at room temperature.

4.9.3 Bending test

4.9.3.1 Vigorous bending test

Figure 4.22 shows these bending test results for an Al / Panipol/ fabric sample. The resistance soared by 8-fold during the first bending cycle and it did not return to the initial value. Micro-cracks, microstructural damage or delamination, which was observed with the optical microscope, may be the main reasons for the increase in the electrical resistance. On the other hand, PEDOT:PSS not only maintained the conductivity of aluminium film, as can be seen in Figure 4.23 but actually improved it, an observation that is not fully understood at this point. The purpose of this test was to evaluate the effect of rough handling on the electrical properties of the coated fabrics and the results indicate that PEDOT:PSS has better stability under such harsh conditions.

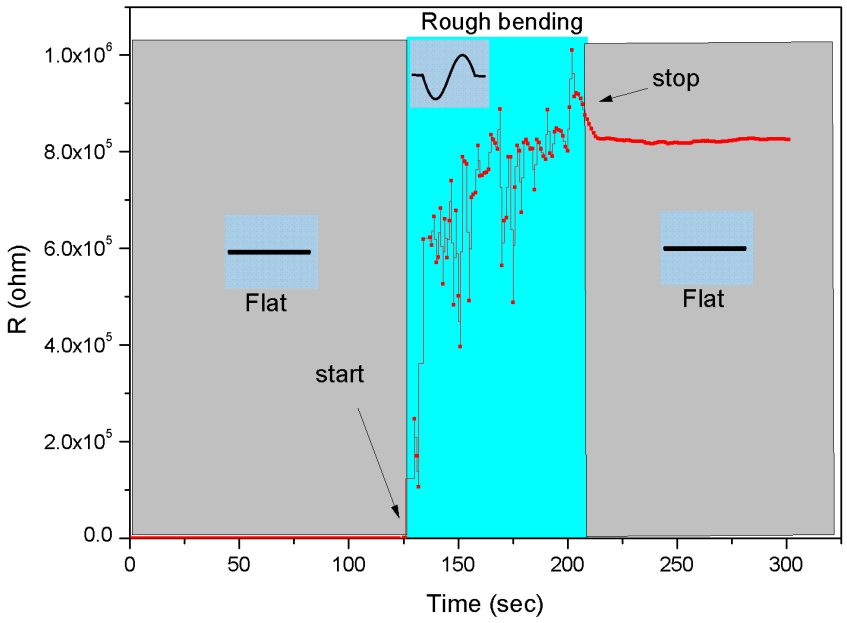

Figure 4.22. Vigorous bending test of Al/Panipol/ fabric sample.

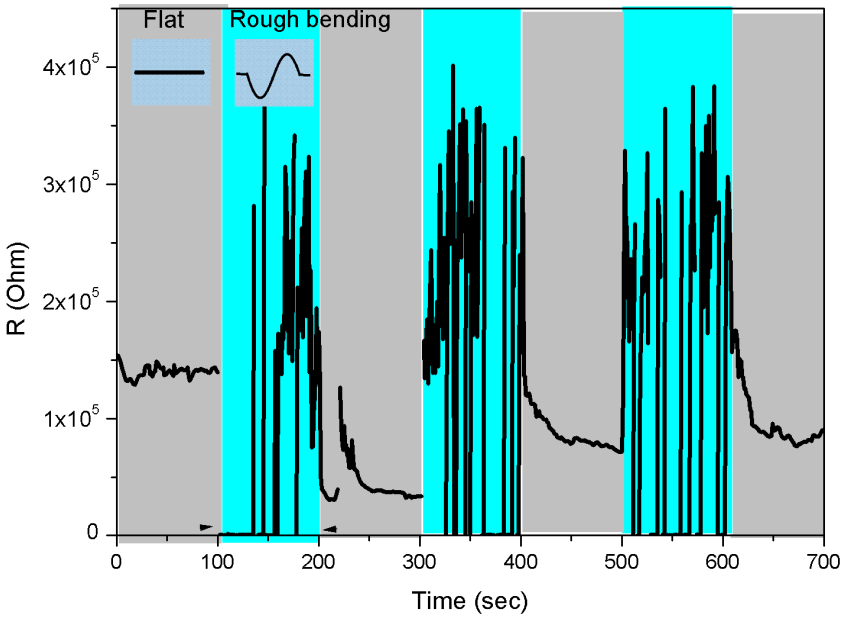

Figure 4.23. Vigorous bending test of Al/PEDOT:PSS/ fabric sample.

4.9.3.2 Systematic bending test

Figure 4.24 shows these bending test results for the Al/Panipol /fabric sample. The change of resistance is expressed as R over the range of bending angles starting from 180^{o} to 55^{o} in the first stage, and then back to180^{o} again in the reverse stage. The bending test results showed that at the initial stage (black squares), the electrical resistance of the bent sample did not significantly change down to a bending angle of 110^{o}. After this bending angle, the resistance began to increase gradually. However, it is noteworthy that the abrupt change in resistance value started at 110^{o}. Moreover, it can be seen that Panipol plays an important role in the structure so the aluminium film did not lose its conductivity. In the second bending stage (red squares), where the micro-cracks already exist, it is clear that the polymer almost maintains the conductivity of the metallic film and the difference between the initial and final values of resistance is due to the high resistance of Panipol itself.

Figure 4.25 shows the robustness of the Al/PEDOT:PSS/fabric structure against this severe bending. With decreasing bending angle from 180^{o} to 90^{o} , the resistance value of the sample increased gradually and the significant change started only at 90^{o} and

below. The remarkable result is that there are no huge differences between initial and final values of resistance in the first and second bending test stages. These results show a promising durability and electrical function in the PEDOT:PSS coated fabrics.

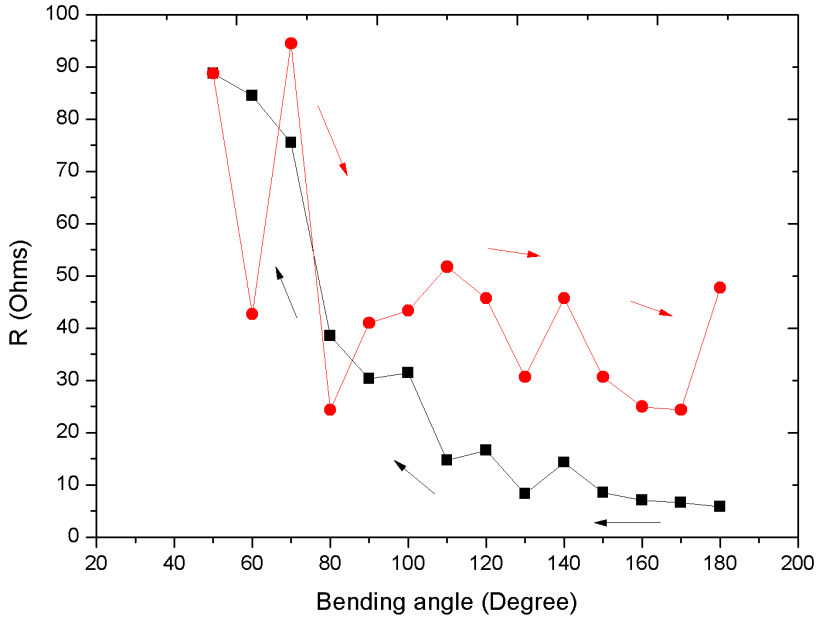

Figure 4.24. Bending reliability tests with changing bending angles off Al/ Panipol coated fabrics.

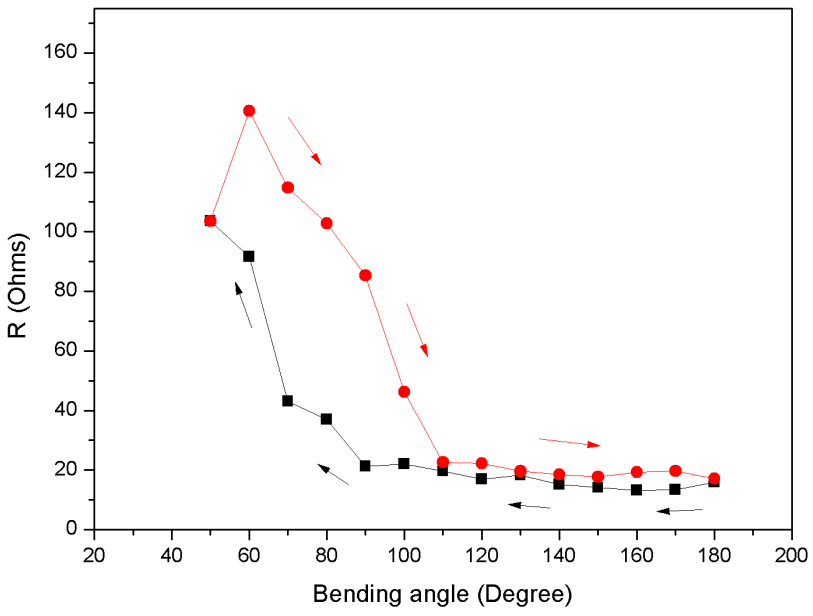

Figure 4.25. Bending reliability tests with changing bending angles of Al/PEDOT:PSS coated fabrics.

4.10 Conclusion

The project was focused on the study of electrical properties of polymer coated fabric which we aim to use as a back contact for solar cells or other applications. Coating yarns and fabrics by knife to table liquid coating with conducting polymer turned the fabrics into a conductive material. In order to achieve high quality conductive polymer on fabrics, four important treatment stages were reported in this work:

- Cleaning the fabrics to get rid of any impurities.
- Thermal calendaring of fabrics to make surfaces continuous across the weave sections.
- Plasma treatment of polyester fabric to improve polymer/fabric adhesion.
- Degassing the polymer to minimise bubble formation.

Mild air plasma does produce hydrophilic properties of the polyester textile surface. Surface resistance decreased with increasing amount of polymer on yarns or fabrics till a saturation level where the yarn and fabrics cannot cope with more polymer coats. The optimum amount of Panipol and PEDOT:PSS was considered but this still produced too much resistance in the contact for solar cells which required an over-coating of evaporated aluminium.

We demonstrate the difference in the electrical properties that results from heating in Ar . One reason for considering that is to know which polymer will survive similar heat treatment which is required for building thin film silicon solar cells on fabrics directly by using PECVD. As a result PEDOT: PSS exhibited better stability than the Panipol.

The results of TLM test for Al/Polymer showed that by using PEDOT:PSS instead of Panipol, the contact resistance decreased by 200-fold.

In addition, from the bending-resistance measurement using polymer coated fabrics, it was confirmed that using PEDOT:PSS enhanced the flexibility and stability of electrical contacts on the woven fabrics better than Panipol.

The dependence of resistance on time at room temperature for PEDOT:PSS showed improvement and stability in its conductivity over the period of the test whereas Panipol showed the opposite. We can confirm that these coated fabrics still possessed their former morphology and flexibility as well as electric conductivity of the polymer/metal contact.

4.11 References

1. Schubert MB, and Werner JH. *Flexible solar cells for clothing*. Materials Today. 2006;9(6):42-50.

2. Håkansson E, Amiet A, and Kaynak A. *Electromagnetic shielding properties of polypyrrole/polyester composites in the 1–18 GHz frequency range*. Synthetic Metals. 2006;156(14–15):917-25.

3. Madhusoothanan M, and Neelakandan R. *Electrical Resistivity Studies on Polyaniline Coated Polyester Fabrics*. Journal of Engineered Fibers and Fabrics. 2010;5(3):25-9.

4. Geetha S, Satheesh Kumar KK, and Trivedi DC. *Polyaniline reinforced conducting E-glass fabric using 4-chloro-3-methyl phenol as secondary dopant for the control of electromagnetic radiations*. Composites Science and Technology. 2005;65(6):973-80.

5. Dhawan SK, Singh N, and Rodrigues D. *Electromagnetic shielding behaviour of conducting polyaniline composites*. Science and Technology of Advanced Materials. 2003;4(2):105-13.

6. Wilson JIB, Mather R, Lind H, and Diyaf A. *Flexible solar cells on textiles*. Modern Energy Review. 2012;4(1):66-8.

7. Lind H, Wilson JIB, and Mather R. *Raman spectroscopy of thin-film silicon on woven polyester*. physica status solidi (a). 2011;208(12):2765-71.

8. Holik H, Gamsjäger N, Westerkamp A, Schmitt MW, Morton A, Stetter A, Tietz M, Feldmann R, Wohlfahrt M, and Mirsberger P. *Paper and Board Manufacturing*. *Handbook of Paper and Board*: Wiley-VCH Verlag GmbH & Co. KGaA; 2006. p. 219-331.

9. Shishoo R. *Plasma technologies for textiles*.Cambridge: Woodhead Publications; 2007.

10. Radetić M. *Functionalization of textile materials with silver nanoparticles*. J Mater Sci. 2013 2013/01/01;48(1):95-107.

11. Kale K, Palaskar S, Hauser PJ, and El-Shafei A. *Atmospheric pressure glow discharge of helium-oxygen plasma treatment on polyester/cotton blended fabric*. Indian Journal of Fibre and Textile Research 2011;36(2):137-44.

12. BS6524. *British Standard Method for Determination of Surface Resistivity of a Textile Fabric*. 1984 1984.

13. 76-2005 Atm. *Electrical Resistivity of Fabrics*.2010.

14. ASTM. Standard D257-99. *Standard test methods for D-C resistance or conductance of insulating materials*. 1999.

15. 257-91 AD. *Standard test methods for D-C resistance or conductance of insulating materials*. 1991.

16. Schroder DK, andMeier DL. *Solar cell contact resistance. Electron Devices*, IEEE Transactions on. 1984;31(5):637-47.

17. Dobrzański LA, Musztyfaga M, Drygała A, and Panek P. *Investigation of the screen printed contacts of silicon solar cells using trans*. Journal of Achievements in Materials and Manufacturing Engineering. 2010;41(1-2):57-65.

18. Blinova NV, Stejskal J, Fréchet JMJ, and Svec F. *Effect of reaction conditions on film morphology of polyaniline composite membranes for gas separation*. Journal of Polymer Science Part A: Polymer Chemistry. 2012;50(15):3077-85.

19. Chandrakanthi N, andCareem MA. *Thermal stability of polyaniline*. Polymer Bulletin. 2000 2000/02/01;44(1):101-8.

20. Aasmundtveit KE, Samuelsen EJ, Pettersson LAA, Inganäs O, Johansson T, and Feidenhans'l R. *Structure of thin films of poly(3,4-ethylenedioxythiophene)*. Synthetic Metals. 1999;101(1–3):561-4.

21. Huang J, Miller PF, de Mello JC, de Mello AJ, and Bradley DDC. *Influence of thermal treatment on the conductivity and morphology of PEDOT/PSS films*. Synthetic Metals. 2003;139(3):569-72.

Chapter 5 Characterisation of solar cell layers

5.1 Introduction

In solar cell research, it is important to study the properties of each layer in terms of their optical and electrical properties to achieve high performance. For the present investigation, both single and stacked metal contact layers and thin silicon films are built on glass and flexible substrates for optical and electric characterisation. The aim of this Chapter is to lay out the relevant processes to better understand the experimental work related with manufacturing the amorphous silicon solar cells which are presented in the subsequent chapters. It is important to examine the available manufacturing facilities based at HWU in terms of the quality of thin films such as TCO, aluminium, and amorphous silicon.

In the first part, the types of substrates and cleaning procedure are briefly discussed. Then optical and electrical properties of metal and transparent conductive oxide contacts have been studied. Finally, intrinsic and doped layers of hydrogenated amorphous silicon have been studied in terms of electrical and optical properties and their dependence on deposition conditions.

5.2 Substrates and cleaning procedure

Glass slides of dimension 2.5 cm x 7.5 cm, silicon wafers, polytetrafluoroethylene (PTFE) fabric, and polyester fabrics were used as supports for thin films. Considering a single layer thin film, using glass as a substrate facilitates both optical and electrical measurements.

The purity of any deposited films not only depends on purity of the material source delivered to the reaction chamber, and the leakage in the system, but also it is widely believed on the substrate cleaning procedure. So substrate cleaning is one of the most important stages of any thin film production process and it plays an important role in film quality. There are many different methods for substrate cleaning which give good results [1].

The following procedure was used in our work:

1- Ultrasonically clean in Acetone for 30 minutes to remove grease.
2- Ultrasonically clean in Isopropanol for 30 minutes.
3- Ultrasonically clean in 1% Decon for 30 minutes.
4- Rinse in flowing deionised water for 15 to 20 minutes.
5- Dry for 30 minutes in an oven heated to about 150^0C

When satisfied that the samples are clean then transfer to sputter or evaporation unit to deposit the back contact of Aluminium or ITO. After that, the samples are ready to transfer to the amorphous silicon reactor chamber.

5.3 Conductive contacts for solar cells

5.3.1 Aluminium

Aluminium can be evaporated or sputtered to form back or top contacts for solar cells. In this work, an Edwards E306A vacuum system was used to evaporate aluminium with different thickness onto glass substrates. Aluminium was evaporated in a vacuum chamber via resistive evaporation, by which a large current is passed through a tungsten coil loaded with aluminium filaments. The chamber was pumped down to a base pressure of $1x10^{-6}$ mbar prior to the process. That is to avoid the oxidation of aluminium to improve the quality of the aluminium contacts. In order to study quality of the aluminium films, a set of samples with aluminium thicknesses of 25, 50, 70, and 100 nm were prepared. Sheet resistivity was measured by using four-point probe testing instrument Suzhou SZT-2A. Figure 5.1 presents measured sheet resistivity as a function of aluminium film thickness. It shows that with increase of thickness of aluminium films, the resistivity decreases as expected. This improvement in electrical conductivity is due to charge carrier increases with the film thickness. This can be attributed to reduction in the electron mean free path due to size effects. Unlike the properties of bulk materials, electrical properties in the thin film depend on several factors such as rate of deposition, thickness, and substrate temperature, which determine the grain sizes and their boundaries, thus affecting the carrier mobility [2].

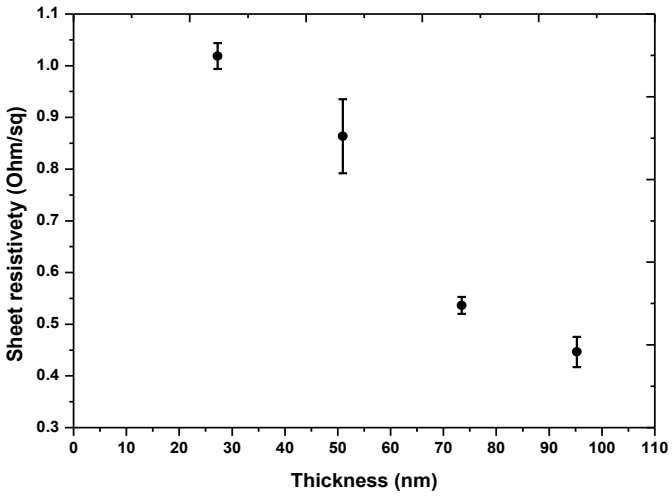

Figure 5.1. Aluminium sheet resistivity with different thicknesses.

5.3.2 Transparent Conductive Oxide

The properties of sputtered ITO films are strongly dependent on the deposition conditions, such as substrate temperature, the distance between the target and the substrate, plasma power, and oxygen partial pressure. In this section, we will study the effects of thickness, plasma power and distance between target and substrate on the properties of ITO film. High quality ITO can be sputtered without introducing any oxygen into the growth environment [3, 4].

5.3.2.1 Experimental details

Experimental work can be divided into three parts. The first is to examine the effects of the thickness of ITO films on the optical and electrical properties of the films. The ITO films were deposited by RF sputtering using an Edwards AUTO 360 system as described in chapter 3. The chamber was pumped down to a base pressure of 1.8×10^{-6} mbar prior to the process. Sputtering was carried out in argon atmosphere at a pressure of 1×10^{-4} mbar. A 13.56 MHz RF power supply was used to provide the RF excitation. Plasma was generated with power of 70W and the substrates were kept at a distance of 14.7 cm above the target.

ITO films with different thickness were deposited on microscope slide glasses of dimension 2.5cm x 7.5 cm and the target was sputtered for 5,10,15,20,30, and 45 min. In the second part, the effect of plasma power was examined so ITO films were deposited on glass substrates under processing pressure of $1x10^{-4}$ mbar and the RF power was varied in the range 10W to 90W. Finally, the effects of sputtering target to substrate distance on the quality of the ITO films was examined by fixing all sputtering parameters and changing target- sample distance as follows: 6.1cm, 14.7cm, and 24.7cm. For all experiments, the optical and electrical measurements were performed as discussed below.

5.3.2.2 Effect of the Film Thickness on the Properties of ITO Films

Ellipsometric parameters Ψ and Δ over the wavelength range of 300-1000nm were measured at three angles of incidence 50^o, 60^o and 70^o using Variable Angle Spectroscopic Ellipsometry (VASE)[5]. In order to calculate the desired values such as layer thickness and optical constants from the measured data, a suitable optical model has to be applied. ITO films can be modelled by using different types of mathematical models such as the Cauchy model which can give good fit in the visible range (500-700nm), also the Lorentz oscillator model can be applied with more exact fits over a wider spectral range, especially by adding a graded profile [6]. In this case, one and two sets of graded Lorentz oscillators were used to cover both the transparent and absorbing spectral range.

As an example, Figure 2.2 shows as an example ellipsometric data and fit for the range of 300-1000nm. In this sample, the ITO film thickness was determined to be 122.5±0.4 nm. A graded profile was used to model the ITO optical constants as shown in Figure 5.3. It can be seen that the extinction coefficient is lower at the bottom of the film, which suggests that the ITO film is more conductive at the film air interface. During the sputtering process, the density of the film is increased gradually so the film became more conductive at the top where the film is more continuous. This can enhance the film electrical conductivity at the film-ambient interface [6].

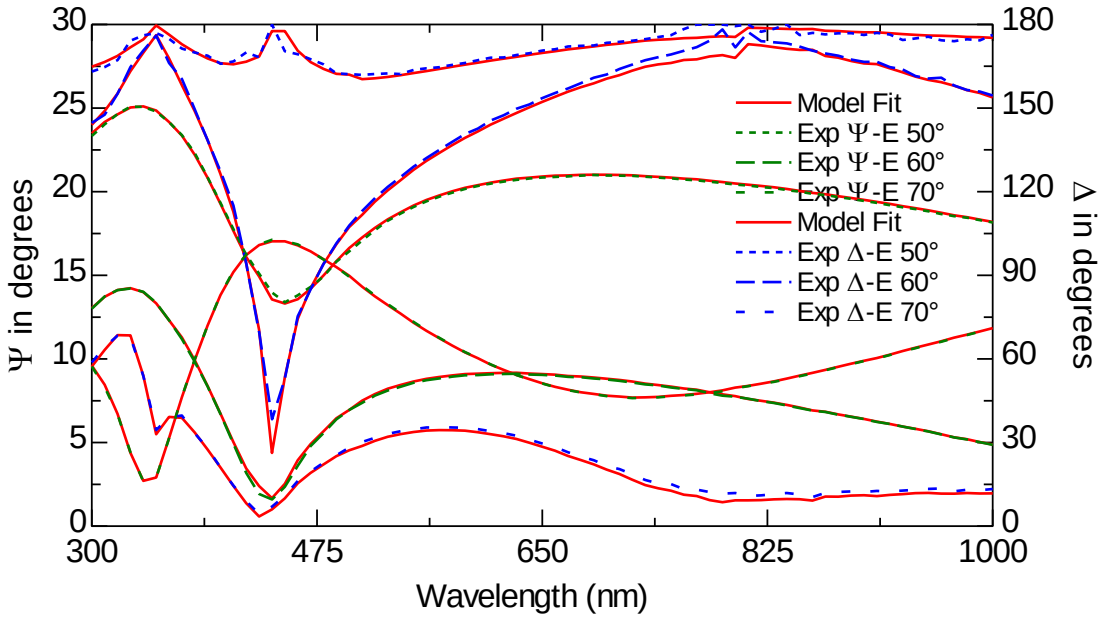

Figure 5.2. Transmittance spectra of different thickness of ITO films.

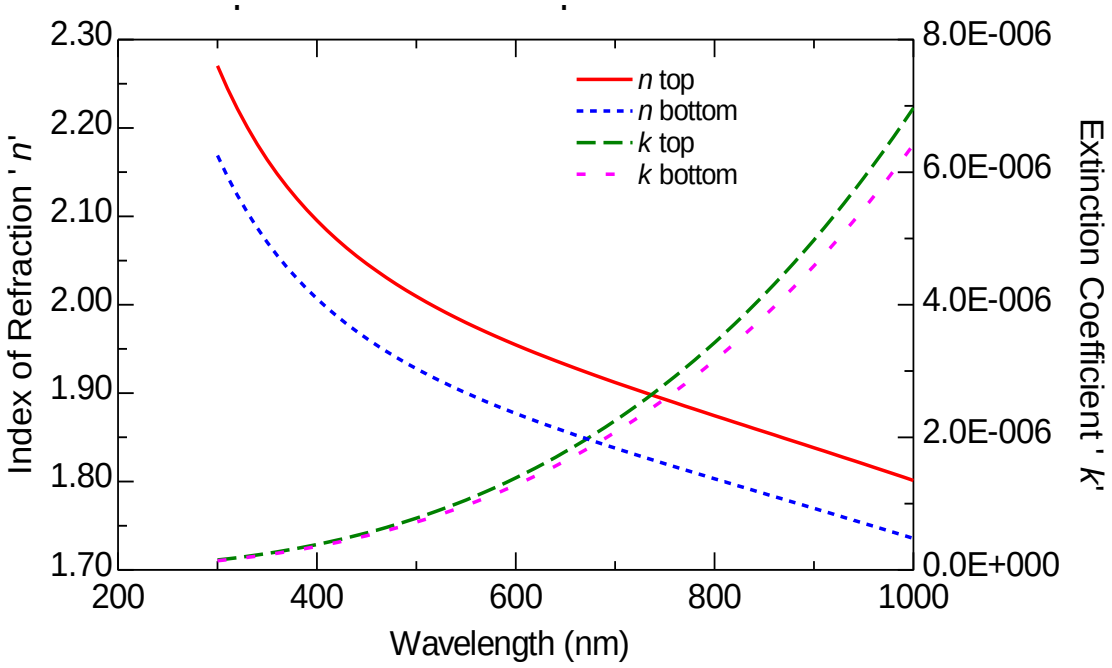

Figure 5.3. Refractive index and extinction coefficient at the top and bottom of ITO films.

The transmittance measurements were carried out in the UV-VIS spectrometer; details of these measurements are described in chapter 5.3. Figure 5.4 shows the transmittance of selected films with different thickness over the wavelength range 200 to 2400nm. It

is observed that in the visible range of the spectra (400nm to700nm), the film with thickness 122.6± 0.4nm shows good transmittance and the transmittance decreases with increasing the thickness of the films as expected. Average transmittance over the 400 - 1000 nm optical region of ITO thin films is presented in Figure 5.5. It can be noticed that around 80% transmittance is achieved for the range 400 to 1000nm for samples with thickness around 122.6± 0.4 nm, also the film loses its transparency with average 65% when becoming thicker (270nm). It is clear that the transparency of the film is determined both by film structure and thickness. Also thickness and stoichiometry.

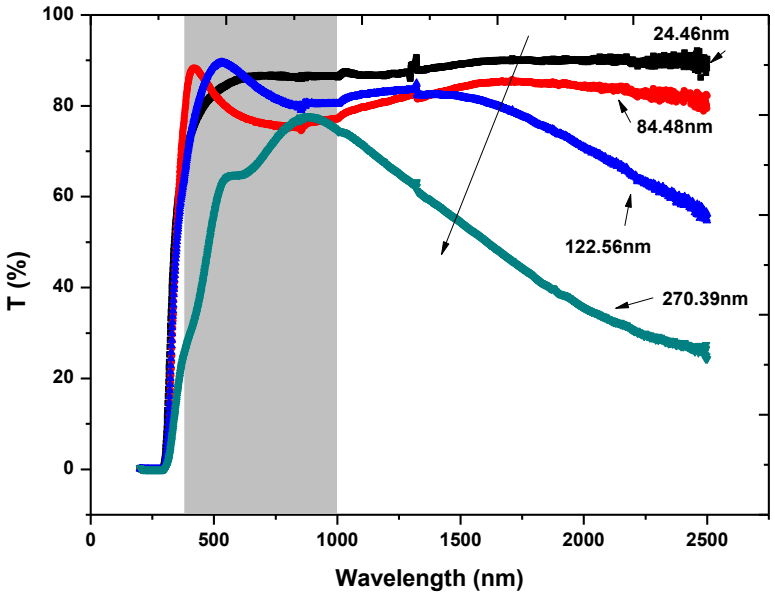

Figure 5.4 .Transmittance spectra of different thickness of ITO films.

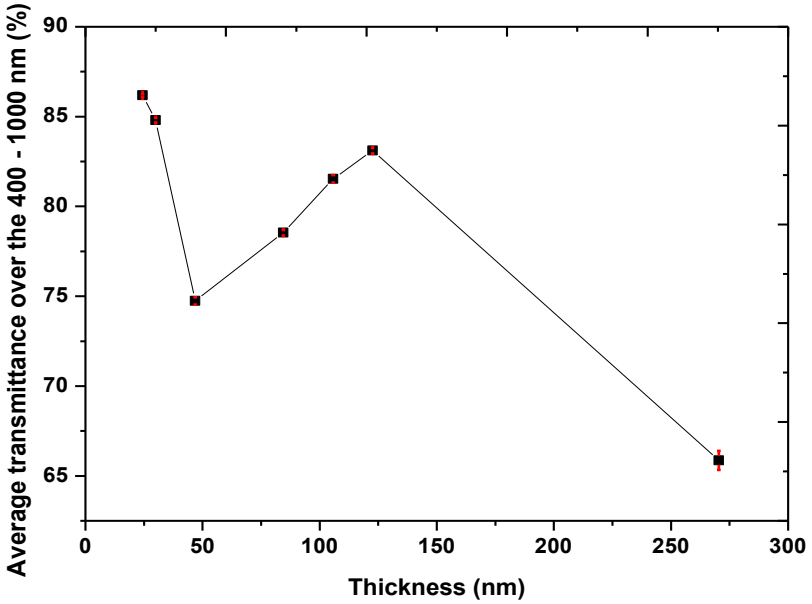

Figure 5.5. Average transmittance over the 400 - 1000 nm optical region of ITO thin films deposited with various thicknesses. The black line is a guide for the eye.

Changing the carrier concentration can increase or decrease the optical band gap in degenerate semiconductors such as doped ZnO and ITO. Many studies have reported that the band gap widens by increasing film thickness which in turn increases carrier concentration [7, 8]. However, in our case, the optical band gap narrowed by increasing the thickness of the ITO films. As shown in Figure 5.6, the band gap energy decreases when the film thickness increases. This is in agreement with the result of some previous studies [9, 10]. When the carrier concentration exceeds a critical value, the band gap tends to narrow because of (1) the merging of donor and conduction bands, (2) band tailing by impurity-induced potential fluctuations and (3) electron-electron and electron impurity scattering [11-13].

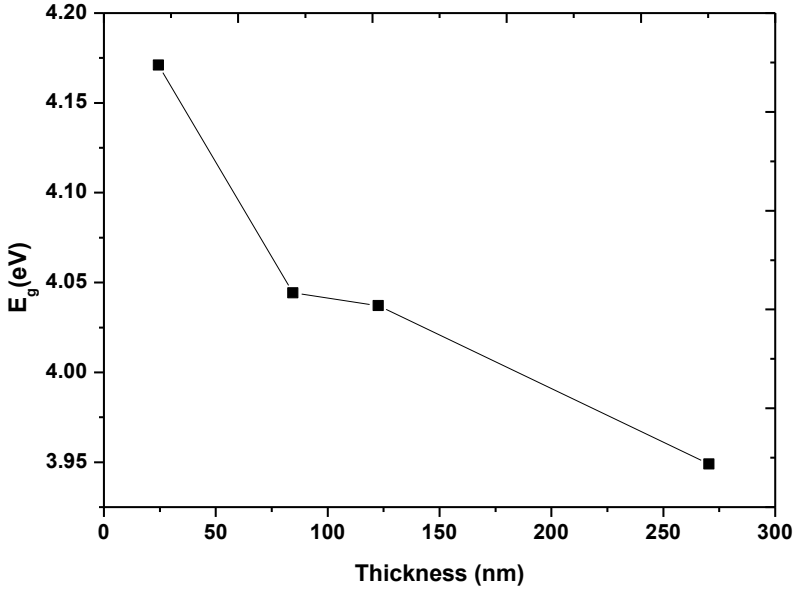

Figure 5.6. Variation of energy gap (Eg) of ITO films with varying film thickness. The black line is a guide for the eye.

Four-point probe measurements were performed on ITO samples and the results are listed in Table 1 which includes film thicknesses obtained by using the ellipsometer. The result showed a 66-fold decreased sheet resistivity of ITO films by increasing thickness from 24.4nm to 270.4nm. This shows that for a given set of deposition conditions, the thicker film has better electrical properties. These results are consistent with the findings of Lei Hao [14].

It can be seen in Figure 5.7 that the decrease in sheet resistance is rapid when the film thickness increases from 20 nm to 80 nm, whereas this decrease is very slow when the thickness is greater than 100 nm. The minimum sheet resistivity is about 57.6 Ω/□ for the film with thickness 270.4nm. This improvement in electrical conductivity with increasing of thickness could be attributed to improvement in film crystallinity and increase in grain size of the films which in turn lead to increasing the carrier mobility [14-16].

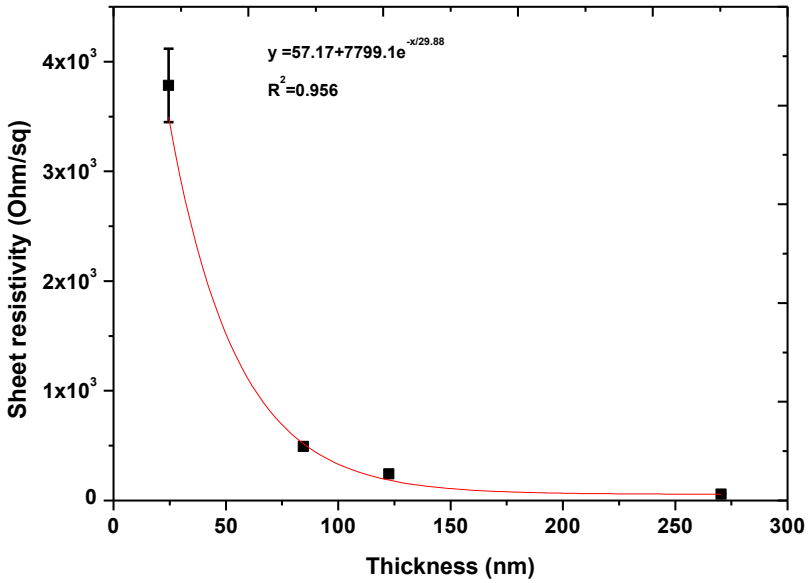

Figure 5.7. Dependence of sheet resistivities of ITO films on thickness. The red line is fitted.

Table 5.1. Effect of thickness on properties of ITO films deposited under identical conditions.

Sample	Exposure Time(min)	Plasma power (watt)	Pressure (mbar)	Film thickness (nm)	Sheet resistivity (Ω/sq)	Resistivity Ω-cm	Optical band gap
T1	5	70	$1x10^{-4}$	24.4±0.4	3783.1	$9.25x10^{-3}$	4.17
T2	15	70	$1x10^{-4}$	84.5±0.9	493.5	$4.18x10^{-3}$	4.04
T3	30	70	$1x10^{-4}$	122.6±0.4	241.9	$3.01x10^{-3}$	4.03
T4	45	70	$1x10^{-4}$	270.4±1.5	57.6	$1.49x10^{-3}$	3.95

5.3.2.3 Influence of RF power on the Properties of ITO Films

ITO films were deposited on glass substrates at room temperature. The base pressure in the chamber was $2x10^{-5}$ mbar. A 13.56 MHz RF power supply was used to provide the RF field and plasma power was varied from 10 to 90 watts. The substrates were kept at a distance of 14.7cm above the target and all deposition time were 20min.

Ellipsometry was used to determine thickness of the films and the results are summarized in Table 5.2. Figure5.8 shows variation of thickness of ITO thin films as a function of RF power. The thickness increases dramatically with increase in plasma power. It is indicated that the deposition rate increases almost linearly with increasing sputtering power. Increasing plasma power increases the energy of sputtered atoms and highly energetic bombardment particles. This reduces the density of defects and improves the growth of the film [17, 18].

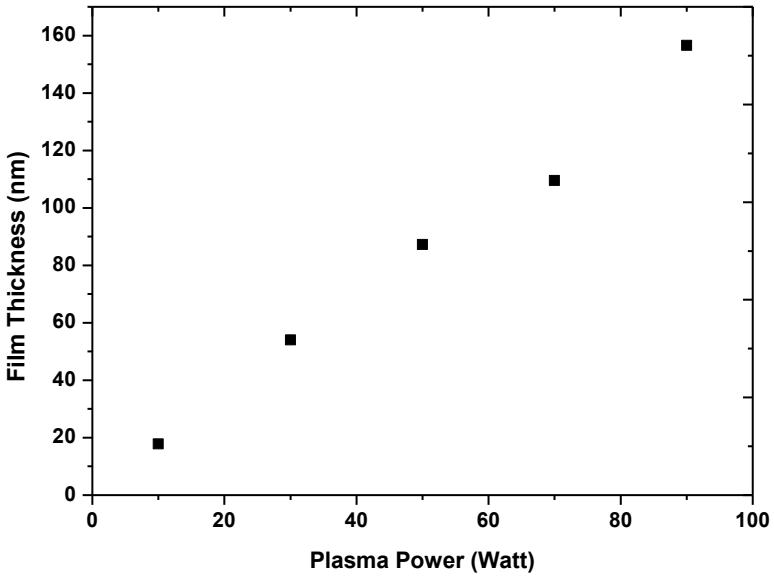

Figure 5.8. Variation of thickness of ITO thin films as a function of RF power.

The transmission spectra of ITO films with different sputtering powers are shown in Figure 5.9. It is observed from the transmission spectrum that the films in general are highly transparent throughout the visible region also the films have a strong absorption in the UV region which is caused by the excitation across the band gap E_g.

Average transmittance over the 400 - 1000 nm optical region of ITO thin films with different RF power is presented in Figure 5.10. The average transmittance in that range of the electromagnetic spectrum was above 85%.

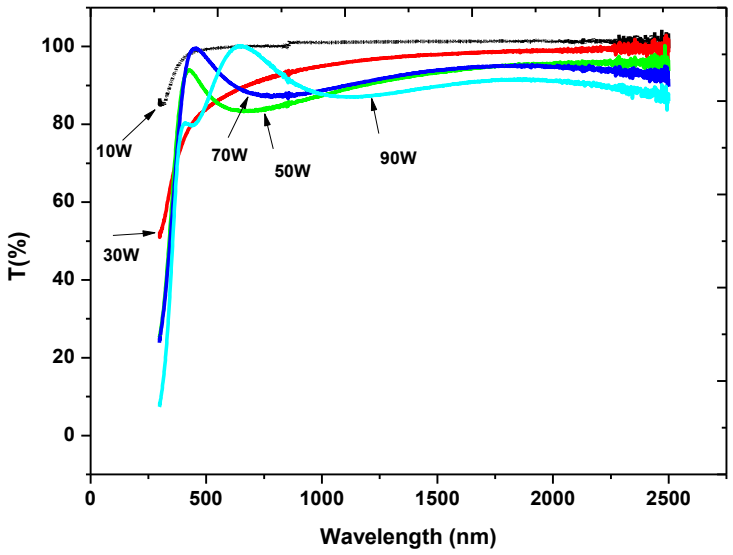

Figure 5.9. Transmission spectra of ITO films with sputtering power 10, 30, 50,70 and 90 W, respectively.

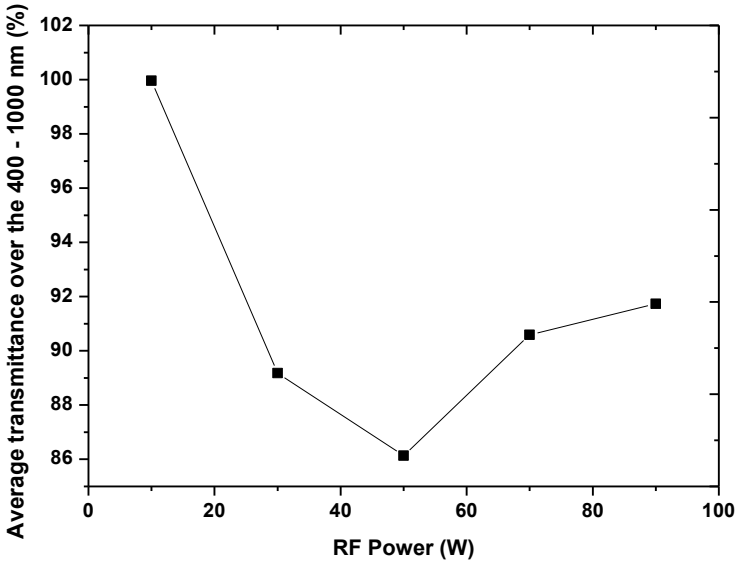

Figure 5.10. Average transmittance over the 400 - 1000 nm optical region of ITO thin films deposited with various RF powers. The black line is a guide for the eye.

The optical band gaps were determined from the plot of $(\alpha E)^2$ vs photon energy (equation 2.2) by extrapolating the linear portion of the curve to $(\alpha E)^2$ equal to zero as shown in Figure 5.11 (as example), where α is the absorption coefficient and E is photon energy. In this study, the band gaps of the ITO films were calculated from the transmission spectra for different RF powers (Figure 5.12). As a result, the band gap decreased with increasing in RF power up to 30W and then increased. This can be attributed to the Burstein - Moss shift which is due to the filling of the states near the bottom of the conduction band [19].

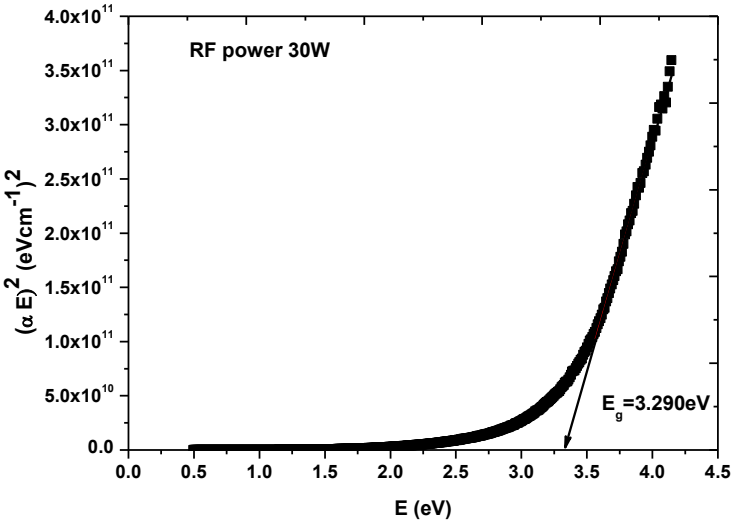

Figure 5.11 . Plot of $(\alpha h\nu)^2$ vs. Photon energy for selected ITO film growth by RF power of 30W.

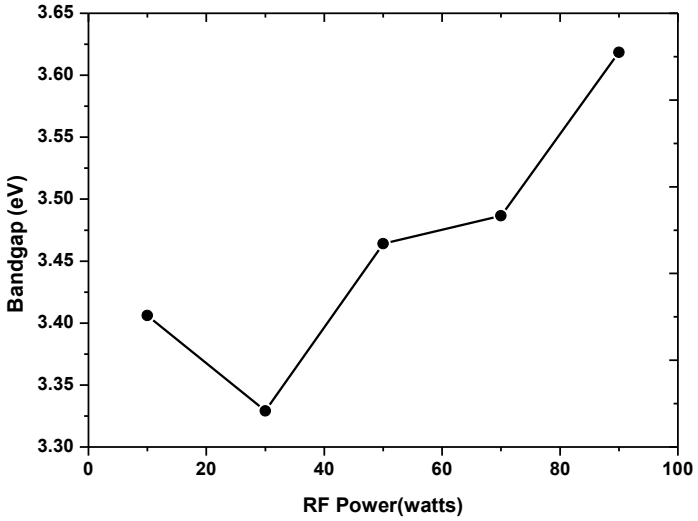

Figure 5.12 .Variation of band gap of ITO thin film as a function of RF power. The black line is a guide for the eye.

The sheet resistivity of the ITO films was determined by employing four-point probe technique. As can be seen in Figure 5.13, the resistivity decreased with increase in plasma power. As a result of increasing RF power, thickness of the films increased (see Figure 5.8). Consequently, sheet resistivity decreased. This behaviour may be due to increase of crystallite size and carrier concentration [20]. The minimum sheet resistivity around 100Ω/□ was obtained for the films deposited at the highest RF power of 90W. Table 5.2 summarises the important properties of ITO thin films which were obtained in this part as a function of RF plasma power.

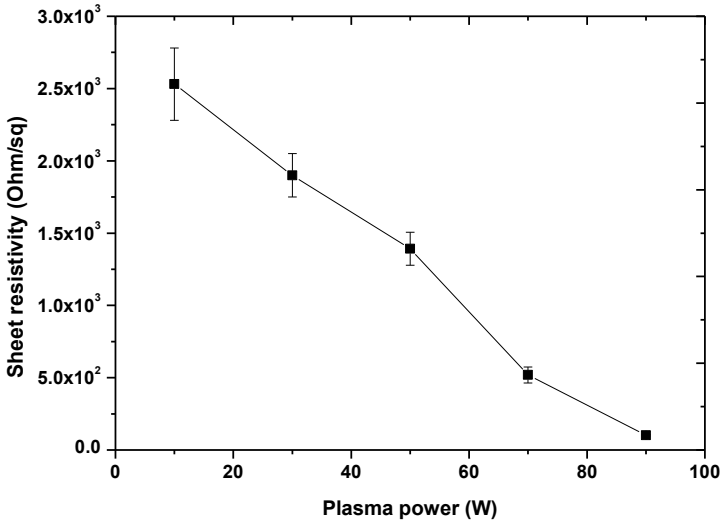

Figure 5.13 .Variation of sheet resistivity of ITO thin film as a function of RF power. The black line is a guide for the eye.

Table 5.2. Effect of plasma power on properties of ITO films.

sample	Exposure Time(min)	Plasma Power (w)	Pressure (mbar)	Film thickness (nm)	Sheet resistivity (Ω/sq)	Optical band gap (eV)
P11	20	10	$1x10^{-4}$	17.8±1.90	2530.7	3.41
P12	20	30	$1x10^{-4}$	54.0±1.85	1900.0	3.33
P13	20	50	$1x10^{-4}$	87.3±1.64	1392.0	3.46
P14	20	70	$1x10^{-4}$	109.5±0.55	519.1	3.49
P15	20	90	$1x10^{-4}$	156.6±3.00	101.9	3.62

5.3.2.4 Effect of Target to Substrate Distance

To investigate the influence of ITO target to glass substrate distance on ITO film properties, the following deposition conditions were applied: $1x10^{-4}$ mbar Argon pressure, RF power 70W, and target-substrate distance was 6.1, 14.7 and 24.7 cm. Figure 5.14 shows transmission spectra of ITO thin films deposited at various target-substrate distances. Transparency of the film increased by increasing target- substrate distance and average transmittance over the 400 - 1000 nm reached 98% when the substrate was located at 24.7cm from the ITO target as shown in Figure 15. This could be explained by the fact that deposition rate decreased with increase of target- substrate distance [21, 22]. As it can be seen in Figure 5.16, the ITO film becomes thinner as it is moved away from the target.

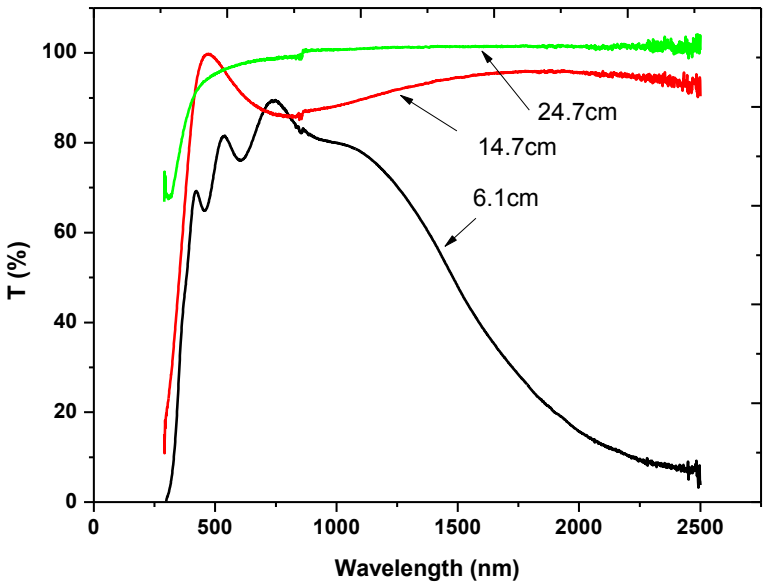

Figure 5.14. Transmission spectra of ITO thin films deposited at various target-substrate distances.

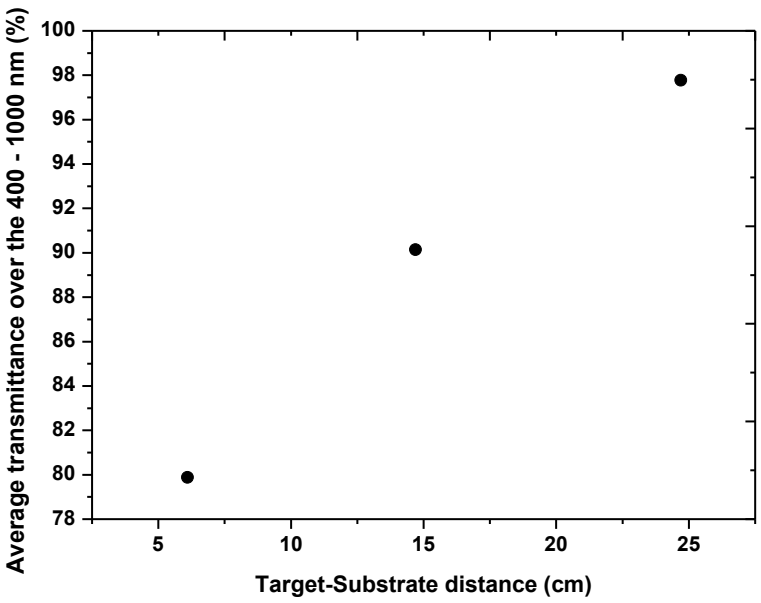

Figure 5.15 . Average transmittance over the 400 - 1000 nm optical region of ITO thin films deposited with various target-substrate distances.

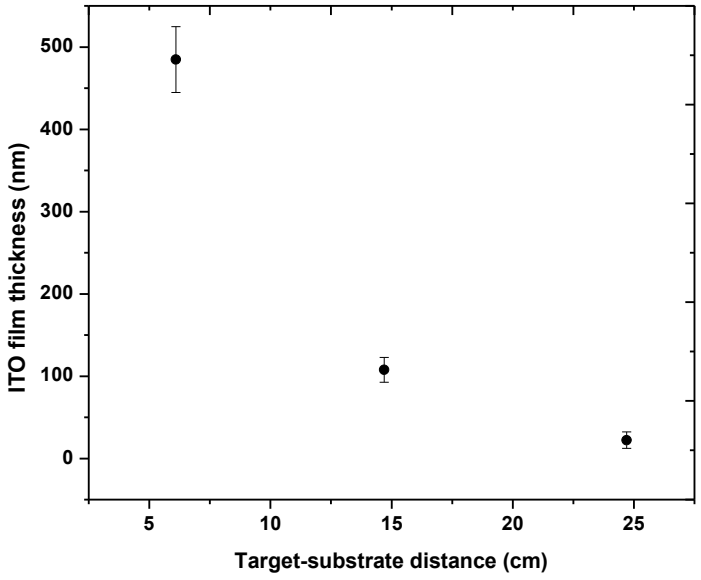

Figure 5.16. Variation of Thickness of ITO thin film as a function of target-substrate distance.

Optical energy gap for each film was calculated from the transmission data. Figure 5.17 shows the dependence of optical band gap of ITO films on the distance between sputtering target and glass substrate. Energy band gap decreased as substrate was moved away from the target. It gradually decreased from 3.71 to 3.27eV.

Figure 5.18 shows the variation of sheet resistivity of ITO thin films as a function of target-substrate distance. The number of high energy particles which arrive at the sample decreases with increasing the target –substrate distance and as result of that, film growth rate decreases and the film becomes more resistive [23]. Also that can be attributed to increase of substrate temperature during the plasma bombardment as increase of target –substrate distance [21]. The critical distance was assumed to be around 15cm.

Results for selected samples that show the effects of variation of target-substrate distance on electrical and optical properties of ITO films are surmised in Table 5.3.

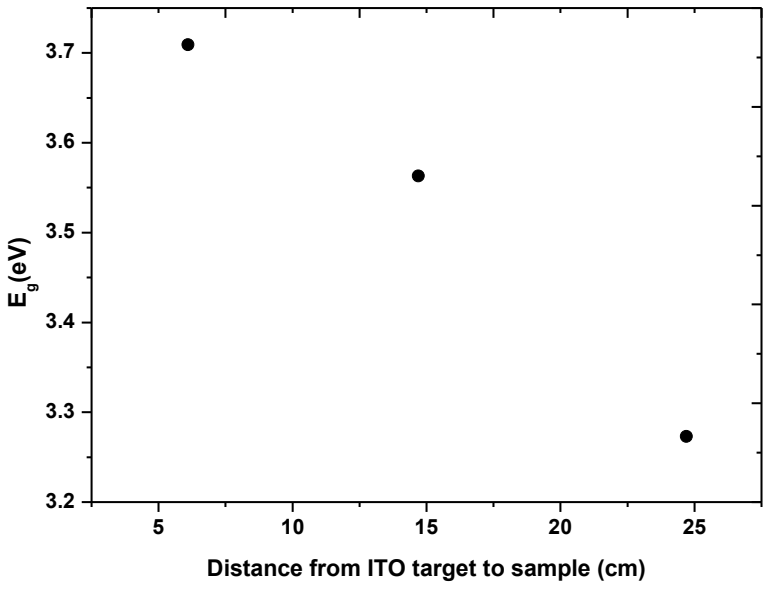

Figure 5.17. Variation of band gap of ITO thin film as a function of target-substrate distance.

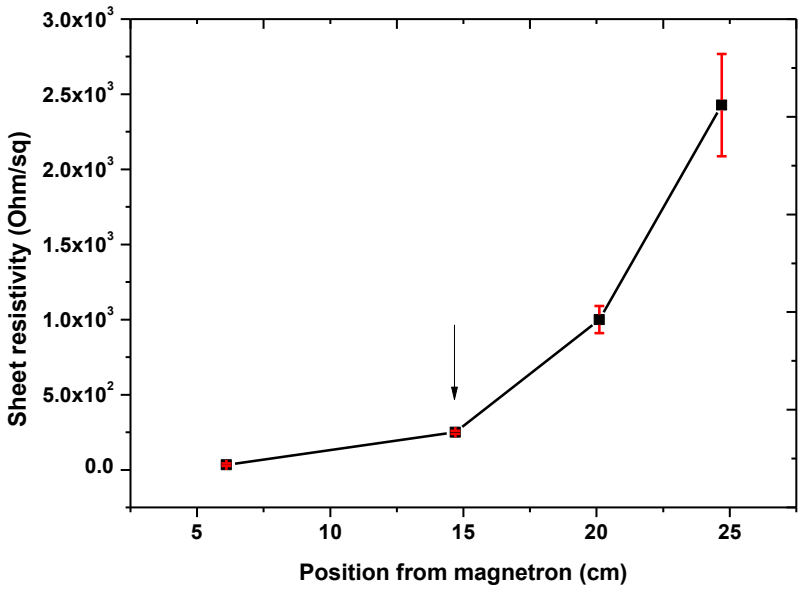

Figure 5.18. Variation of sheet resistivity of ITO thin film as a function of target-substrate distance. The black line is a guide for the eye.

Table 5.3. Effect of target-substrate distance on properties of ITO films.

Sample	Exposure Time (min)	Target-substrate distance (cm)	Plasma Power (watt)	Pressure (mB)	Film thickness (nm)	Sheet resistivity (Ω/sq)	Optical Energy (eV)
D1	20	6.1	70	$1x10^{-4}$	484.8±4.1	34.17	3.71
D2	20	14.7	70	$1x10^{-4}$	107.7±5.5	249.5	3.56
D3	20	24.7	70	$1x10^{-4}$	22.2±5.8	2427.3	3.27

5.4 Hydrogenated amorphous silicon a-Si:H layers

In amorphous silicon solar cells, it is important to characterise the optical and electrical properties of each functional layer. Single layers of intrinsic and doped amorphous silicon films have been prepared. All samples were deposited by RF plasma enhanced chemical vapour deposition at Heriot-Watt University and then each layer investigated in terms of the optical and electrical properties. Deposition parameters for intrinsic and doped silicon layers were previously studied by our group [24, 25]. Different techniques used to build and analyse the intrinsic/doped silicon films were introduced in chapter 3.

5.4.1 Experimental

Glass substrates were cleaned then transferred to the evaporator to build aluminium strips as a back contact as shown in Figure 5.19. Intrinsic and doped amorphous silicon thin films were then deposited by using plasma enhanced chemical vapour deposition technique (PECVD). Plasma was generated with 13.56 MHz RF power and substrates were heated to 200^{o}C. Deposition recipes which had been optimised by our group are shown in the Table 5.4. Once the silicon film was deposited, the sample was transferred immediately to the evaporator again to deposit top contacts as spots with diameter of about 1mm for electrical characterisation. To allow optical characterisation measurement, a silicon film was also deposited on the top of blank glass at the same time.

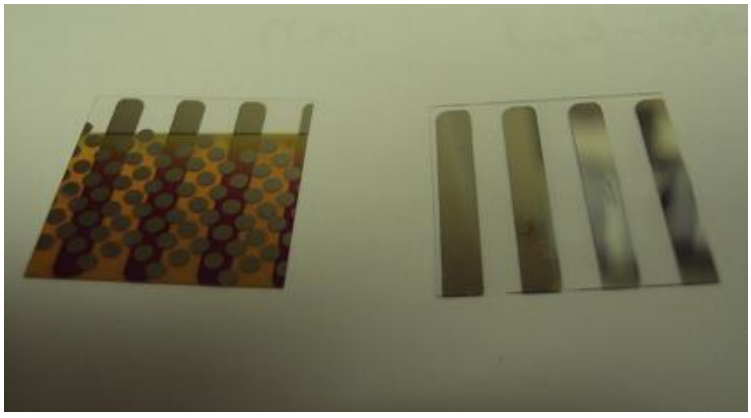

Figure 5.19. Aluminium strips and dots as back and top contacts to a thin silicon film.

Table 5.4. Recipe of a-Si:H layers. Dopant is pre mixed 1% in hydrogen.

Layer type	SiH_4 (sccm)	PH_3/H_2 (sccm)	B_2H_6/H_2 (sccm)	Plasma power(W)	Heater Temp (^0C)	Pressure (Torr)	Deposition Time(min)
Intrinsic	9.99	00	00	30	200	0.2	20
N-type	2.08	0.05	00	30	200	0.2	10
P-type	2.04	00	0.10	30	200	0.2	10

5.4.1.1 Failure behaviour

Previous studies in our group have optimised the process to deposit a good quality film of amorphous silicon using our PECVD system [24, 25]. Despite that, cracks and delamination have been seen in some samples during the earlier stage in the project. So to overcome this problem, it is important to take into account some possible causes of such failure. At the top is a mis-management of the mechanical stress in the film that can lead to cracks and even delamination of the films.

Also it is important to consider the contamination in the deposition process, which can be a substrate contamination or gaseous cross-contamination in such a single chamber PECVD system, as well as leakage contamination. As mentioned earlier in this chapter, substrates are considered as a major source of impurities in the process. So an effective cleaning procedure has to be applied to tall substrates as well as internal parts of the reactor chamber. To minimise the effects of the cross-contamination which come as a result of using a single chamber, an extra gas purging procedure between depositing doped and intrinsic layer must be applied. Finally, contamination can be caused by atmospheric gas such as oxygen and nitrogen via air leaks in PECVD setup.

To overcome these problems, it is important to make sure that cleaning of the samples is sufficient, and to revise the deposition conditions which provide the proper control of the mechanical stress and adhesion of the deposited layers.

Figure 5.20 shows a cracked film of amorphous silicon deposited on a glass substrate. We have noticed that the thicker the film the higher the possibility of failure taking place. This behaviour is well known in such highly stressed amorphous material. High

internal stress in the film network and contamination on substrates were considered as main causes of this behaviour [32, 33].

A flowchart of thin film process is presented in Figure 5.21. As example of the film optimisation process, an overview of the deposition parameters which were adjusted to improve film quality and avoid cracks and delamination, is shown in Table 5.5.

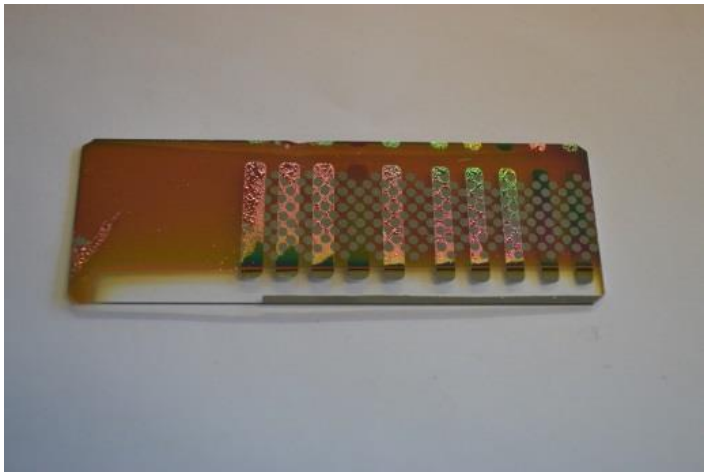

Figure 5.20. Failure behaviour of thin film a-Si:H.

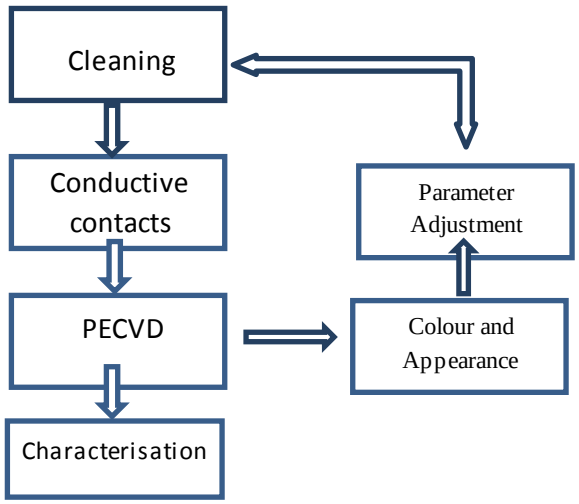

Figure 5.21. A flowchart of thin film process.

Table 5.5. Recipe adjustment for a-Si:H layers.

Sample	Date	Type	RF Power	Substrate Temp (^{o}C)	Chamber Pressure (Torr)	Dep. time min	SiH_4 sccm	PH_3/H_2 sccm	B_2H_6/H_2 sccm	Notes
2567	25/7/2011	i	30	200	0.2	20	9.58	-	-	Film looks good
2569	1/8/2011	i	30	200	0.2122	15	3.20	-	-	Film looks good (especiallyon glass)
2576	4/9/2011	n	30	200	0.5	10	2.04	-	-	It's okay on the fabric but the film peels off on the glass as well as silicon wafer
		i	30	200	0.5	20	9.99	-	-	
		p	30	200	0.5	10	2.04	-	0.098	
2577	20/9/2011	The same as 2576: good film on small glass 18x18mm with wide Al strips and on the fabric but it doesn't stick on silicon and microscope glass.								
2578	21/9/2011	n	30	200	0.5	10	2.04	0.05	-	(New heater). It's okay on the fabric but the film peels off on the glass as well as silicon wafer
		i	30	200	0.5	20	9.99	0.00	-	
		p	30	200	0.5	10	2.1	-	0.098	
2579	22/9/2011	i	30	200	0.5	20	9.99	-	-	The film flaked off
2580	23/9/2011	i	30	200	0.5	20	9.99	-	-	30 watt Ar plasma treatment for 10 min. **Slow** delamination
2581	27/9/2011	n	20	200	0.5	10	2.04	0.05	-	It's okay on the fabric but the film peels off the glass as well as silicon wafer **Fast**
		i	20	200	0.5	20	9.99	-	-	
		p	20	200	0.5	10	2.1	-	0.098	
2582	12/10/2011	i	30	200	0.5	20	10	-	-	Flaked off stronglywhen removed from chamber but fabric was ok
2583	13/10/2011	i	30	200	0.5	20	10	-	-	Flaked off even when extra cleaning for big glass
2584	18/10/2011	i	30	200	0.2	15	3.2	-	-	Film looks good
2585	19/10/2011	i	30	200	0.2	15	9.8	-	-	Not bad. some delamination
2586	20/10/2011	i	30	200	0.1	15	9.8	-	--	peels off **Fast**

5.4.2 Results

5.4.2.1 Thickness measurement and Optical characterisation

5.4.2.1.1 Intrinsic film

A Variable Angle Spectroscopic Ellipsometer (J. A. Woolam) with a spectral range of 300–1500 nm was used to extract ellipsometric parameters Ψ and Δ which can be used to measure thickness and optical properties of the intrinsic amorphous silicon films. Each sample was measured at three angles of incidence (65°, 70°, 75°), then data acquisition and analysis was performed using WVASE32 software. In order to determine layer thickness and optical constants from the measured data, a suitable optical model has to be applied. The Tauc-Lorentz model is particularly suited for the analysis of amorphous semiconductors [26-28]. Figure 5.22 shows schematic representation of a layered optical model with single intrinsic layer of a-Si:H for a selected sample. By applying this model with measured Ψ and Δ, theoretical values of Ψ and Δ can be obtained as shown in Figures 5.23 and 5.24. The model adjusted to minimise MSE (mean square error) between measured and theoretical data. Then from these data, optical constants and thickness of the film can be derived.

3 srough	2.239 nm
2 SimpleGradedEMA (GenOsc)	201.382 nm
1 GenOsc	0.000 nm
0 bk7	1 mm

Figure 5.22. Schematic representation of a layered optical model with single i-layer of a-Si:H.

The model consists of a set of thin films on a glass substrate. Each layer has its optical properties which should be physically acceptable. As a result for an intrinsic a-Si:H layer, film thickness was found to be around 201.4±0.6 nm. A simple effective medium approximation (EMA) layer of 2.7% voids has been added to the model. Finally a thin rough interface was added at the top of the model structure with thickness of 2.2 nm which improved the result.

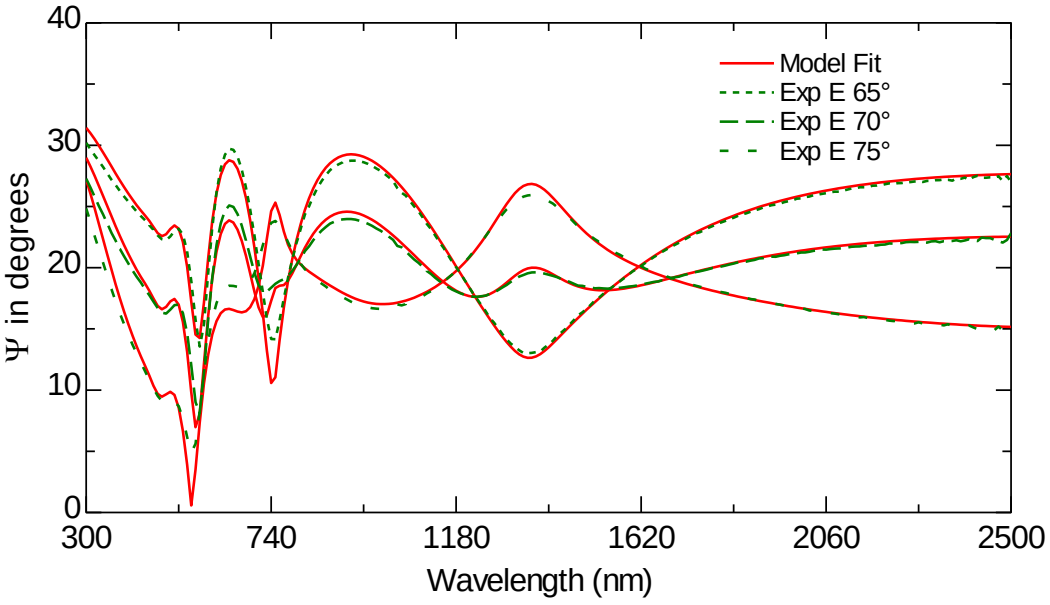

Figure 5.23. Ψ of intrinsic a-Si:H thin film on glass substrate measured from 300 to 2500nm.

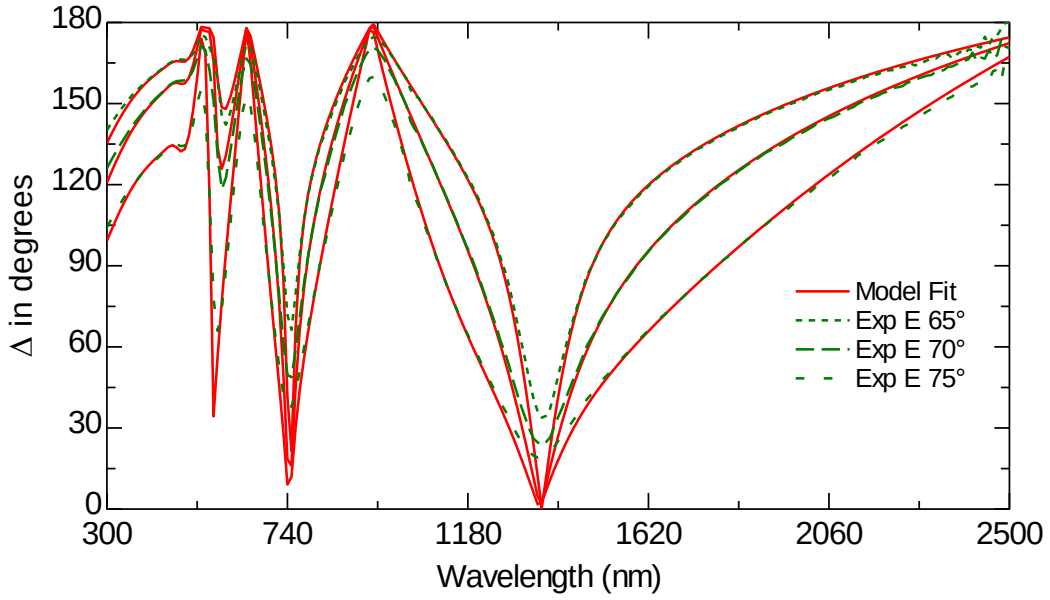

Figure 5.24. Δ of intrinsic a-Si:H thin film on glass substrate measured from 300 to 2500nm.

As a result of including a graded EMA layer in the model, the best fit optical constants at the top and bottom of the intrinsic film are shown in Figure 5.25. From to the direct relation between k and the absorption coefficient, strong absorption can be seen starting around 750nm, peaking at around 300nm and the Urbach region accounts for a very small absorption above 750nm.

Furthermore, the index of refraction is slightly lower at the bottom of the film and can be seen in the depth profile of optical constants where the variation in n and k is very

small across the film as shown in Figure 5.26. This can be attributed to decreased film roughness with increasing of thickness. That is known as a smoothing mechanism [29].

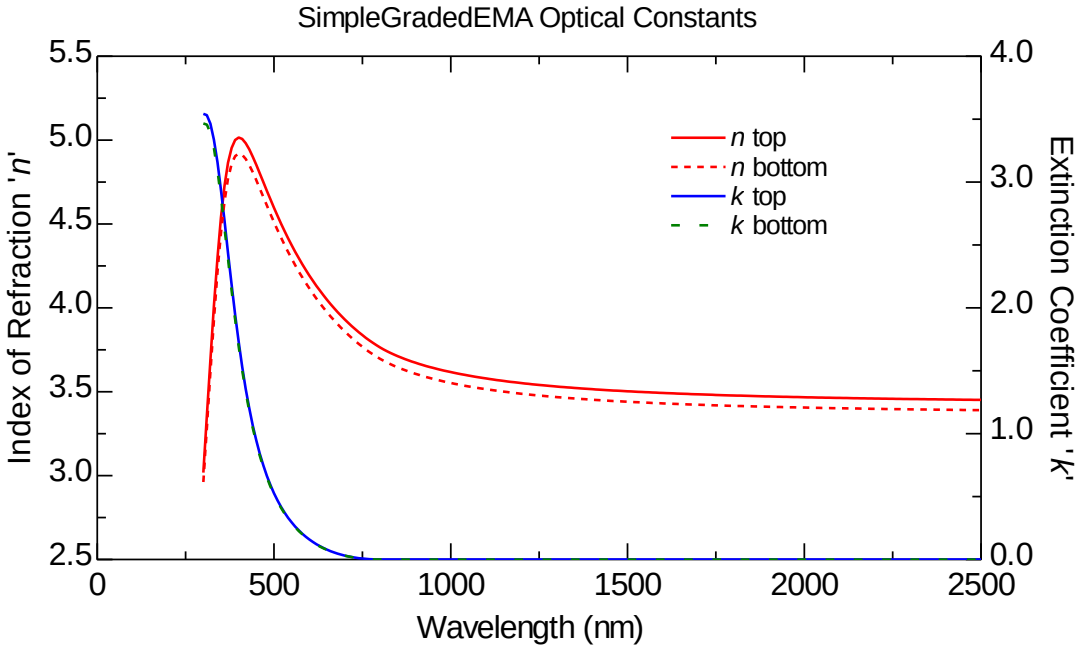

Figure 5.25. Optical constants of intrinsic layer.

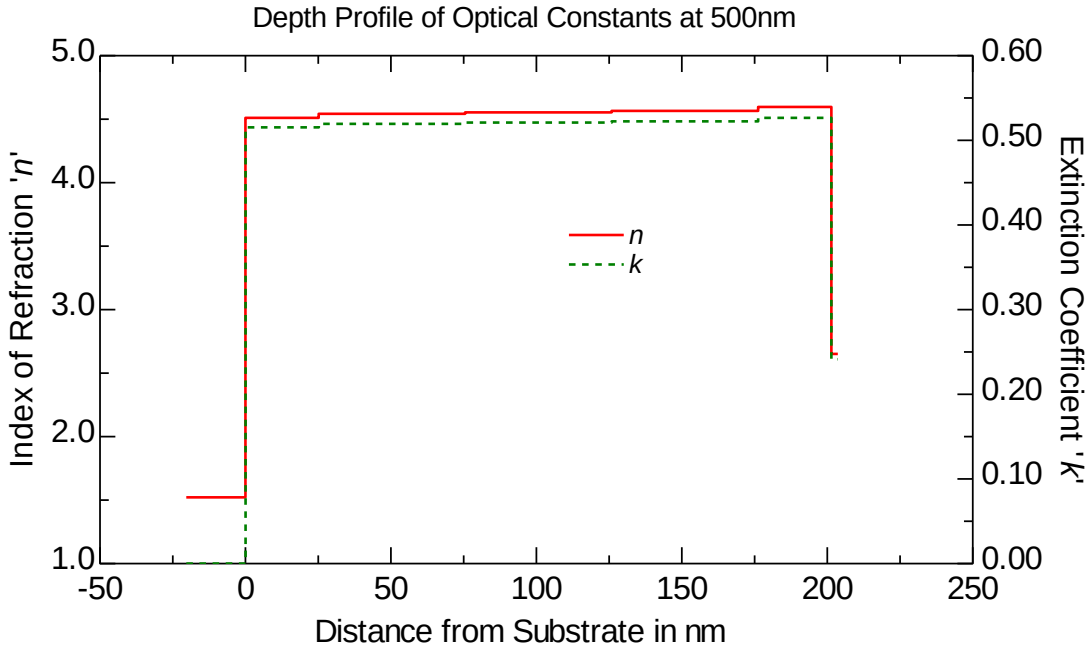

Figure 5.26. Depth profile of optical constants of intrinsic layer.

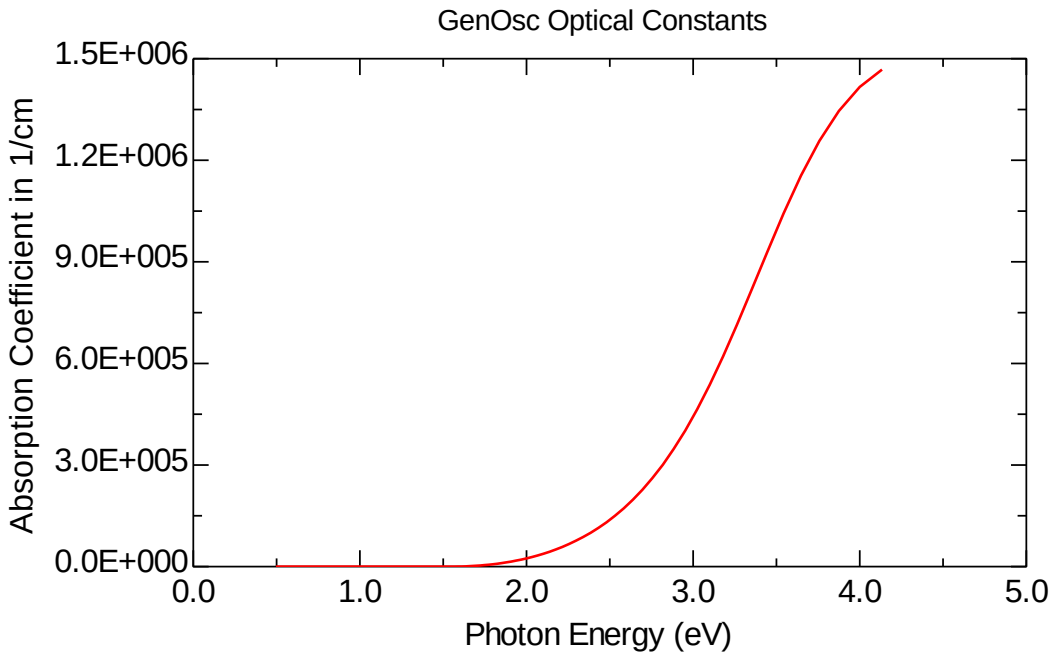

Figure 5.27. Absorption coefficient vs photon energy generated from the model.

Figure 5.27 shows the absorption coefficient of the intrinsic film as generated from the model. The data obtained by using Perkin UV/VIS spectrometer is shown in Figure 5.28, where the effect of Urbach energy (E_u) can be seen as sub gap absorption beyond the optical band gap threshold (E_g). The transition near the band gap is controlled by the transition from extended to extended states and it can be described by the Tauc equation.

The optical band gap is determined by a plot of $(\alpha h\upsilon)^{1/2}$ versus $(h\upsilon)$, which is Tauc's plot as shown in Figure 5.29. It is clear that the plot is linear over a wide range of photon energies indicating the direct type of transitions and the plot gives a straight line with intercept equal to the optical band gap. For intrinsic layers, optical band gap was found to be 1.733eV.

In amorphous semiconductors such a-Si:H the Urbach energy varies from 30 to 100 meV. In our case, for the intrinsic layer it is 101meV which corresponds to a high level of disorder within the semiconductor material.

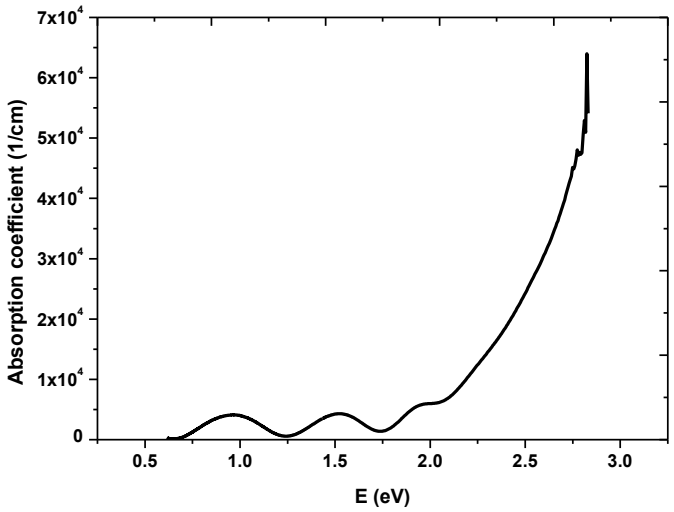

Figure 5.28. Absorption coefficient vs photon energy obtained from UV/VIS spectrometer.

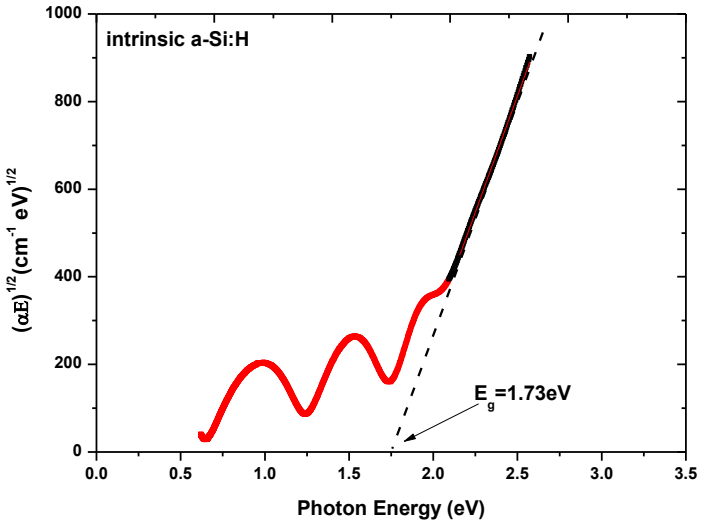

Figure 5.29. Variation of $(\alpha h\upsilon)^{1/2}$ versus photon energy ($h\upsilon$), Tauc's plot, of i-a-Si:H thin film.

5.4.2.1.2 Doped films

The same TL model (graded Tauc-Lorentz) was applied on measured ellipsometric data for phosphine and boron doped amorphous silicon films (n and p-type). Figure 5.30 shows a schematic representation of a layered optical model with a single n-type layer (left) and p-type (right) for typical samples. During the fitting trials, it can be seen that there is a strong relation between the roughness of the film and the thickness.

At the beginning of film deposition, interaction between neighbouring nuclei occurs and smoothing results from the mass transport into the surface [29,30].

3	srough	3.190 nm	3	srough	5.650 nm
2	SimpleGradedEMA (GenOsc)	66.563 nm	2	SimpleGradedEMA (GenOsc)	56.921 nm
1	GenOsc	0.000 nm	1	GenOsc	0.000 nm
0	bk7	1 mm	0	bk7	1 mm

Figure 5.30. Schematic representation of a layered optical model with single n-type (left) and p-type (Right) of a-Si:H film.

Figures 5.31 and 5.32 show the variation in n and k between top and bottom for n-type and p-type amorphous silicon films respectively. Refractive index grading allowed n and k to vary two steps from the bottom to the top of both n and p-type films. That can be seen in depth profile of the optical constants as shown in Figures 5.33 and 5.34 which were obtained from the TL model.

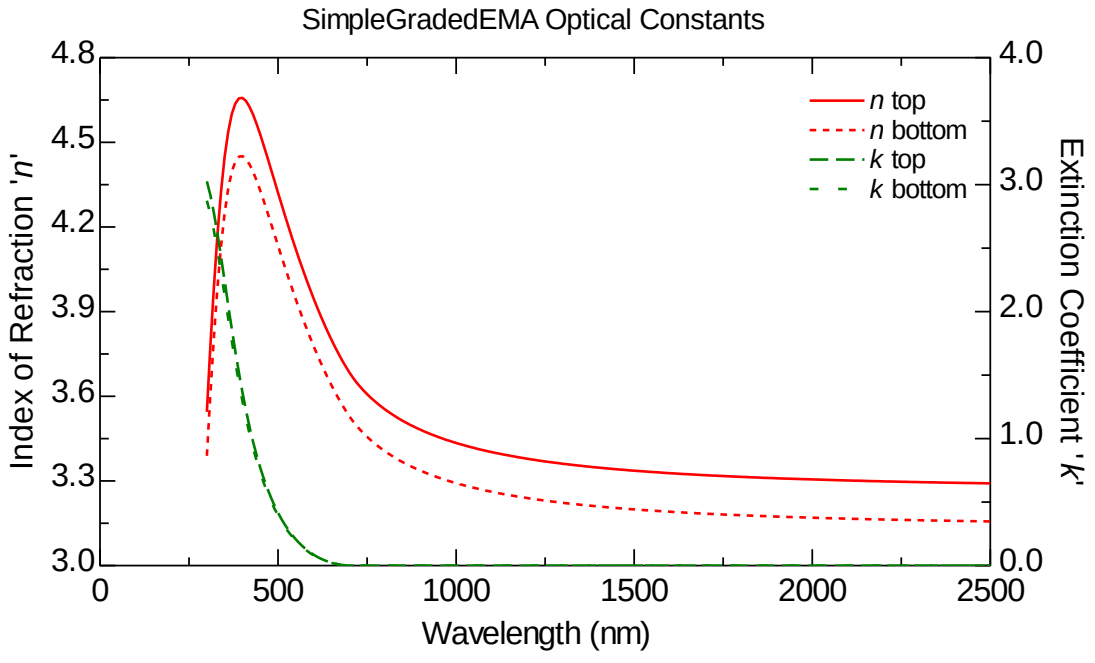

Figure 5.31. Optical constants of n-type layer.

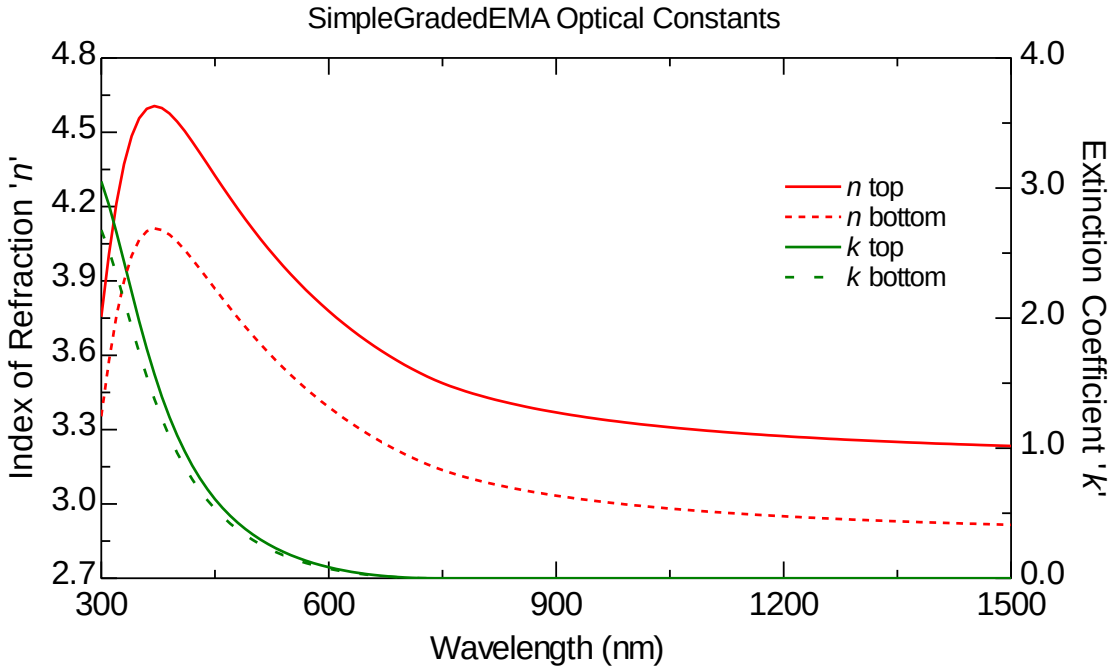

Figure 5.32. Optical constants of n-type layer.

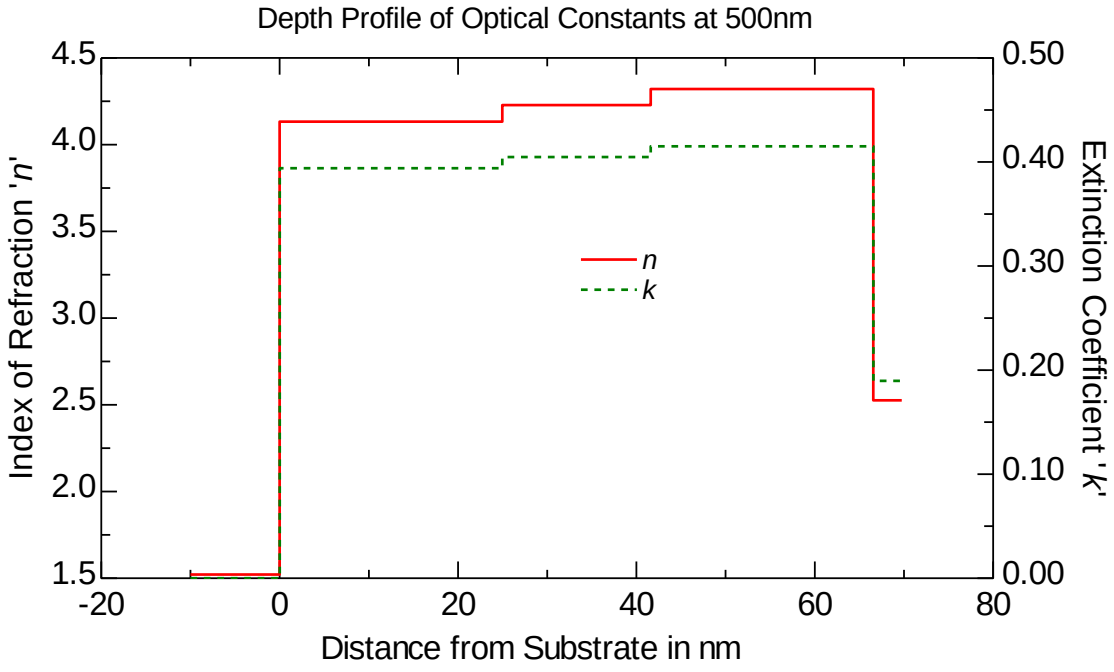

Figure 5.33. Depth profile of optical constants of n-type layer.

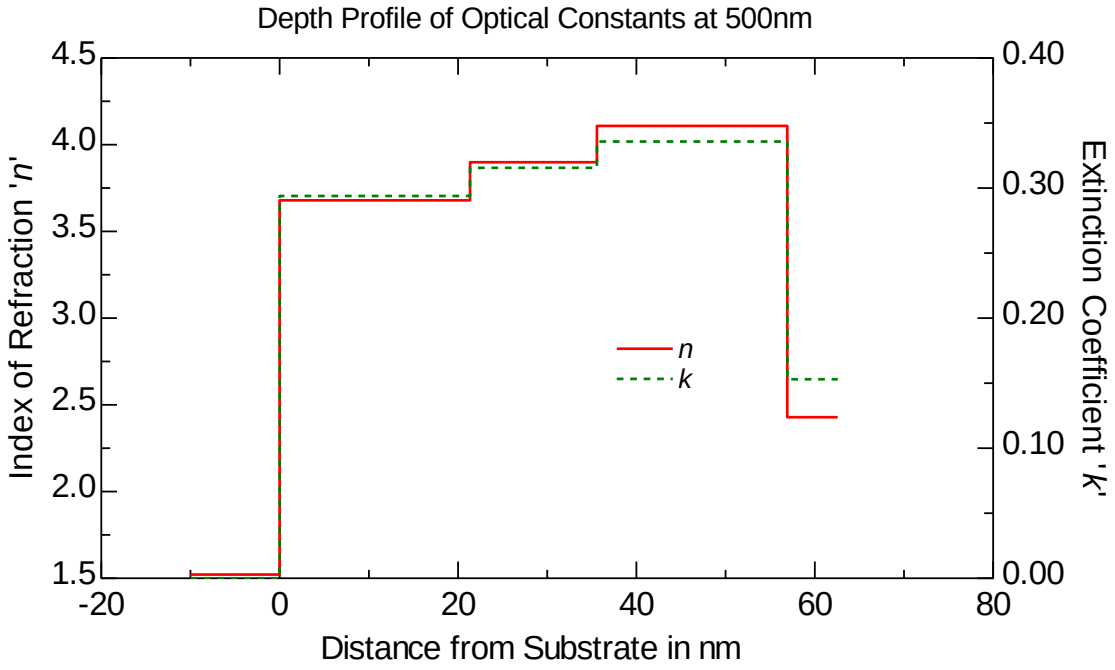

Figure 5.34. Depth profile of optical constants of p-type layer.

The optical band gap is determined by a plot of $(\alpha h\upsilon)^{1/2}$ versus $(h\upsilon)$ for each layer as shown in Figures 5.35 and 5.36. Optical band gaps were found to be 1.8304eV and 1.703eV for n-type and p-type amorphous silicon respectively. By considering the absorption coefficient at the photon energy just below the optical gap, Urbach energies were found to be 73 meV for n-type and 55meV for p-type amorphous silicon layers.

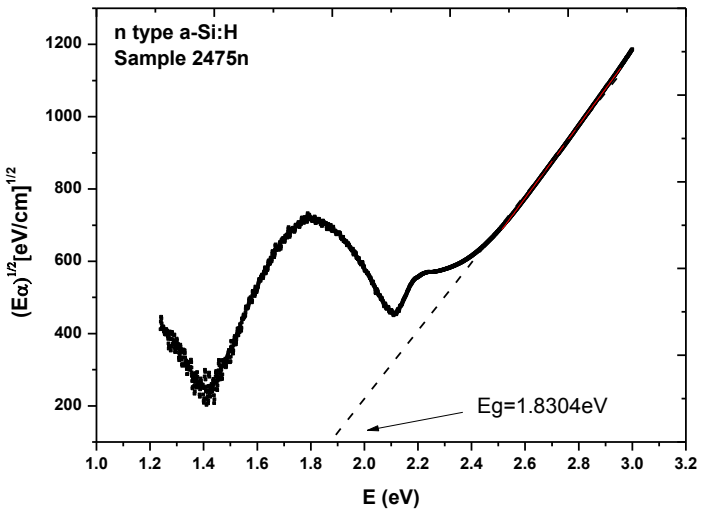

Figure 5.35. Variation of $(\alpha h\upsilon)^{1/2}$ versus photon energy($h\upsilon$), Tauc's plot, of n-type a-Si:H thin films.

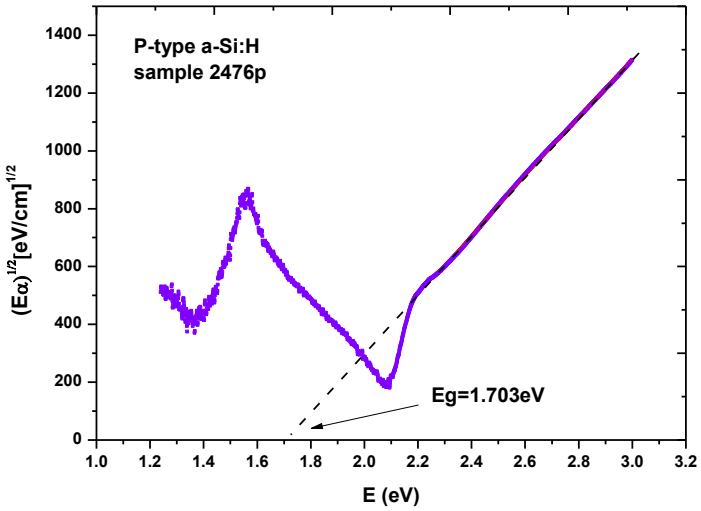

Figure 5.36. Variation of $(\alpha h\upsilon)^{1/2}$ versus photon energy($h\upsilon$), Tauc's plot, of p-type a-Si:H thin films.

5.4.2.2 Electrical characterisation

5.4.2.2.1 I-V characterization

A single layer of amorphous silicon was deposited on an aluminium coated glass substrate and then aluminium dots with a diameter of 1 mm were evaporated on top of the configuration as shown in Figure 5.37. A *J-V* plot for single intrinsic and doped layers is plotted in Figure5.38, 5.39 and 5.40. As can be seen the forward bias response is non-linear probably indicating diode behaviour. This is possibly due to a Schottky barrier between the silicon and aluminium contact.

By fitting a linear plot to the *J-V* curves at the high bias end of the data, the resistivities of the layers were measured using equation (3-3). The resistance of a typical intrinsic layer was measured to be 101.2KΩ and the resistivity was found to be $1.56\text{x}10^{6}$ Ω-m. For n- and p-layers, resistances were measured to be 6.7KΩ and 73.1KΩ respectively. The resistivity of n-type silicon was calculated to be $3.16\text{x}10^{5}$ Ω-m, and $41.80\text{x}10^{5}$ Ω-m for p-type. We can see that the resistivities are of similar order, suggesting that n-and p-layers are insufficiently doped (compare with Figure 2.11).

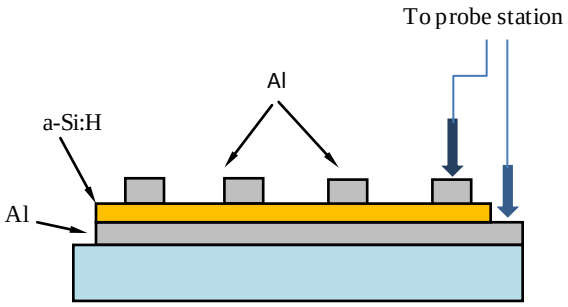

Figure 5.37. Cross-section for Al/a-Si:H/Al configuration used in dark conductivity measurements.

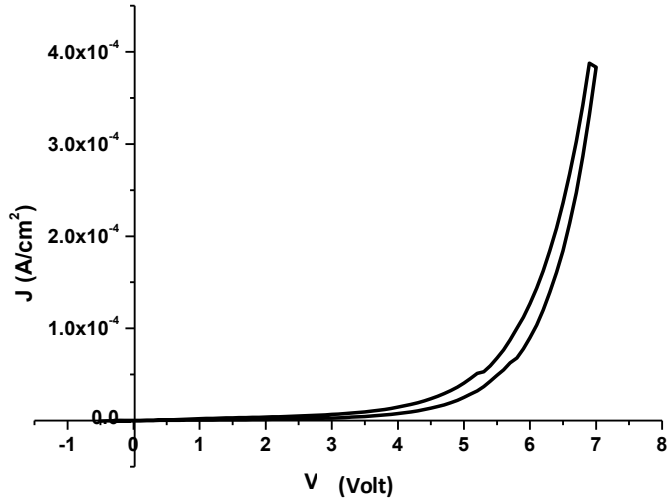

Figure 5.38. A typical J-V characteristic curve of intrinsic thin film silicon.

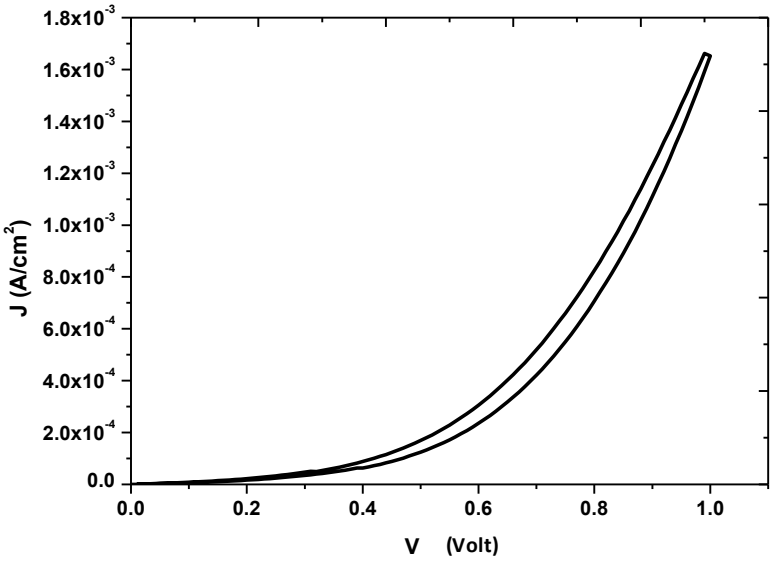

Figure 5.39. A typical J-V characteristic curve for thin film silicon doped with phosphorus (n-type).

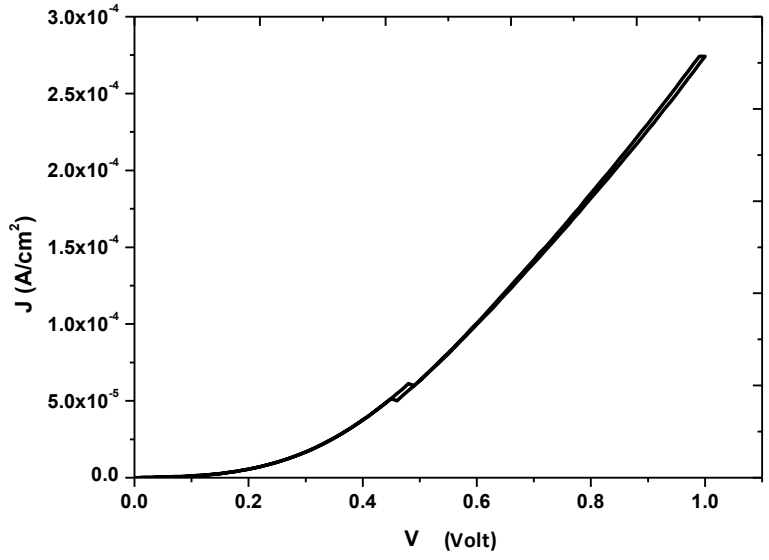

Figure 5.40. A typical J-V characteristic curve for thin film silicon doped with boron (p-type).

5.4.2.2.2 Temperature dependence of the dark conductivity

Dark conductivity as a function of temperature was measured for intrinsic as well as doped amorphous silicon deposited with configuration of Al/a-Si:H/Al (see Figure 5.37). Samples were heated during the test and *I-V* data were collected as function of temperature which started from room temperature to 100°C in increments of 5°C. Figure 5.41 shows the effects of the temperature on a typical sample *I-V* behaviour. The relation between (*1/T*) and ($ln\sigma$) is plotted in Figure 5.42 to obtain the activation energy E_a. It is found that the activation energy for intrinsic layer is about 0.41eV and for n- and p-type 0.18eV and 0.32eV respectively. The activation energy of intrinsic layer is smaller than expected implying defect energy levels within band gap.

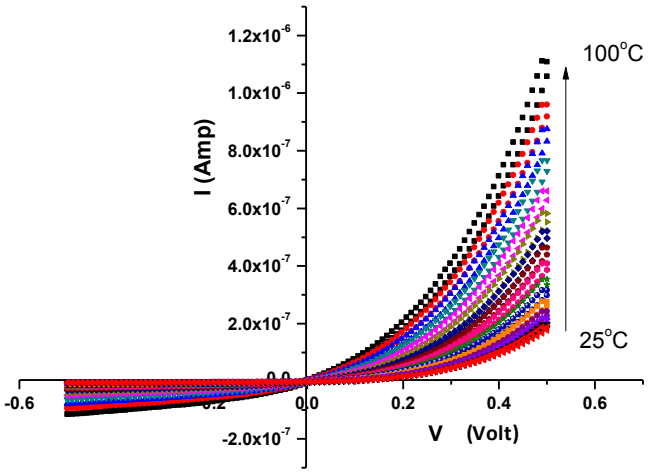

Figure 5.41. Temperature dependence of the dark conductivity.

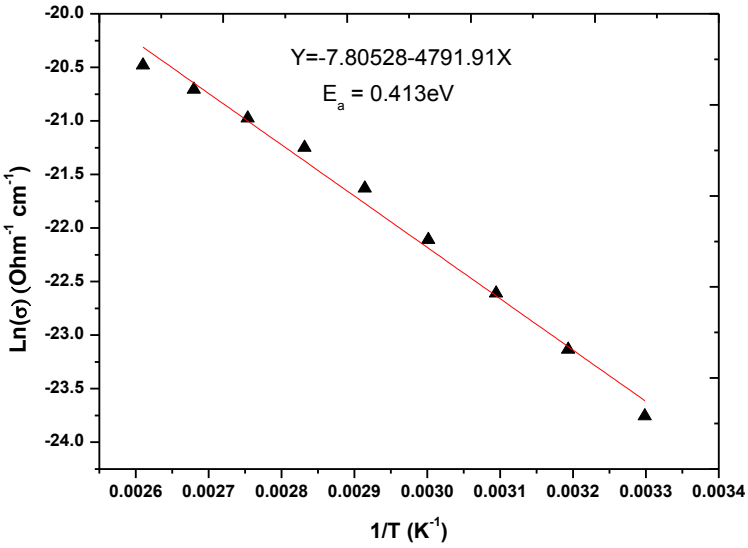

Figure 5.42. Temperature dependence of dark conductivity for intrinsic layer of a-Si:H.

5.4.2.3 Raman spectroscopy

Thin films of intrinsic amorphous silicon were deposited on top of glass substrates in order to study the crystallinity. Raman spectroscopy is a non-destructive technique used for monitoring the structure of amorphous silicon films. A Renishaw inVia spectrometer was used to analyse the samples with 514nm laser wavelength and power varied from 5% to 100% with magnification of 50x.

Figure 5.43 shows the influence of laser power on the Raman shifts of intrinsic a-Si:H on a glass substrate. The peak centre position shifts towards lower wavenumber with an increase in laser power. The increase of the laser power seems to have a significant influence on the Raman measurements. It was reported that the peak shifts are almost reversible and therefore not caused principally by permanent structural change [31]. It appears that this film showed typical amorphous structure.

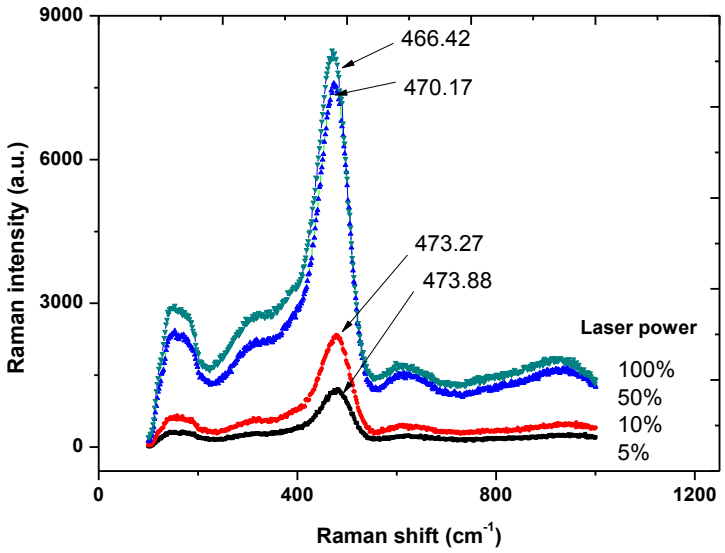

Figure 5.43. The influence of laser power on the Raman shifts of intrinsic a-Si:H.

5.5 Conclusion

To conclude, conductive contacts on glass substrates as well as single layers of a-Si:H have been successfully fabricated and characterised in terms of their optical and electrical properties. Aluminium contacts and indium tin oxide films were deposit on glass substrates in order to investigate changes in layer deposition conditions to potentially improve layer quality and optimise the process. Then intrinsic and doped layers of amorphous silicon were fabricated and subjected to optical and electrical tests to provide more information about their durability and functionality. Then finally thin film deposition parameters were adjusted to overcome the failure behaviour in the film. So we can move toward combining these films to construct a functional configuration of solar cells either on glass or flexible substrates. That is the target of the next chapter where we will use the information related with single layers to build and test the functionality of the cells.

5.6 References

1. Kay, J., Jr, *Substrate cleaning methods for thin film deposition*. 1959, San Diego: General Dynamics.

2. Oliva A I, A. F, and Ceh O, *Physical properties of AU and AL thin films measured by resistive heating*. Surface Review and Letters, 2005. 12(1): p. 101- 106,.

3. Chuang, M., *ITO Films Prepared by Long-throw Magnetron Sputtering without Oxygen Partial Pressure*. Journal of Materials Science & Technology, 2010. 26(7): p. 577-583.

4. Tuna, O., et al., *High quality ITO thin films grown by dc and RF sputtering without oxygen* J. Phys. D: Appl. Phys, 2010. 43: p. 7.

5. J.A. Woollam Company, I., *Guide to using WVASE32*. 1994-2010, J.A. Woollam Co., Inc: Lincoln, NE,68508.

6. Synowicki, R.A., *Spectroscopic ellipsometry characterization of indium tin oxide film microstructure and optical constants. Thin Solid Films*, 1998. 313–314(0): p. 394-397.

7. Kim, H., et al., *Electrical, optical, and structural properties of indium-tin-oxide thin films for organic light-emitting devices*. Journal of Applied Physics, 1999. 86(11): p. 6451-6461.

8. Kim, H., et al., *Effect of film thickness on the properties of indium tin oxide thin films*. Journal of Applied Physics, 2000. 88(10): p. 6021-6025.

9. Ali, H.M., H.A. Mohamed, and S.H. Mohamed, *Enhancement of the optical and electrical properties of ITO thin films deposited by electron beam evaporation technique*. The European Physical Journal - Applied Physics, 2005. 31(02): p. 87-93.

10. S. H. Mohamed , F.M.E.-H., G. A. Gamal and M. M. Kahlid, *Properties of Indium Tin Oxide thin films deposited on polymer substrates*. Acta Phys. Polonica A, 2009. 115(3).

11. Kim, K.J. and Y.R. Park, *Large and abrupt optical band gap variation in In-doped ZnO*. Applied Physics Letters, 2001. 78(4): p. 475-477.

12. Weijtens, C.H.L. and P.A.C. Van Loon, *Influence of annealing on the optical properties of indium tin oxide*. Thin Solid Films, 1991. 196(1): p. 1-10.

13. Han, H., J.W. Mayer, and T.L. Alford, *Band gap shift in the indium-tin-oxide films on polyethylene napthalate after thermal annealing in air*. Journal of Applied Physics, 2006. 100(8): p. 083715.

14. Hao, L., et al., *Thickness dependence of structural, electrical and optical properties of indium tin oxide (ITO) films deposited on PET substrates*. Applied Surface Science, 2008. 254(11): p. 3504-3508.
15. Deng, W., et al., *Development of conductive transparent indium tin oxide (ITO) thin films deposited by direct current (DC) magnetron sputtering for photon-STM applications*. Applied Physics A, 2001. 72(5): p. 595-601.
16. Benoy, M.D., et al., *Thickness dependence of the properties of indium tin oxide (ITO) FILMS prepared by activated reactive evaporation*. Brazilian Journal of Physics, 2009. 39: p. 629-632.
17. Liu, F.S., et al., *Visible and infrared emissions from c-axis oriented AlN:Er films grown by magnetron sputtering*. Journal of Applied Physics, 2006. 99(5): p. 053515.
18. Chao, Y., W. Tang, and X. Wang, *Properties of Resistivity, Reflection and Absorption Related to Structure of ITO Films*. Journal of Materials Science & Technology, 2012. 28(4): p. 325-328.
19. Burstein, E., Anomalous Optical Absorption Limit in InSb. Physical Review, 1954. 93(3): p. 632-633.
20. Martínez, M.A., J. Herrero, and M.T. Gutiérrez, *Optimisation of indium tin oxide thin films for photovoltaic applications*. Thin Solid Films, 1995. 269(1–2): p. 80-84.
21. Kumar, C.V.R.V. and A. Mansingh, *Effect of target-substrate distance on the growth and properties of rf-sputtered indium tin oxide films*. Journal of Applied Physics, 1989. 65(3): p. 1270-1280.
22. Suzuki, A., et al., *Highly conducting transparent indium tin oxide films prepared by pulsed laser deposition*. Thin Solid Films, 2002. 411(1): p. 23-27.
23. Meng CHEN, X.B., Jun GONG, Chao SUN, Rongfang HUANG, Lishi WEN, *Properties of reactive magnetron sputtered ITO films without in-situ substrate heating and post-deposition annealing*. J. Mater. Sci. Technol., 2000. 16(03): p. 281-285.
24. Jardine, S., *Thin Film Silicon on Textiles by Microwave Plasma Chemical Vapour Deposition*. PhD thesis, Heriot-Watt University, Edinburgh, 2006.
25. Lind, A.H.N., *Deposition and Characterisation of Silicon and Conductive Layers on Woven Polyester*, PhD thesis, Heriot-Watt University, Edinburgh, 2013.
26. G. E. Jellison, J. and F.A. Modine, *Parameterization of the optical functions of amorphous materials in the interband region*. Applied Physics Letters, 1996. 69(3): p. 371-373.

27. Sánchez, P., et al., *Characterization of Doped Amorphous Silicon Thin Films through the Investigation of Dopant Elements by Glow Discharge Spectrometry: A Correlation of Conductivity and Bandgap Energy Measurements*. International Journal of Molecular Sciences, 2011. 12(4): p. 2200-2215.

28. Amans, D., et al., E*llipsometric study of silicon nanocrystal optical constants*. Journal of Applied Physics, 2003. 93(7): p. 4173-4179.

29. Wank, M.A., R.A.C.M.M.v. Swaaij, and M.C.M.v.d. Sanden, *On the surface roughness development of hydrogenated amorphous silicon deposited at low growth rates*. Applied Physics Letters, 2009. 95(2): p. 021503.

30. Collins, R.W., et al., *Evolution of microstructure and phase in amorphous, protocrystalline, and microcrystalline silicon studied by real time spectroscopic ellipsometry*. Solar Energy Materials and Solar Cells, 2003. 78(1–4): p. 143-180.

31. Lind, H., Wilson J.I.B, and Mather R. *Raman spectroscopy of thin-film silicon on woven polyester*. physica status solidi (a), 2011. 208(12): p. 2765-2771.

Chapter 6. Functional solar cells

6.1 Introduction

As discussed in previous chapters one challenge was to prepare a polyester fabric substrate so it can be rendered electrically conducting. A second challenge is to apply the n-i-p silicon configuration directly on the conductive polyester fabrics [1, 2]. In this chapter, n-i-p single junctions to a-Si:H were fabricated onto different types of substrates such as glass, polyester fabric and polytetrafluoroethylene fabric (PTFE).

In the first part of this chapter, the solar cell configuration was built on glass substrate so the functional properties could serve as reference. Then the same configuration was introduced onto woven PTFE and polyester fabric substrates. With this approach, the effects of surface roughness on the functionality of the cells can be observed. An additional layer of ITO, Cr or Ti was used as diffusion barrier between the aluminium back contact and n-type a-Si:H layer.

Diffusion barrier with Al back contact has been suggested to improve the efficiency of amorphous silicon cells [3,4].

6.2 Experimental details

Amorphous silicon solar cells were made on different types of substrates. Glass, polyester and PTFE fabric were used as substrates for depositing single (n-i-p) amorphous silicon solar cells. In the first section, the first aim was to assess the influence of the diffusion barrier on the electrical performances of the solar cell devices. In order to study the influence of the thickness of aluminium back contacts on the electrical performance of the device, a set of glass substrates was coated with different thicknesses of aluminium contacts with and without introducing ITO, Cr and Ti as a diffusion barrier. Finally, three types of substrates; Glass, PTFE, and polyester fabrics are used as a base for amorphous silicon solar cells. The target was to examine the effects of the roughness and flexibility of the substrate on the performance of the cell.

6.2.1 Substrate Material

Amorphous silicon solar cells will be fabricated on different types of flexible substrates which act as a holder and provide a mechanical. Amorphous silicon solar cells are made in an RF PECVD vacuum system which required samples to be heated to about 200^{o}C. Thus, the substrate material should be selected carefully to survive such temperature. Glass slides with dimension of 2.5 cm x 7.5 cm were used as a reference substrate in both superstrate and substrate configuration. Thin film silicon can be deposited on polyester fabric by microwave PECVD which enables nc-Si formation [1, 2]. Conductive contacts were fabricated onto polyester fabric as described in detail in chapter 4. The surface topography of the polyester fabric was inspected using Leica DM6000M optical microscope as shown in Figure 6.1. Height variations of up to 100 µm were found. More textured surface and less roughness was found when the PTFE sample was analysed and the variation found to be around 70 µm as shown in Figure 6.2.

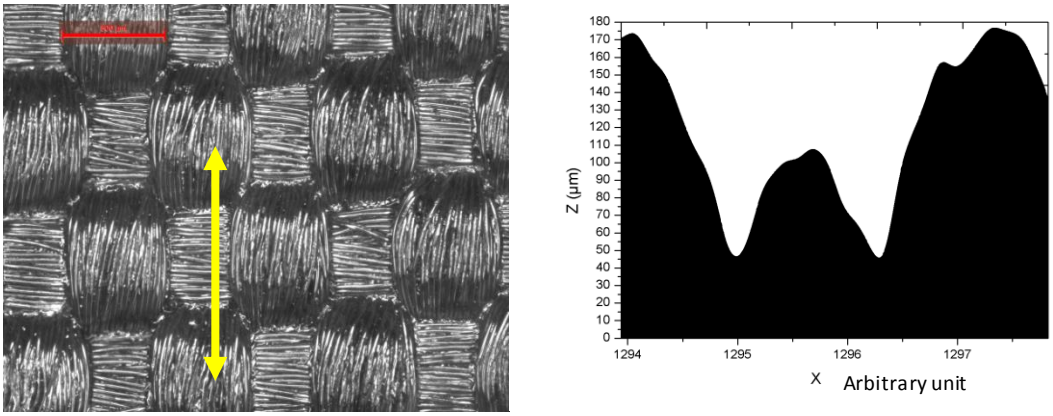

Figure 6.1. Left: polyester coated fabric, Right: Height versus position along the line indicated in left picture (roughness profile).

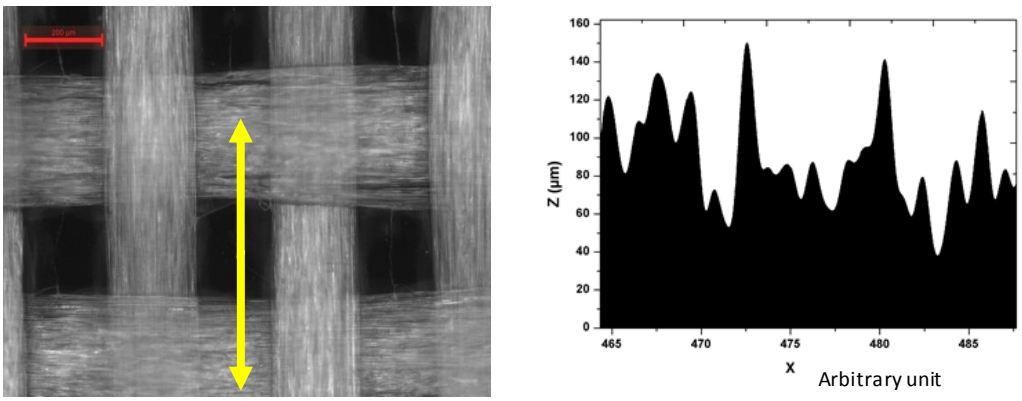

Figure 6.2. Left: PTFE coated fabric, Right: Height versus position along the line indicated in left picture (roughness profile).

6.2.2 Solar cell configurations

The PECVD technique has the versatility to deposit hydrogenated silicon on a variety of substrates such as glass, plastic, and silicon wafers etc. Also this technique is capable to build amorphous silicon with two different configurations; n-i-p and p-i-n. The thin film solar cells can be developed in two structures, known as superstrate and substrate. In superstrate configuration, the light enters through the substrate which should be transparent whereas in substrate configuration light passes through the opposite side as shown in Figure 6.3. Both types of cell configuration were used in this work.

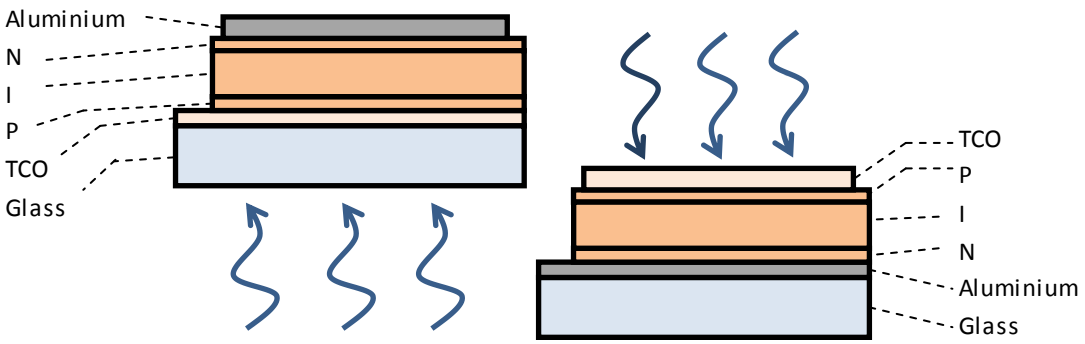

Figure 6.3. Superstrate configuration (Left) and substrate configuration (Right).

6.2.3 Deposition parameters

Table 6.1 shows deposition parameters for n-i-p amorphous silicon solar cell layers.

Table 6. 1. An n-i-p amorphous silicon cell deposition recipe.

Layer type	SiH_4 (sccm)	PH_3/H_2 (sccm)	B_2H_6/H_2 (sccm)	Plasma power (W)	Heater Temp (^0C)	Pressure (Torr)	Deposition Time(min)
N-type	2.08	0.05	00	30	200	0.2	10
Intrinsic	10.00	00	00	30	200	0.2	20
P-type	2.04	00	0.10	30	200	0.2	10

Note: Dopant is pre mixed 1% in hydrogen.

All the samples in this work have been given a unique serial number which refers to the actual PECVD deposition run. Using such a numbering scheme facilitates access to the information related to each sample and helps to distinguish between cells. Deposition parameters for each run were recorded in a form (see Appendix D).

6.3 Results and Discussion

6.3.1 Single junction a-Si:H solar cells on glass substrate

Both the substrate (n-i-p) and superstrate (p-i-n) configurations were deposited on glass substrates. First, we investigated the effect of a diffusion barrier on the a-Si:H solar cells' performance with three available materials used as barrier (ITO, Cr, Ti). Then the effect of the aluminium contact thickness with and without barrier was subjected to investigations. Finally, cells were examined in terms of the influence of diffusion barrier thickness. The current voltage characteristics of all cells were measured under illumination with a solar simulator (ABET sun 2000s) in standard test conditions (25°C, AM1.5 spectrum, 100mW/cm^2). Figure 6.4 shows actual single junction amorphous silicon solar cells on glass substrate each with area of 0.25cm^2.

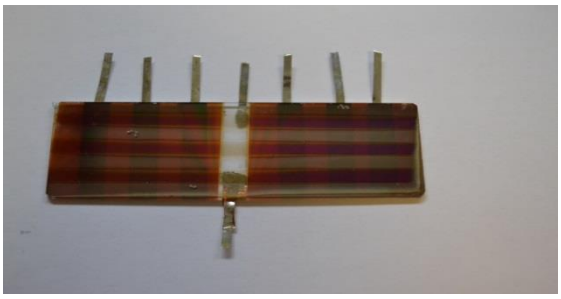

Figure 6.4. Single junction a-Si:H solar cells on glass.

6.3.1.1 Influence of the diffusion barrier on the electrical performance

Material as a diffusion barrier layer must be conductive, transparent and thermally stable [3,4]. Tin doped indium oxide (In_2O_3:Sn), Chromium (Cr) and Titanium (Ti) were deposited by Edwards Auto 306 RF-Sputter Coater (see 3.2.1.2) and used as the diffusion barrier layers between the aluminium back contacts and n-type a-Si:H for amorphous silicon solar cells on glass substrates.

6.3.1.2 Solar cells with and without diffusion barrier

Sputtered titanium (Ti) with thickness of 20nm was used as the diffusion barrier for the cell structure of *Glass/Al/Ti/n-i-p/ITO*. The solar cell efficiency was around 0.14% with short circuit current 0.22mA, open circuit voltage 0.843 V, and very low FF as shown in Figure 6.5. The maximum EQE peak was 15% as shown in Figure 6.6.

Figure 6.7 shows the poor light I-V characteristics of all studied cells with Cr diffusion barriers. The cell structure of *Glass/Al/Cr/n-i-p/ITO* has poor performance with η=0.004%%, FF = 19.5%, V_{oc} = 0.314 V and I_{sc} = 0.022 mA. Maximum EQE peak was 8% as shown in Figure 6.8. This poor cell efficiency may be due to diffusion of Cr into amorphous silicon layers [8].

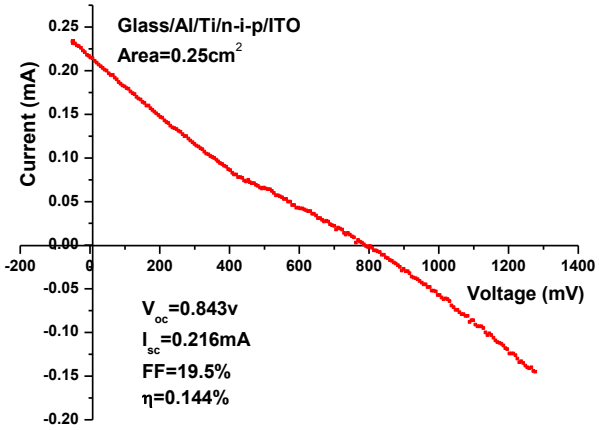

Figure 6.5. IV curve of a-Si:H solar cell on glass substrate with Titanium barrier.

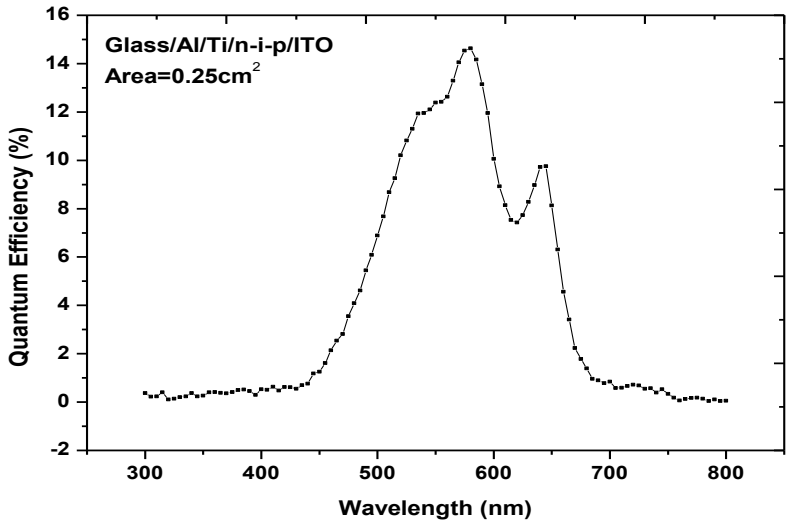

Figure 6.6. Measured external quantum efficiency (EQE) of a-Si:H solar cell on glass substrate with Ti barrier.

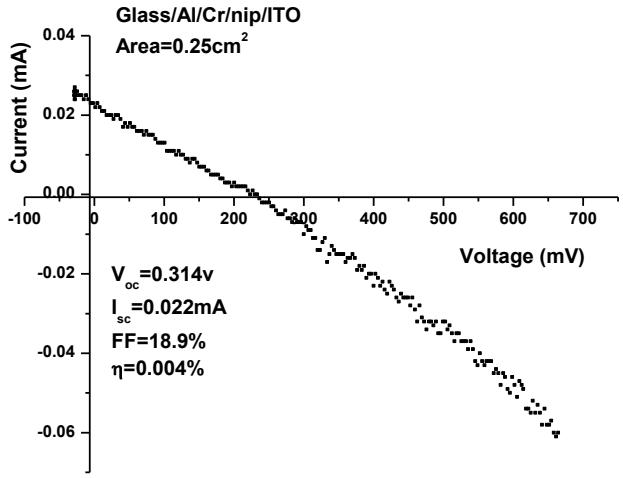

Figure 6.7. I-V curve of a-Si:H solar cell on glass substrate with Chromium barrier.

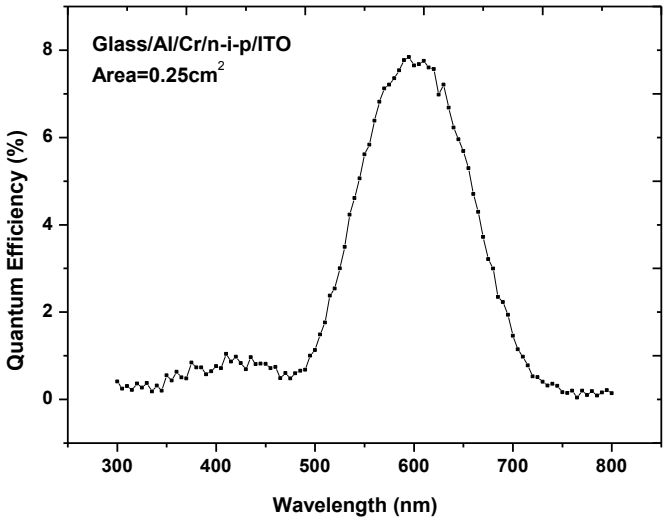

Figure 6.8. Measured external quantum efficiency (EQE) of a-Si:H solar cell on glass substrate with Cr barrier.

I-V curve of typical a-Si:H solar cells (substrate configuration) with and without ITO diffusion barrier are shown in Figure 6.9. In the case of absence of diffusion barrier, the efficiency is only around 0.005% with an open circuit voltage V_{oc} of 0.23V and short current was only 0.037 mA. These figures were improved by introducing 80nm of sputtered ITO as a diffusion barrier between the aluminium back contact and amorphous silicon configuration. The efficiency became 1.71% with an open circuit voltage V_{oc} of 0.79V and short current was around 1.15mA. Fill factor (*FF*) is improved from 0. 5% to 17.1% when the barrier layer applied. The low value of *FF* is a consequence of poor carrier collection within the structure of the cell, possibly due to high series resistance. External quantum efficiency (QE) measurements were performed on amorphous silicon cells with and without ITO diffusion barrier. QE curves of the solar cells are shown in Figure 6.10 and there is a clear increase of the QE in the 400 nm–800 nm range.

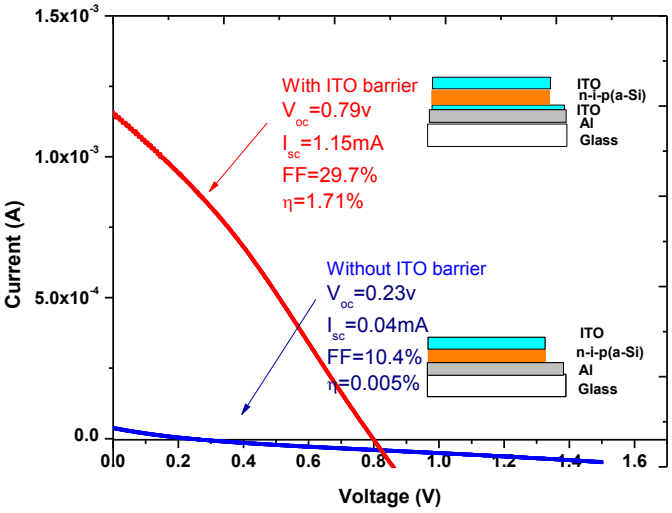

Figure 6.9. I-V curve of a-Si:H solar cells (substrate configuration) on glass substrate with and without ITO (80nm) barrier.

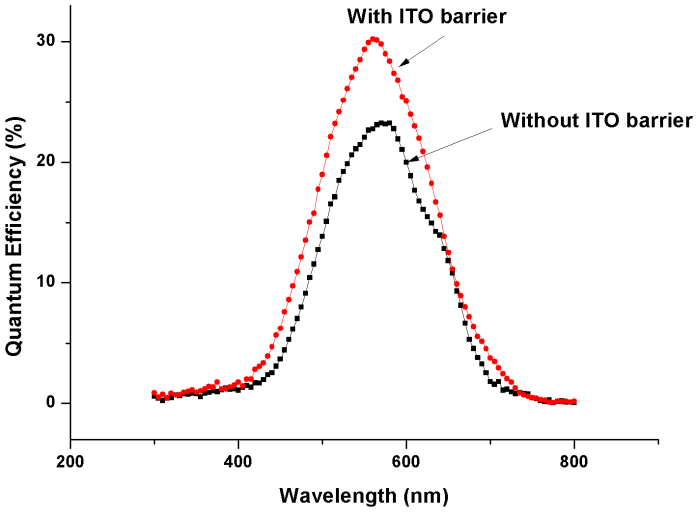

Figure 6. 10. Measured external quantum efficiency (EQE) of a-Si:H solar cell on glass substrate with and without ITO barrier.

Figure 6.11 shows *I-V* curve of an amorphous solar cell with superstrate configuration. In this case amorphous silicon is deposited onto ITO coated glass substrate and there is no need for a separate diffusion barrier. The solar cell efficiency was 1.46% and short circuit current density was 5.03mA/cm^2.

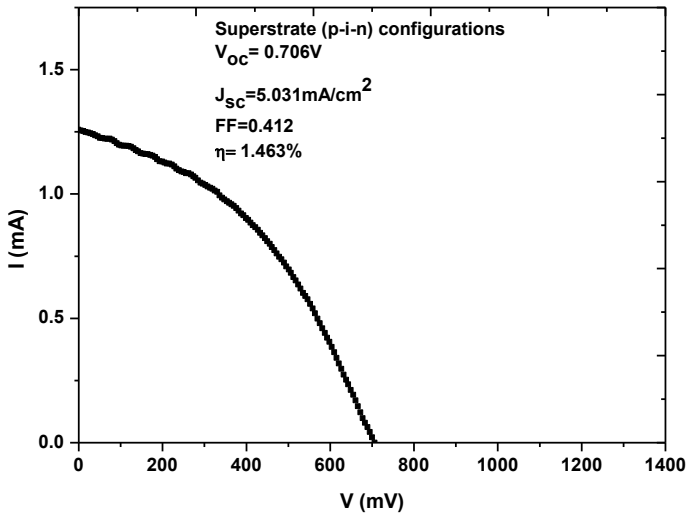

Figure 6.11. I-V curve of p-i-n (superstrate configuration) a-Si:H solar cell on glass without barrier.

6.3.1.3 Influence of the thickness of aluminium back contact on the electrical performances of the device

The results presented here are based on two sets of a-Si:H solar cells on glass substrates. In the first set, different thicknesses of aluminium layers were built as a back contact on glass substrate and then n-i-p configuration silicon deposited to form solar cells without any diffusion barrier. The aim was to investigate the influence of the thickness of the back contact on the efficiency of the cells. The thicknesses were varied from 20nm to 100nm of evaporated aluminium on glass substrate with substrate configuration. After depositing the silicon layers, ITO of around 200nm was sputtered on the configuration to form top contacts. The second set was cells built on aluminium coated glass substrate with different thicknesses of ITO diffusion barrier. The diffusion barrier thicknesses were varied from 20nm to 80nm.

Figure 6.12 shows variation of the cell efficiency with different thicknesses of aluminium back contact without diffusion barrier. The current-voltage measurements reveal that the efficiency increases as expected with increased aluminium thicknesses. This improvement of cell efficiency can be related to improved conductivity of aluminium layers. The same improvement in short circuit current with increased Al thicknesses can be seen in Figure 6.13, whereas V_{oc} was stable when the aluminium thickness reached a figure of 50nm.

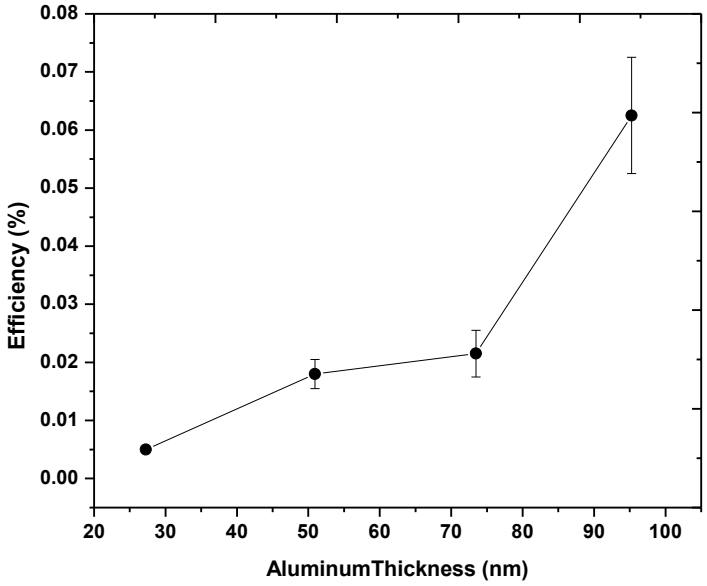

Figure6.12. Efficiency versus Aluminium back contact thickness without diffusion barrier.

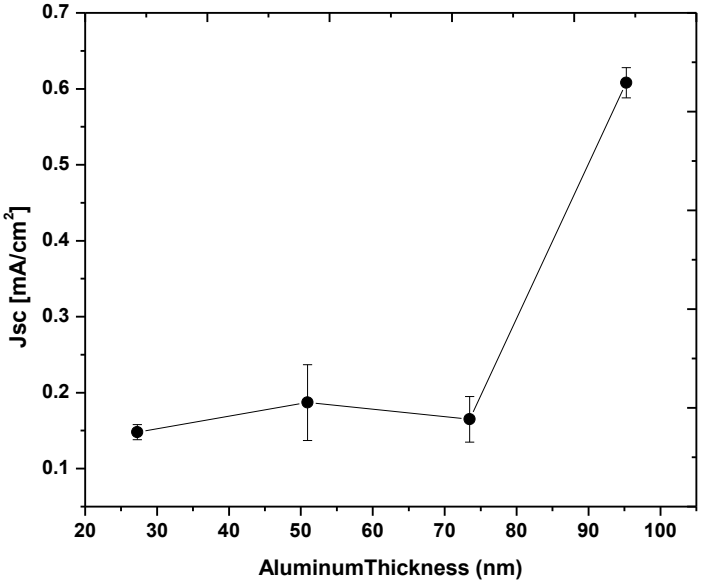

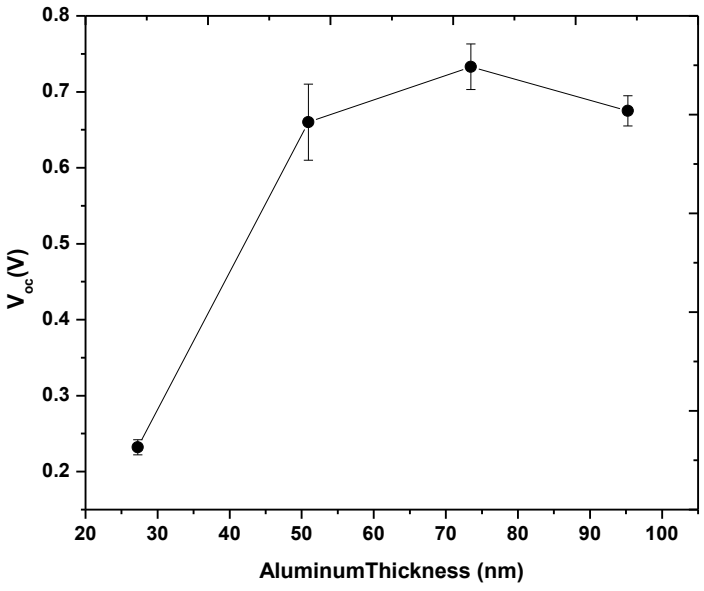

Figure 6.13. Jsc and Voc versus Aluminium back contact thickness without diffusion barrier.

Figure 6.14 shows variation of the cell efficiency with different thicknesses of aluminium back contact with ITO diffusion barrier of 21.8nm. The figure shows that the efficiency rapidly decreases with increasing Al thicknesses. Similar decreases in the fill factor observed which can be attributed to increased silicon- ITO series resistance. Figure 6.15 shows the variation of both J_{sc} and V_{oc} with increasing the thickness of the aluminium. It is clear that the thinner aluminium with ITO barrier provides the better J_{sc} and V_{oc}. This indicates that the thickness of ITO is insufficient to prevent the aluminium diffusion when the aluminium becomes thicker than 30nm.

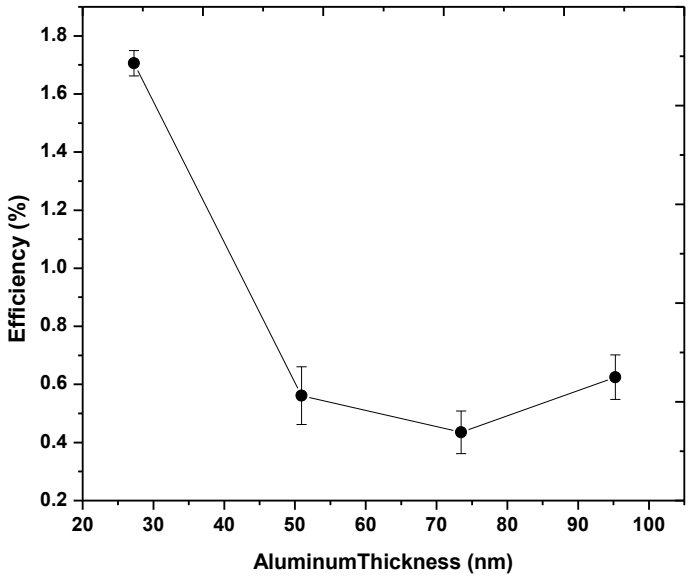

Figure 6.14. Efficiency vs Aluminium back contact thickness with ITO (21.8nm) diffusion barrier.

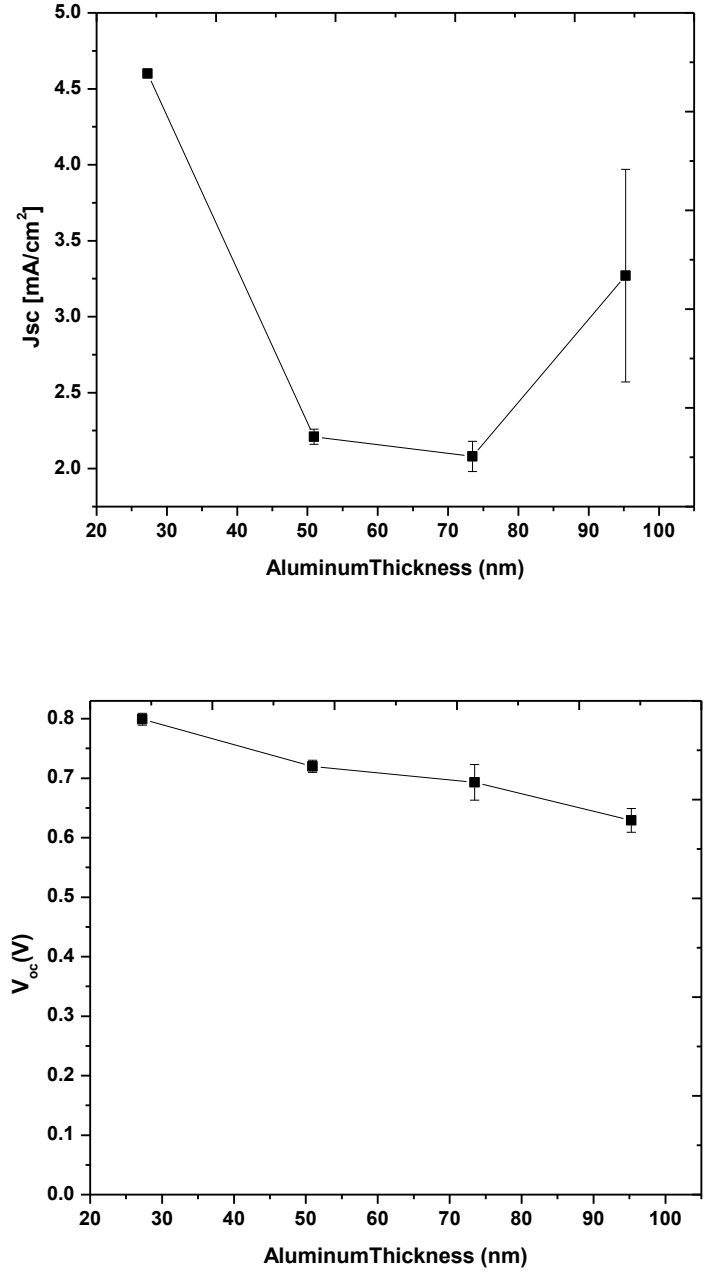

Figure 6.15 J_{sc} and V_{oc} vs Aluminium back contact thickness with 21.8nm ITO diffusion barrier.

6.3.1.4 Influence of the thickness of ITO diffusion barrier on the electrical performances of the device

A set of samples with configuration of (*Glass/Al/ITO/n-i-p/ITO*) was built in order to investigate the influence of ITO barrier thicknesses on the solar cell's performance. The thicknesses of the barrier were varied from 0 to 120nm and the effective cell area was 0.25cm^2. Thickness of the aluminium back contact was around 100nm. Figure 6.16 shows the variation of solar cell efficiency and calculated fill factor with ITO diffusion barrier thickness. It was observed that the increase in cell efficiency was rapid when the barrier film thickness increased from 0 to 80 nm, and then the efficiency decreased when the thickness was greater than 80 nm. That is the critical thickness where the ITO dominates electrically the back contact over the aluminium. Most effort was concentrated on the minimum necessary thickness of the diffusion barrier to have a maximum efficiency. Open voltage V_{oc} and short circuit density J_{sc} showed that the value of both are stable for barrier thickness above 30nm as shown in Figures 6.17 and 6.18.

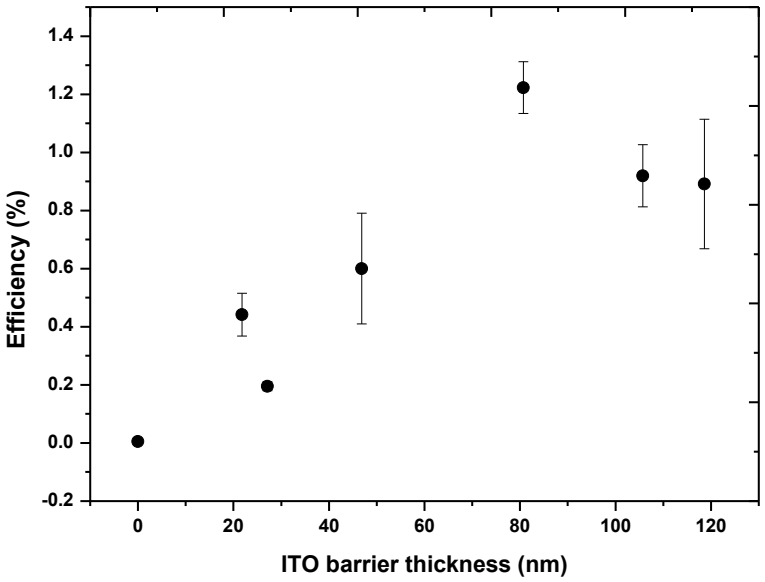

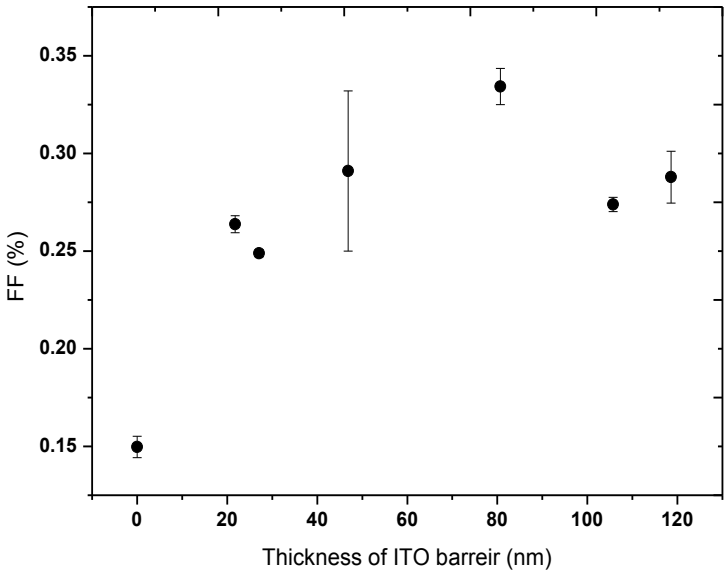

Figure 6.16. Efficiency and FF vs ITO diffusion barrier thicknesses on glass substrate.

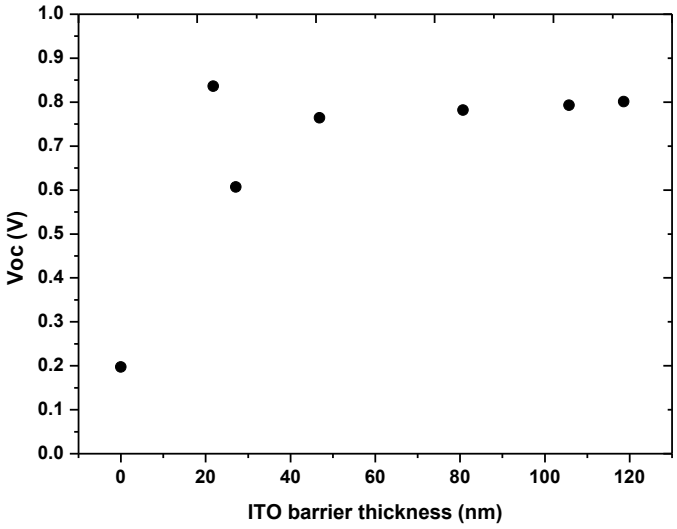

Figure6.17. Voc vs ITO diffusion barrier thicknesses on glass substrate.

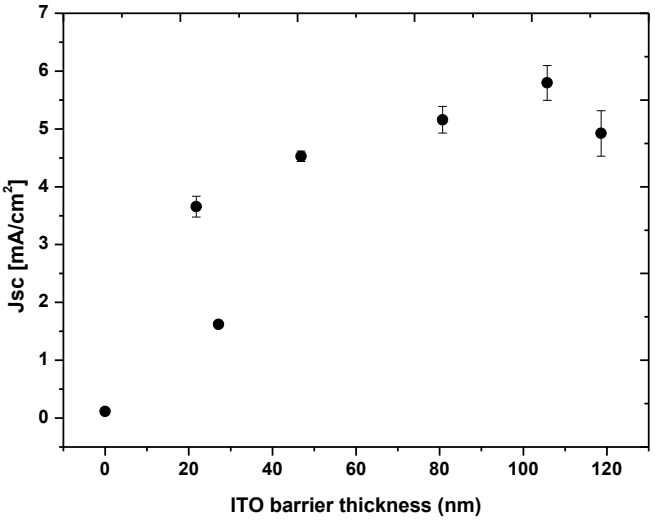

Figure 6.18. Jsc vs ITO diffusion barrier thicknesses on glass substrate.

6.3.2 Single junction a-Si:H solar cells on flexible substrate

Aluminium coated PTFE and polyester fabrics were used as a substrate to build single junction (n-i-p) amorphous silicon devices. Thin indium tin oxide (ITO) with different thicknesses was used as a diffusion barrier. The current voltage characteristics were measured under a solar simulator to study the effect of barrier thickness on the efficiency of the cells.

6.3.2.1 Cells on PTFE

In terms of examining the effect of ITO diffusion barrier thickness on the performances of the devices on PTFE fabric substrate, amorphous silicon solar cells with configuration of *PTFE/Al/ITO(barrier)/n-i-p/ITO* were built and ITO diffusion barrier thickness was varied from 21 to 120nm. Figure 6.19 shows an example of single junction amorphous silicon solar cell on PTFE fabric. Figure 6.20 shows that the efficiency of the cells increases with increasing the ITO diffusion barrier thickness. Even though the cells showed low efficiency it seems that the diffusion barrier helps to prevent aluminium diffusing into the silicon network.

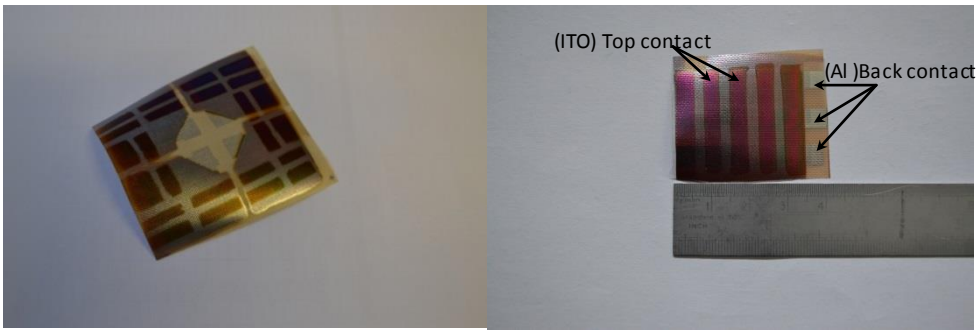

Figure 6.19. Single junction a-Si:H solar cell on PTFE fabric.

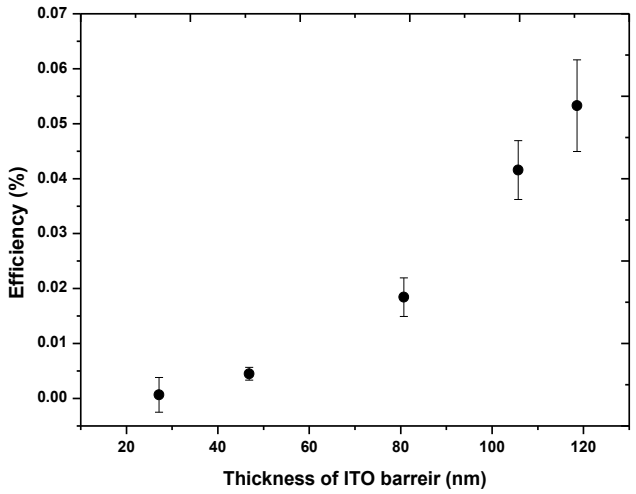

Figure 6.20. Efficiency vs ITO diffusion barrier thickness on PTFE fabric.

6.3.2.2 Cells on polyester fabric

As discussed in chapter 4, polyester fabrics were coated with PEDOT:PSS polymer and then around 100nm of aluminium evaporated to form back contacts. Amorphous silicon devices with configuration of *Al/ ITO (barrier)/n-i-p/ITO* were built onto these polyester fabrics. The thickness of ITO barrier varied from 21nm to 120nm. Figure 6.21 shows amorphous silicon cells on polyester fabrics. The variation of the efficiency of the cells with ITO barrier thickness is shown Figure 6.22. With increasing barrier thickness the efficiency showed improvement and the 80-nm-thick film shows the highest efficiency. After that there is a fall of efficiency which is attributed to increased resistance between the silicon and aluminium back contact.

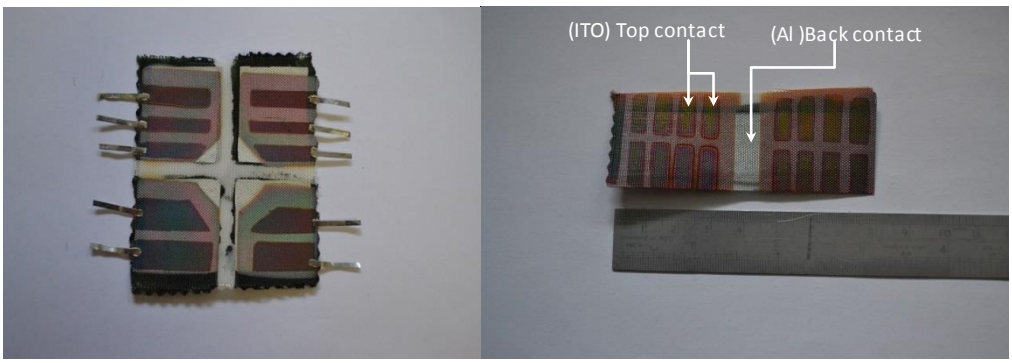

Figure 6.21. Single junction a-Si:H solar cells on polyester fabric.

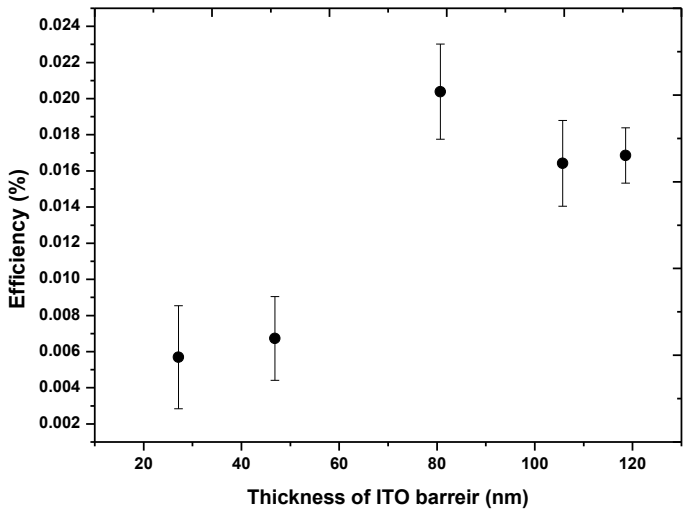

Figure 6.22. Efficiency vs ITO diffusion barrier thickness on polyester fabric.

6.3.3 ZnO as front contact

This work investigates the influence of using a different transparent conductor, namely zinc oxide (ZnO), in place of indium tin oxide (ITO) as a top contact for amorphous silicon solar cells. The ZnO was provided by University of Oxford. The TCOs were applied to glass substrates, and superstrate structures of *p-i-n* amorphous silicon were deposited by using our PECVD system. Evaporated aluminium was used as a back contact and the cell effective area was 0.25cm^2. Figure 6.23 shows single junction amorphous silicon solar cells on ITO and ZnO coated glass substrates.

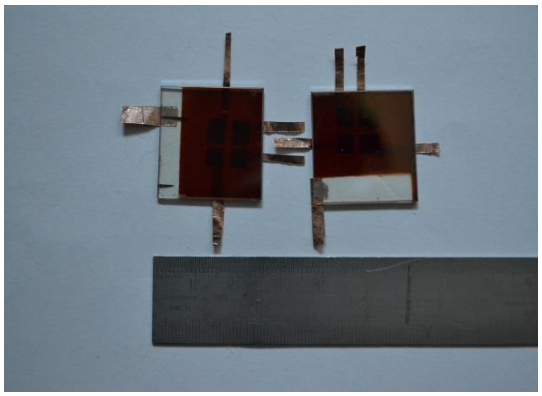

Figure 6.23. Single junction a-Si:H solar cells on ITO & ZnO coated glass substrates.

As a result, Figures 6.24 and 6.26 show *IV* curves of selected a-Si:H solar cells on glass substrate with ZnO and ITO top contact respectively. Cell with ITO top contact showed a better efficiency of 1.46% whereas the one with ZnO was 0.63%. That could be because of high resistance of ZnO as can be seen in Table 2, which summarises performance of the cells with both TCO top contacts. Measured external quantum efficiency (EQE) of a-Si:H solar cell with ITO top contact has EQE peak of about 37% whereas for the cell with ZnO top contact it was around 15% as shown in Figures 6.25 and 6.27. The two cells were found to be shunted with 0.33KΩ for ITO contact and 1.38KΩ for ZnO contact.

Table 6.2. Performance of selected cells with ITO and ZnO top contacts.

Front contact type	Front contact thickness (nm)	Front contact sheet resistivity (Ω/□)	J_{sc} (mA/cm^2)	V_{oc} (Volte)	FF (%)	η (%)	R_s KΩ	R_{shunt} KΩ
ITO	260	64.3	5.03	0.71	0.41	1.46	1.24	0.33
ZnO	240	590	2.95	0.63	0.33	0.63	0.62	1.38

V_{OC} = open-circuit voltage, J_{SC} = short-circuit current density, FF = fill factor, η = efficiency, R_s=series resistance, and R_{shunt}= shunt resistance.

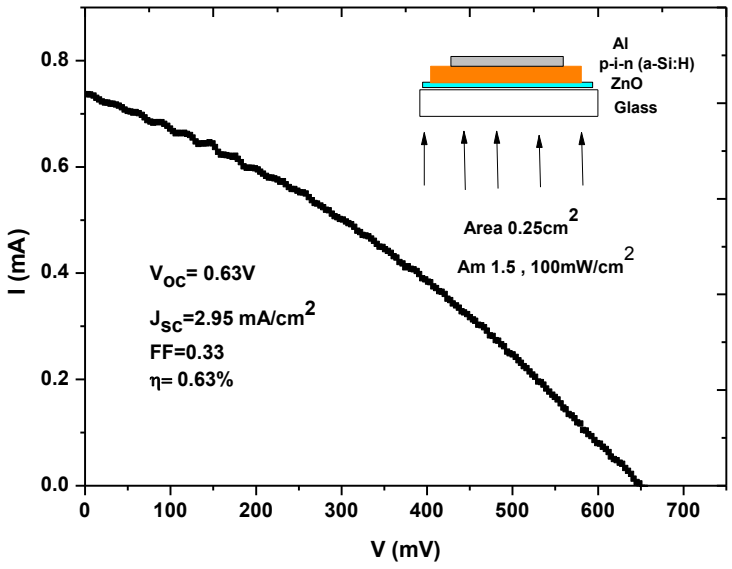

Figure 6.24. IV curve of a-Si:H solar cell on glass substrate with ZnO top contact.

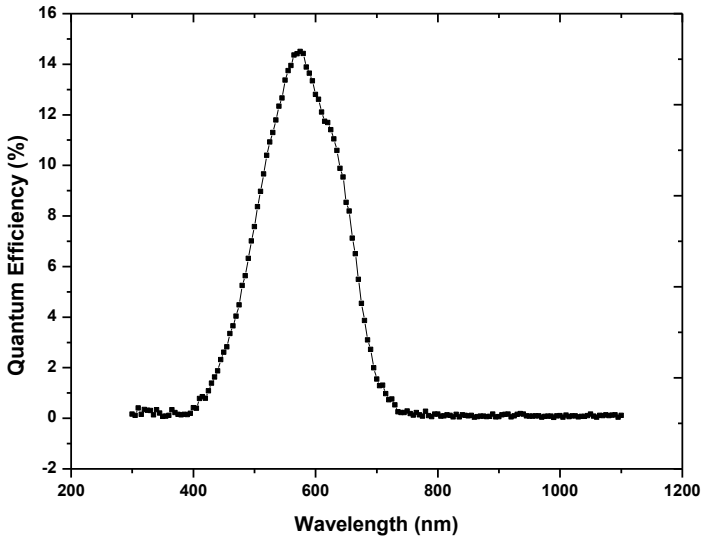

Figure 6.25.Measured external quantum efficiency (EQE) of a-Si:H solar cell on glass substrate with ZnO top contact.

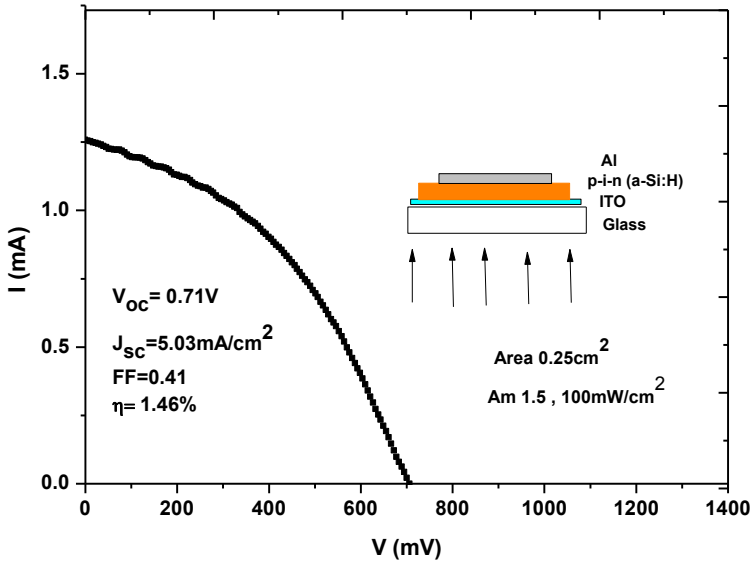

Figure 6.26. IV curve of a-Si:H solar cell on glass substrate with ITO top contact.

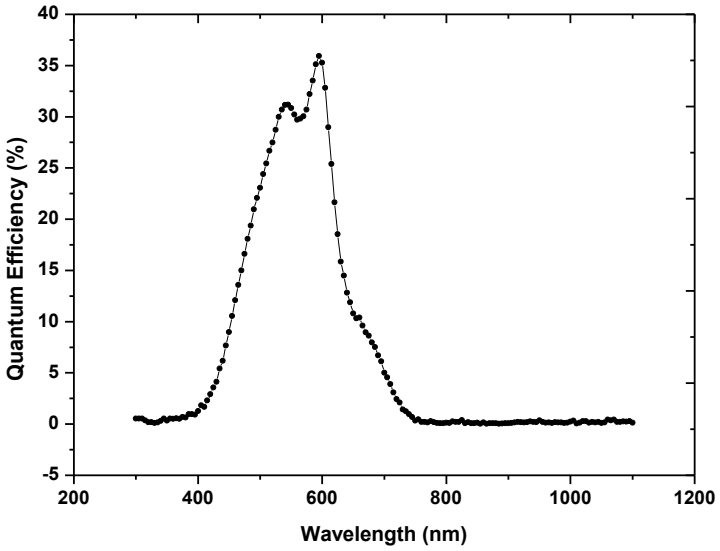

Figure 6.27.Measured external quantum efficiency (EQE) of a-Si:H solar cell on glass substrate with ITO top contact.

6.3.4 Fabrication issues

In this part we will discuss fabrication issues identified during this work which can have a big impact on the performance of the solar cells and lead to poor efficiencies of the amorphous solar cells on PTFE and polyester fabrics.

6.3.4.1 Dust and powder formation

Dust and particle growth in Silane-based plasmas is known to occur for a long time now and can be a major source of contamination in the reactor chamber [5, 6]. The particles can be larger than the film thickness which causes electrical shunts through the layers [7]. In the chamber of our PECVD system, the sample is heated to about 200^{o}C whereas the rest of the chamber remains cold during the deposition process. That helps to form dust and powder which cover the cool internal sides of the chamber. We have noticed that the dust does not stick well on the cold surfaces and can be shifted by the flowing gases toward the sample then integrated into the cell configuration. Figure 6.28 illustrates the scenario of cell shunt problem caused by a pinhole during deposition of amorphous silicon.

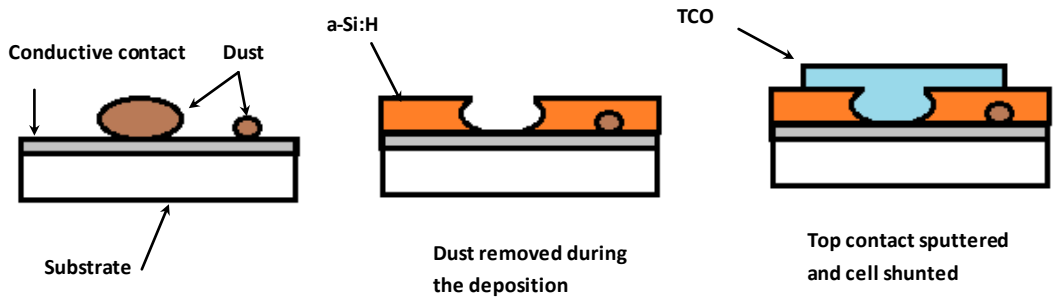

Figure 6.28. Scenario of cell shunt problem caused by a pinhole during deposition of amorphous silicon.

6.3.4.2 Bubble formation

We suggest a similar scenario when it comes to liquid coating a fabric substrate. As explained in chapter 4, polyester fabrics were coated with either Panipol or PEDOT:PSS and then a layer of aluminium was evaporated to form conductive contacts. Gas bubbles can be formed and trapped inside the polymer layer. The vapour pressure of the solvent in the polymer-solvent mixture is considered as one of the reasons for bubble formation. Moreover bubbles can be developed and grow at temperatures below the boiling point of the solvent in the polymer film [8]. Figure 6.29 illustrates the scenario suggested for bubble formation in liquid polymer coated fabrics. During plasma deposition processing, coated fabric is heated to about 200^{o}C and bubbles can be either "hatched" or "unhatched". In both cases damage in the cell structure can take place and then the solar cell would be shorted or shunted. Bubble defects can be seen by optical microscope as shown in Figure 6.30.

Figure 6.31 shows SEM images of bubble defects in an amorphous solar cell on polyester fabric. It has been observed that the degassing of the polymer solutions before coating the fabrics resulted in reduced bubble formation as can be seen in Figure 6.32.

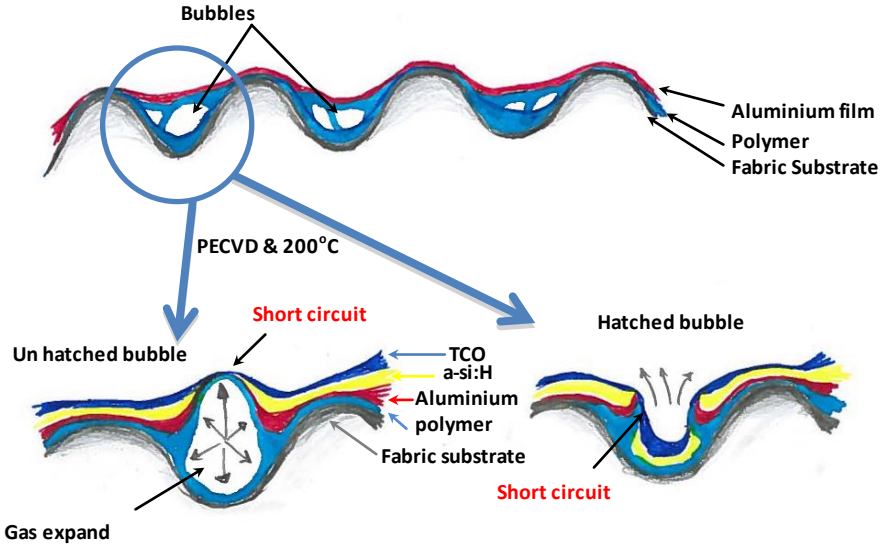

Figure 6.29. Bubble formation scenario.

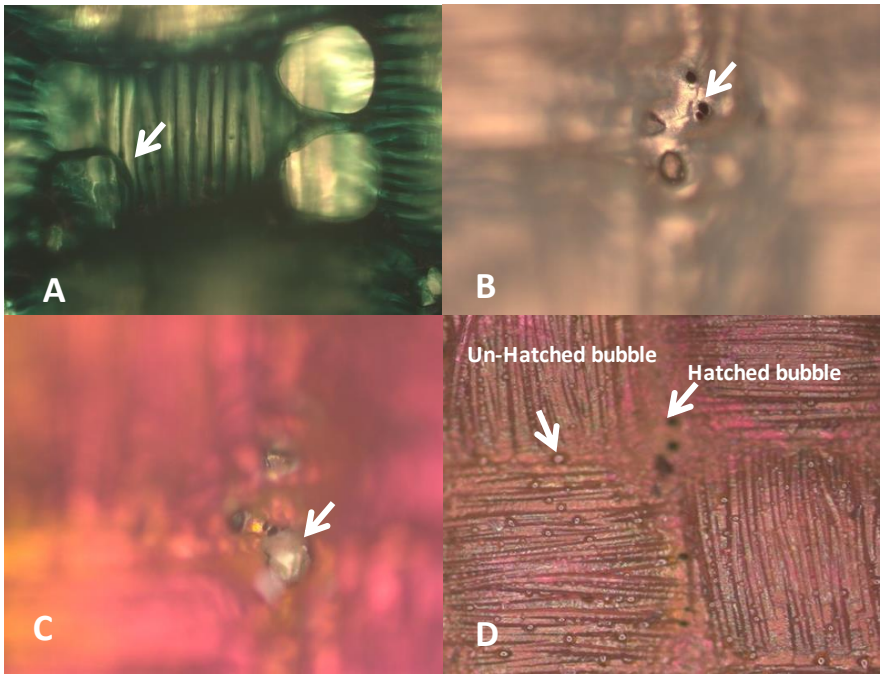

Figure 6.30. Optical micrograph of woven textile with added (A) panipol, (B) panipol/aluminium, (C) panipol/aluminium/a-Si:H, and (D) panipol/aluminium/a-Si:H/ITO.

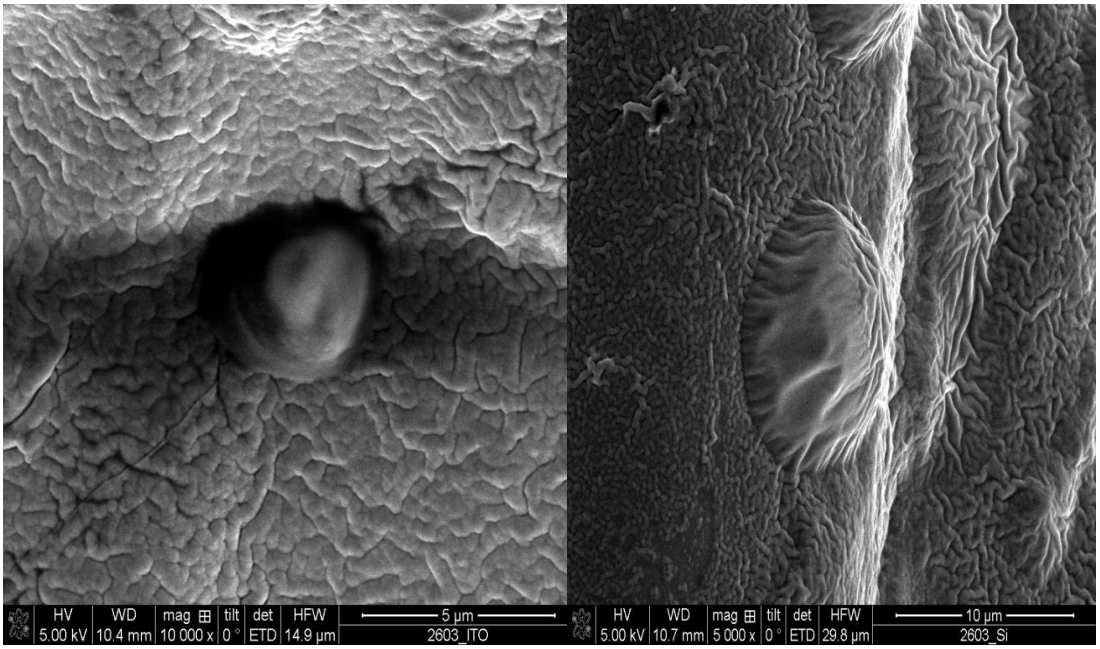

Figure 6.31. SEM images of bubble defects in amorphous silicon cell on polyester fabric.

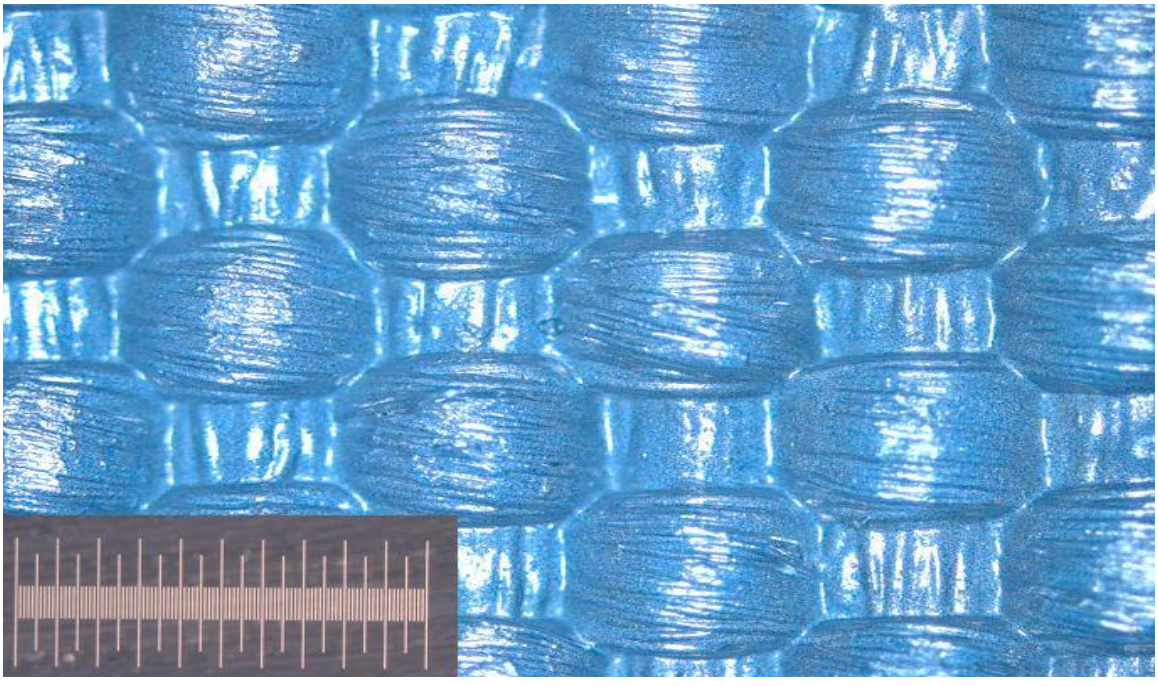

Figure 6.32. Optical micrograph of woven textile with added panipol/aluminium coating. The polymer liquid was treated with degassing process before being applied. The scale has 10 µm fine divisions.

6.3.4.3 Surface roughness

Intentional roughening of the interfaces between thin film solar cell layers is usually achieved by using rough substrates. Increasing the optical path of light propagation in the thin layers can lead to higher absorption which in turn improves the cell efficiency [9], although that increase in the roughness would tend to break up amorphous silicon layers and affect the electric field across the intrinsic layer, reducing carrier collection. It is possible that the back contact at the rough peak could shunt the cell by connecting either back and top contacts or *n* layer and *p* layer. These situations are described in figure 6.33.

As shown in section 6.2.1, flat glass, polyester fabrics and PTFE fabrics were used as a substrate to support an amorphous silicon solar cell configuration. Roughness of the surfaces is varied from smooth to rough as shown in Figure 6.1 and 6.2. The efficiency of solar cells dropped from 1.7% in case of flat substrate to 0.02% in case of polyester fabrics. This drop can be attributed to the effects of the high roughness of substrates. Figure 30 illustrates the issues that could take place due to roughness of the substrate surface. In case (*A*), high peak of back contact causes a direct short circuit between back and top contact and the cell is fully shunted. Peak (*B*) represents the case where n-layer covers the metal contact conformally and the cell is still functional with no problems. Finally as shown in (*C*), the peak of the back contact is higher than the thickness of n-layer that would possibly disable the functional n-layer and disrupt the electrical field in the location of the metal peak.

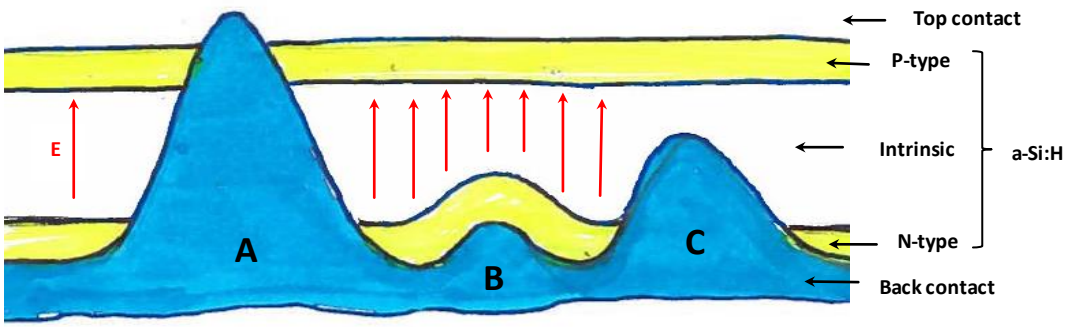

Figure 6.33. Possible defects due to substrate roughness.

6.3.4.4 Misalignment and Probing issues

Different masks were used in this work to place and form each functional layer without any overlap or interference, which would cause a short circuit or even shunt the cell. Misalignment of the masks can lead to edge shunts which are considered as manufacturing defects where the top and back contact are connected and allow current leakage [10]. Figure 6.34 shows some masks used in this work and also the structure of the solar cell on polyester fabrics.

Probing the sample by spring-loaded probes, when measuring IV characteristics, can damage the structure and cause a short circuit through the fragile layers on the top of this flexible substrate. Accordingly layers have been laid on the top of each other considering enough room to avoid edge shunts and short circuits caused by pressure of the spring-loaded probes. Some suggested structures to avoid the problem are shown in Figure 6.35. Alternatively, silver paste and conductive adhesive tape can be used but these form more permanent contacts.

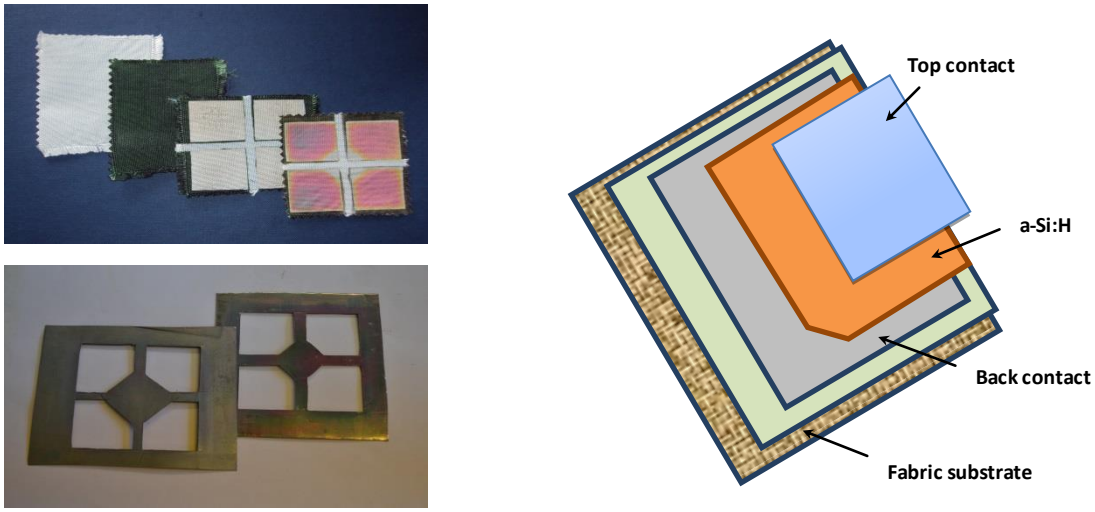

Figure 6.34. Masks and designed structure on top of polyester fabrics.

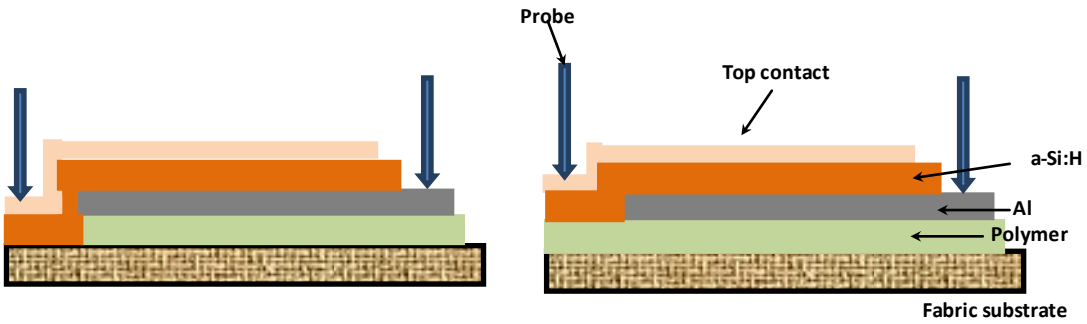

Figure 6.35.Suggested configuration to avoid short circuit problems.

6.3.4.5 Contamination and Cross contamination issues

Although using single chamber plasma-enhanced chemical vapour deposition (PECVD) offers the advantage of a low cost in comparison with multi-chamber processes equipment, phosphorus or boron contamination from the internal walls of the reactor can be a source of contamination during subsequent deposition [11]. That can degrade the performance of the solar cells. Additional cleaning cycles were considered by incorporating reactor cleaning and pumping steps after the n-type deposition to reduce part of the phosphorus cross-contamination [12].

Chamber wall and gas pipe leakage could be a major cause of oxygen and other impurities which cause a decay of solar cell efficiency. So to counter that leakage tests were performed to track any leakages in the system.

Diffusion pump oil can be a source of fluorine contamination which had been detected by using EDS as shown in Figure 6.36. To avoid that, the pumping procedure was considered by taking into account pressure balance between the chamber and diffusion pump.

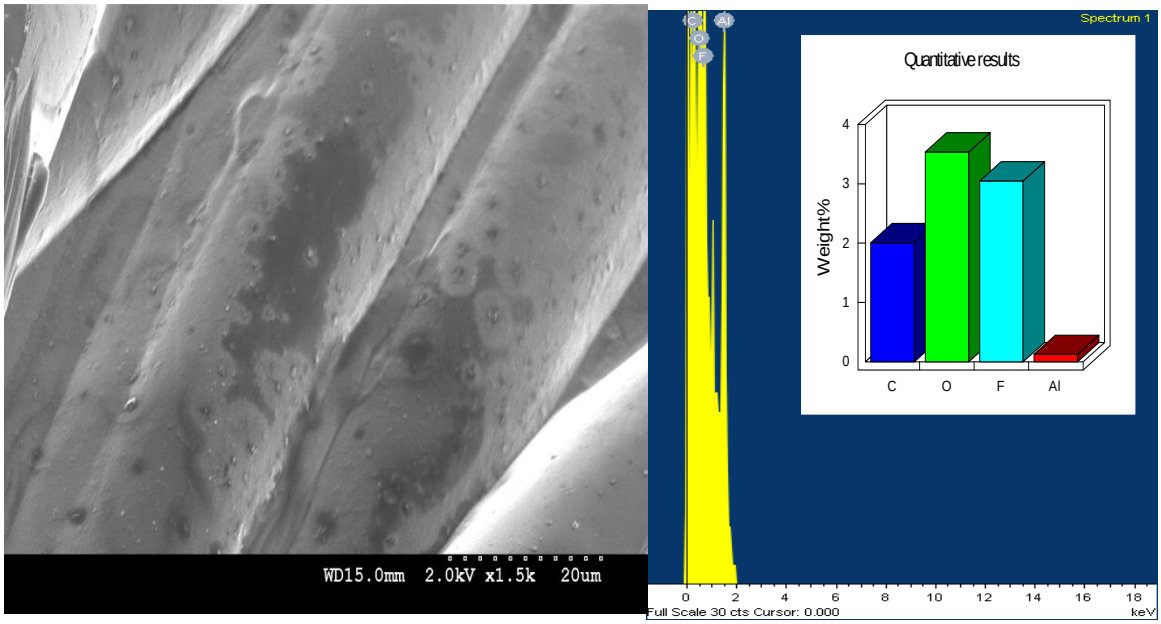

Figure 6.36. Fluorine (F) contamination on (a-Si:H/Al/PEDOT:PSS/ Polyester Fabric) detected by using EDS.

6.4 Conclusion

Single junction amorphous silicon solar cells were successfully deposited by PECVD on glass and flexible fabric substrates at a temperature of 200°C. Investigation into the electrical characterisation of a-Si:H structures, with and without a diffusion barrier of different thicknesses, was presented, as well as the influence of the thickness of aluminium back contact on the electrical performances of the devices.

Amorphous silicon solar cell structures were produced on two types of fabric substrate. In the case of substrate configuration it was found that using a thin layer of ITO as a diffusion barrier improves the efficiency of the amorphous silicon solar cell.

Diffusion of aluminium into silicon (substrate side) may have a big impact on the cell efficiency and is therefore harmful to the cell. We assume that during the plasma deposition process there is transport of aluminium atoms into the silicon network. Because of that it is very important to prevent such diffusion which can be done by using a thin conductive film.

Zinc oxide was introduced as an alternative thin conductive layer to form the top contact of the cells and was compared with indium tin oxide. Finally we discussed some fabrication issues which have a big impact on the performance of the cells and possibly lead to poor efficiencies of the amorphous solar cells on textiles.

6.5 References

1. Lind, H., Wilson J.I.B, and Mather R, *Raman spectroscopy of thin-film silicon on woven polyester*. physica status solidi (a), 2011. 208(12): p. 2765-2771.

2. Lind, A.H.N., *Deposition and Characterisation of Silicon and Conductive Layers on Woven Polyester*, PhD thesis, Heriot-Watt University Edinburgh, 2013.

3. Cai, H., et al., *Study on diffusion barrier layer of silicon-based thin-film solar cells on polyimide substrate*. Solar Energy Materials and Solar Cells, 2009. 93(11): p. 1959-1962.

4. Saunderson, J.D., R. Swanepoel, and M.J. van Staden, *The role of the ZnO buffer layer in Al/Si interdiffusion in α-Si:H solar cells on flexible substrates*. Solar Energy Materials and Solar Cells, 1998. 51(3–4): p. 425-432.

5. Cavarroc, M., et al., *Instabilities during the growth of dust successive generations in silane-based plasmas*. Physics of Plasmas, 2008. 15(10): p. 103704.

6. Roth, R.M., et al., *Spatial dependence of particle light scattering in an rf silane discharge. Applied Physics Letters*, 1985. 46(3): p. 253-255.

7. Selwyn, G.S., J. Singh, and R.S. Bennett, *In situ laser diagnostic studies of plasma-generated particulate contamination*. Journal of Vacuum Science & Technology A: Vacuum, Surfaces, and Films, 1989. 7(4): p. 2758-2765.

8. Mohammadi, R.P., *Mechanism of Bubble Formation during the Drying of Polymer Films*. PhD thesis, The Pennsylvania State University,USA,May 2005.

9. Krč, J., et al., *Analysis of light scattering in a-Si:H-based solar cells with rough interfaces. Solar Energy Materials and Solar Cells*, 2002. 74(1–4): p. 401-406.

10. Breitenstein, O., et al., *Shunt types in crystalline silicon solar cells*. Progress in Photovoltaics: Research and Applications, 2004. 12(7): p. 529-538.

11. Bugnon, G., et al., *Silicon oxide buffer layer at the p–i interface in amorphous and microcrystalline silicon solar cells*. Solar Energy Materials and Solar Cells, (0).

12. Jardine, S., *Thin Film Silicon on Textiles by Microwave Plasma Chemical Vapour Deposition*, PhD thesis, Heriot-Watt University Edinburgh, 2006,

Chapter 7. Summary and further work

7.1 Summary

The aim of the work presented in this thesis was to deposit amorphous silicon layers on polyester fabrics directly to form a flexible solar cell using plasma enhanced chemical vapour deposition. To achieve that, we divided the work into three parts. In the first part, a study was made of converting polyester fabric into a conductive substrate that was durable in terms of its electrical conductivity and flexibility as well as being able to survive harsh plasma deposition conditions. In the second part, each layer of a amorphous silicon solar cell was individually subjected to an investigation and characterisation in terms of optical and electrical properties. In the last part, information gathered about each layer was used to form solar cells on glass and flexible substrates. The results achieved and described throughout each chapter of this thesis are highlighted below.

Chapter 4 discusses the approaches to obtaining conductive surfaces on polyester fabrics by using commercially available conductive polymers, polyaniline (Panipol) and PEDOT:PSS, which could then be coated with aluminium by vacuum deposition. In this part, we managed successfully to coat polyester fabrics with the conductive polymers. To achieve this target, four important treatment stages were required: cleaning the fabrics, thermal calendaring of fabrics to make surfaces continuous across the weave sections, plasma treatment of polyester fabric to improve polymer/fabric adhesion and finally degassing the polymer to minimise bubble formation.

A comparison study between samples coated with the two types of polymers was carried out. In terms of electrical properties, the results of TLM test for Al/Polymer showed that by using PEDOT:PSS instead of Panipol, the contact resistance decreased by 200-fold. Moreover, resistance measurement during bending showed that using PEDOT:PSS enhanced the flexibility and stability of electrical contacts on the woven fabrics better than Panipol.

Real-time resistance measurements carried out in order to examine the stability of polymer-coated fabrics showed improvement and stability in PEDOT:PSS conductivity over the period of the test whereas Panipol showed the opposite.

The optimum amount of both polymers was considered but a polymer coating alone produced too much resistance in the contact for solar cells which required an over-

coating of evaporated aluminium. The configuration (fabric/polymer/metal) seems to be functional and we can confirm that these coated fabrics still possessed their former morphology and flexibility as well as electric conductivity of the polymer/metal contact.

In chapter 5, we take into our account that understanding the properties of the separate solar cell films is essential to improve its performance. Back and top contact materials as well as functional layers of a-Si:H solar cell were subjected to investigation. Aluminium was chosen as a back contact for its availability and its relatively low cost. The first step was a study of vacuum evaporated aluminium films in terms of electrical properties. The films showed improvement in electrical conductivity with increased thickness. This expected improvement is due to reduce geometrical limitation of the mean free path of the conduction electrons.

Secondly, another conductive material used in this work as a top transparent top contact was indium tin oxide film (ITO) which was built on glass substrates in order to investigate changes in layer deposition conditions to potentially improve layer quality and optimise the process. We investigated the effects of thickness, plasma power and distance between target and substrate on the properties of ITO film. The results were the following:

Effect of the Film thickness on the properties of ITO films

- A Lorentz oscillator model was applied to Variable Angle Spectroscopic Ellipsometry (VASE) measured data with more exact fits over wider spectral range especially by adding a graded profile.
- Around 80% transmittance is achieved for the range 400 to 1000 nm for samples with thickness around 122 nm which was designated as an optimum thickness: also we proved that the transparency of the film is determined by film structure and thickness.
- The band gap energy of ITO film decreased when thickness increased, which can be explained by the Burstein–Moss shift.
- The result showed a 66-fold decreased sheet resistivity of ITO films by increasing thickness from 24 nm to 270 nm

Influence of RF power on the Properties of ITO Films

- The thickness of ITO films increased dramatically with increase in RF sputtering power.
- Average transmittance over the 400 - 1000 nm optical region of ITO thin films sputtered with different RF powers was above ~86%.
- The band gap decreased with increase in RF power up to 30W.
- The minimum sheet resistivity around 100Ω/□ was obtained for the films deposited at an RF power of 90W which was considered to be the optimum power in our sputtering system.

Effect of Target to Substrate Distance

- Transparency of the ITO films increased by increasing sputter target-substrate distance and average transmittance over 400 - 1000 nm reached 98% when substrate was located at 24.7cm from the ITO target.
- The ITO films became thinner and more electrically resistive as the substrate was moved away from the target.
- Energy band gap of the ITO films decreased as the substrate was moved away from the target. It gradually decreased from 3.71 to 3.27eV as target-substrate distance increased from 6.1 to 24.7cm

Then finally intrinsic and doped layers of amorphous silicon were successfully fabricated individually and then subjected to optical and electrical tests to provide more information about their durability and functionality. The results were the following:

Intrinsic a-Si:H film

- In order to study the properties of the film using VASE, a Tauc-Lorentz model is particularly suited for the analysis of amorphous semiconductors.
- A graded simple effective medium approximation (EMA) layer of 2.7% void has been added to the model to improve the result and minimise mean square error MSE.
- There is an agreement between results obtained by using Perkin UV/VIS spectrometer and data obtained with VASE and analysed with the theoretical model.
- For intrinsic layers, optical band gap was found to be 1.73 eV and Urbach energy was 101 meV which corresponds to high level of disorder within the semiconductor material.

- The resistivity of intrinsic layer was measured to be 1.56 x10^6 Ω-m.
- It is found that the conductivity activation energy for intrinsic layer is about 0.41 eV which is smaller than expected implying defects energy levels within band gap.

Doped a-Si:H film

- The same model (graded Tauc-Lorentz) was applied on measured ellipsometric data for phosphine doped amorphous silicon films.
- By considering the theoretical model, there is a strong relation between roughness of the film and the thickness.
- Optical energy gaps were found to be 1.83 eV and 1.70 eV for n-type and p-type amorphous silicon respectively and Urbach energies found to be 73 meV for n-type and 55 meV for p-type amorphous silicon layers. That indicating a high level of disorder with in the intrinsic layer.
- The resistivity of n-type silicon was calculated to be 3.16 x10^5 Ω-m, and 41.80 x10^5 Ω-m for p-type. The resistivities are of similar order suggesting that n- and p-layers are insufficiently doped.
- It is found that the conductivity activation energy for n- and p-type was 0.18 eV and 0.32 eV respectively.

Renishaw inVia spectrometer was used to analyse the samples and 514nm laser power varied from 5% to 100%. The results showed that the increase of the laser power seems to have a significant influence on the Raman measurements. Moreover, it appears that these films showed amorphous structure. Then finally, thin film deposition parameters were adjusted and an effective cleaning procedure applied on all substrates as well as internal parts of the reactor chamber to overcome the cracking behaviour in the film.

So we could move towards combining these films to construct a functional configuration of solar cells either on glass or flexible substrates. That was the subject of *chapter 6* where we tried to test the functionality of the cells. In this chapter, three types of substrates were used; flat glass, PTFE fabrics and polyester fabrics. The surface topography of the fabrics was inspected and revealed that polyester samples have height variations of up to 100μm. More textured surface and less roughness was found when the PTFE sample was analysed and the variation found to be around 70 μm.

Three types of available material; indium tin oxide (ITO), chromium (Cr) and titanium (Ti) were used as a diffusion barrier layer between aluminium back contact and n-type a-Si:H for amorphous silicon solar cells on glass substrates. It was found that using around 80nm of ITO as a diffusion barrier in case of substrate configuration can boost the efficiency from around 0.005% (cells without barrier) to about 1.71%. This improvement can be seen in EQE as well. Also the result showed that for the cell built in superstrate configuration, the efficiency was around 1.46%. Cells with Titanium and Chromium barriers showing efficiencies of about 0.14% and 0.004% which indicates that ITO barrier gives better performance.

In case of cells with different thicknesses of aluminium back contact without a barrier, the current-voltage measurements reveal that the efficiency increases with increased aluminium thicknesses. Influence of the thickness of ITO diffusion barrier on the electrical performances of the device was determined. The result showed that the cell efficiency was increased rapidly when the barrier film thickness increased and then the efficiency decreased after the thickness reached a critical value around 80nm of ITO.

We tried to introduce alternative transparent conductive material ZnO as a top contact instead of ITO. Cells with ITO top contact showed a better efficiency of 1.46% whereas the one with ZnO was 0.63%.

Single junction a-Si:H solar cells were deposited on top of PTFE and polyester fabrics. Although the measured efficiency in general was poor, there was an improvement with increasing the thickness of ITO diffusion barrier. It is clear that the roughness of the substrate has a huge impact on the efficiency of the cells. We suggested some issues which have a big impact on the performance of the solar cells and possibly lead to these poor efficiencies:

- Dust and particles growth in silane-based plasmas is known for a long time now and could be a major source of contamination in the reactor chamber and can lead to shunt problems.
- Gas bubbles can be formed and trapped inside the conducting polymer layer and during the deposition can cause damage in the cell structure.
- It has been observed that the degassing of the polymer solutions before coating the fabrics resulted in reduced bubble formation.

- Roughness of the substrates varied from smooth to rough and can cause either direct short circuits between back and top contact or even disable the functional n-layer and disrupt the electrical field.
- Misalignment of the masks can lead to edge shunts which are considered as manufacturing defects.
- Probing of the sample by spring loaded probes, when measuring IV characteristics, can damage the structure and cause a short circuit through the fragile layers on the top of flexible substrates.
- The disadvantage of using a single chamber to fabricate amorphous silicon solar cells is that phosphorus and boron contamination from the internal walls of the reactor can be a source of contamination during deposition of other layers. That in turn leads to poor quality of amorphous silicon layers.
- Leakage in the PECVD system could be a main cause of oxygen and other impurities which causes a decay of solar cell efficiency.
- Diffusion pump oil can be a source of fluorine contamination which required an extra pumping procedure to be considered.

This work has highlighted the challenges and lots of problems related with manufacturing and characterising solar cells on textiles. It is certain that there is always room for more experimental work in order to gain improvements. Despite these technical limitations, amorphous silicon solar cell layers have been fabricated on woven polyester for the first time.

7.2 Future Work

Referring to conductive surfaces on polyester fabrics, as were successfully obtained and discussed in chapter 4, these can be used in other applications such as sensors, transistors, organic solar cells or any different smart textiles applications.

Considering the result in chapter 5 related to the quality of amorphous silicon films, more work is needed to improve the effectiveness of the doping for both n and p types. That can be done by increasing the gas doping ratio of phosphine and diborane in hydrogen, as the silane flow rate for doped layers is already low. Alternatively, trimethylboron (TMB) gas should be assessed as a p-type dopant source instead of diborane gas for higher doping efficiency.

Due to diffusion problems between amorphous silicon and evaporated aluminium back contacts some improvement in solar cell efficiency was seen by using a thin diffusion barrier layer (see Figure 6.9). However, it is obvious that work is needed to fully overcome this problem either using different metal contacts or using a higher quality diffusion barrier. The conductive material used as a top transparent contact was ITO, which showed higher resistance than may be attained by other practioners. That will affect the electron collection mechanism for cells generating more current than at present. It will be necessary to consider higher quality ITO films or even an alternative TCO in future work.

In terms of characterisation techniques, there are many ways to analyse the structure of amorphous silicon films other than those mentioned in this thesis. As an example, films can be characterised by atomic force microscopy (AFM) to get more information about the surface and defects. There are many different techniques to analyse solar cells and their defects. One of those is lock-in thermography (LIT) to get a better view about pin holes and edge shunts or any other failures in the cells.

The roughness of the back contact surface is supposed to enhance light trapping which in turn improves the solar cell efficiency, especially for thin-film cell types. However in the case of polyester woven fabrics with high levels of roughness, using substrates with less roughness or even sheets of polyester could lead to improvement in the cell performance, which needs to be investigated. Non-woven fabrics with different surface structure could be used alternatively as a substrate for inorganic solar cells.

More work is required to reduce contact resistance between silicon-silicon layers or even silicon-conductive material layers. That in turn allows us better understanding of

interface properties in between solar cell layers and could lead to improving the efficiency of the cells.

It is important to consider a non-destructive electrical probing technique such as a conductive type and mercury probes. Sharp spring loaded probes are known to cause damage on the sample during electrical measurement.

Inspection of the plasma reactor shows that after a few depositions of amorphous silicon, dust has formed on cold reactor parts. That could be reduced by heating the internal parts of the reactor. At least heating both the upper and lower electrodes together can avoid trapping particles in the interelectrode space.

During the n-layer deposition for n-i-p solar cells, phosphine doped material covers the reactor walls. Then during the subsequent i-layer deposition, that may be incorporated into the intrinsic layer. So an extra purge process has been needed to avoid such cross contamination. A single chamber process for thin film solar cells can be economically preferable compared to multi chamber deposition process, but using a multi chamber process can overcome the cross contamination problems although at significant extra cost.

To achieve the desired power to operate any load does require several solar cells to be electrically connected and encapsulated as a module, so work is needed on interconnections between cells on the same substrate. Role to role processing technique can be adopted on a laboratory scale to allow depositing solar cell configurations with different conductor patterns on to a rolled polyester fabric substrate. Masking will be required to define the individual cells and their interconnection.

Appendix A. Product data sheets

A.1. PEDOT:PSS

Heraeus

CONDUCTIVE POLYMERS DIVISION

Number 81076210
Issue 2010-12-22

CLEVIOS™ PH 1000

Chemical Formula

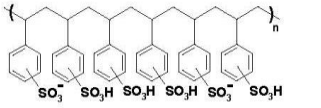

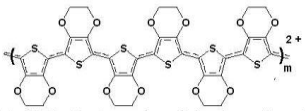

Poly(3,4-ethylenedioxythiophene)-poly(styrenesulfonate)

Description of Product Aqueous dispersion, blue liquid.

Synonyms / Abbreviations PEDT / PSS, PEDOT / PSS

Physical Characteristics[1]

	Min		Max	Unit
Solid content	1.0	-	1.3	%
Specific conductivity*	850			S/cm
Viscosity	15	-	50	mPas

*After the addition of 5% Dimethyl sulfoxide. Measured on the dried coating.

Technical Data (guide values, not a specification)

Form	liquid
Odour	odourless
Colour	dark blue
PEDOT:PSS ratio	1:2.5 (by weight)
pH	1.5 – 2.5 at 20°C
Density	1 g/cm^3 at 20°C
Boiling Point	approx 100°C

1) Information on test methods is available on request.

1/2

Storage and Handling **Avoid freezing!**

Storage and handling are subject to the rules and regulations in the country of use. When stored at temperatures between 5°C and a maximum of 10°C, CLEVIOS™ PH 1000 will remain stable for 9 months from date of production in sealed original containers. After opening the containers must be well closed to prevent the evaporation of water which may result in the formation of a non re-dispersible film. The product is sensitive to frost and should therefore not be stored at temperatures below 5°C. The product cannot be used if it has been frozen.
Brief heating to max. 50°C has no adverse effect on product properties.

Hazards identification See material safety data sheet.

Documentation An inspection document in accordance with EN 10204 is supplied with every commercial order. Inspection documents for samples are supplied on request.

Contact john.bayley@heraeus.com
Phone: +49 214 30-26718, Telefax: +49 214 30-56284

Note: **PRELIMINARY SPECIFICATION** (The product described is still under test. Amendments of all technical data are possible. Special care has to be taken while processing.)

Heraeus Clevios GmbH
CHEMPARK Leverkusen
Building B 202,
51368 Leverkusen/Germany
Phone +49 214 30-1, Fax +49 214 30-56284

A.2. PanStat W

TECHNICAL PRODUCT INFORMATION

PanStat W

Electrically Conductive Coatings and Inks

PanStat W

0107

PanStat W is a series of electrically conductive, water based ink and coating compositions. PanStat W utilises the patented Panipol® inherently conductive polyaniline technology. The coatings are permanently conductive at the optimal ESD protection range and the conductivity is independent of the humidity. The PanStat W coatings are also thermoformable and they withstand ultrasonic washing, as well as moderate mechanical wear. Due to the very low ionic migration, PanStat W offers possibility to make transparent ESD and antistatic coatings for electronic packaging and clean-room applications

Main features:

- Permanent antistatic and ESD coating
- Good stability
- Very low ion content (SO_4^{2-}, NH_4^+ and Cl^- <2 µg/g)
- Substrates: PET, PVC, PS, PC, PE, cardboard and more
- Appearance: green liquid or paste
- Colour: Translucent with greenish tint
- Thermoformable

	Method	Units	Value
Viscosity	DIN cup #4	s	10-100
Surface resistance	IEC 61340-5-1	Ω	10^8-10^9
Static decay time	IEC 61340-5-1	s	0.1-0.2

Usage:

Viscosity, adhesive properties and surface resistivity of the PanStat W coatings can be tailored in a wide range according to the application. The coatings can be applied by utilising standard printing and coating methods: flexo, reverse gravure, roller coating, bar coating, dip coating and spray coating. PanStat W is based on water (no added solvents) and therefore it can be diluted with pure water if needed.

Typical applications:

- Thermoformed electronics packaging
- Heat sealable antistatic and ESD packaging
- ESD protection tapes
- Antistatic and semi-conductive plastic films
- Applications that require permanent conductivity
- Antistatic applications that require high transparency
- Any applications that require semi-conductive properties

PanStat W can be applied as a permanently antistatic, transparent coating for plastic packaging.

PANIPOL OY
P.O. Box 163
06101 Porvoo
FINLAND

Tel. +358 207 432 255
Fax +358 207 432 250
info@panipol.com
www.panipol.com

PANIPOL
INHERENTLY CONDUCTIVE POLYMERS

TECHNICAL DATA SHEET

PANIPOL® W

0107

PANIPOL® W is water based electrically conductive polyaniline dispersion for coating formulations. PANIPOL® W contains inherently conductive polymer polyaniline, manufactured using proprietary production technology of Panipol Ltd. PANIPOL® W can be applied to produce thin, transparent coatings with controllable surface resistance in the optimal ESD protection range of 10^5 - 10^9 Ω. Coatings based on PANIPOL® W are transparent with greenish tint.

Main features:

- Polyaniline paste for permanently antistatic coating formulations
- Adjustable viscosity and conductivity
- Low ion content in the coating
- Substrates: plastic films, textiles, paper, cardboard, glass and more
- Coatings based on PANIPOL® W are thermoformable

Appearance	Dark green paste
Classification	Polyaniline salt, CAS Number 159996-80-2 Solvent: Water
Solid content	Maximum 6 %
Conductivity	Typical ESD formulations: Maximum 10^{-5} S/cm
Viscosity	18 Pa s
pH	2.5
Compatible resins	Various resin and binder systems (please contact Panipol technical service)
Storing	Store in cool and dry place, avoid direct sunlight
Shelf life	12 months in the closed bottle when properly stored
Warnings	X_i (polyaniline salt)

Usage:

PANIPOL® W can be used as an active component in conductive coating formulations:

Dilutant	Water
Binders	Please contact Panipol technical service
Coating methods	Flexo printing, screen printing, roller, bar, dip coating and other printing/coating methods

Typical applications:

- Antistatic and ESD protection coating formulations for electronics packages
- Thermoformable antistatic coating formulations
- Electrically conductive ink formulations for printed electronics
- Any other applications that require permanent semi-conductive properties

PANIPOL OY
P.O. Box 163
06101 Porvoo
FINLAND

Tel. +358 207 432 255
Fax +358 207 432 250
info@panipol.com
www.panipol.com

PANIPOL
INHERENTLY CONDUCTIVE POLYMERS

TECHNICAL DATA SHEET

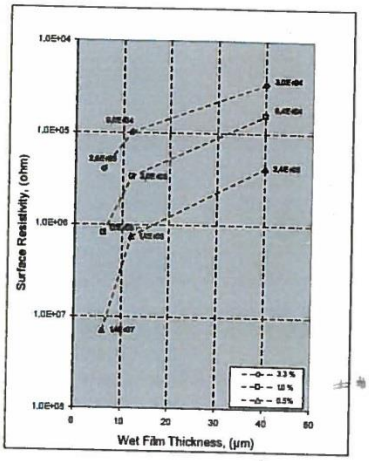

Above: PANIPOL® W dispersion in water.

Left: Electrical conductivity of PANIPOL® W as a function of film thickness at different polyaniline concentrations.

Typical properties of the coating based on PANIPOL® W with binders (PET film, 2.5% polyaniline concentration, bar coating, 12 µm wet thickness):

Property	Method	Units	Value
Surface resistance	IEC 61340-5-1	Ω	10^5
Static decay time	IEC 61340-5-1	s	0.1-0.2

PANIPOL OY
P.O. Box 163
06101 Porvoo
FINLAND

Tel. +358 207 432 255
Fax +358 207 432 250
info@panipol.com
www.panipol.com

Appendix B. Solar cell on textile fabrication process

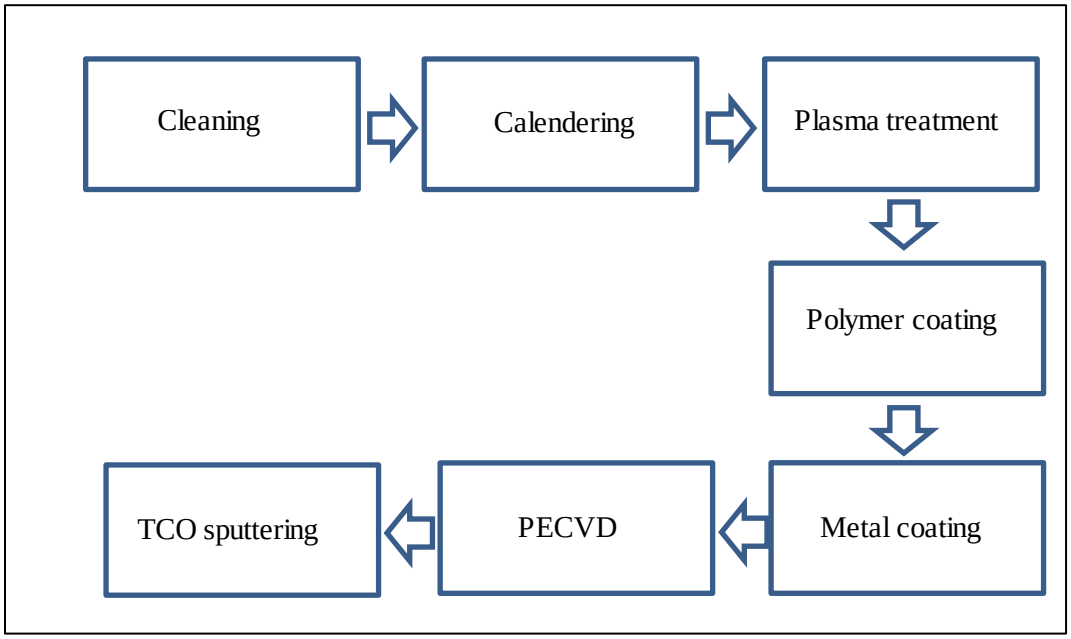

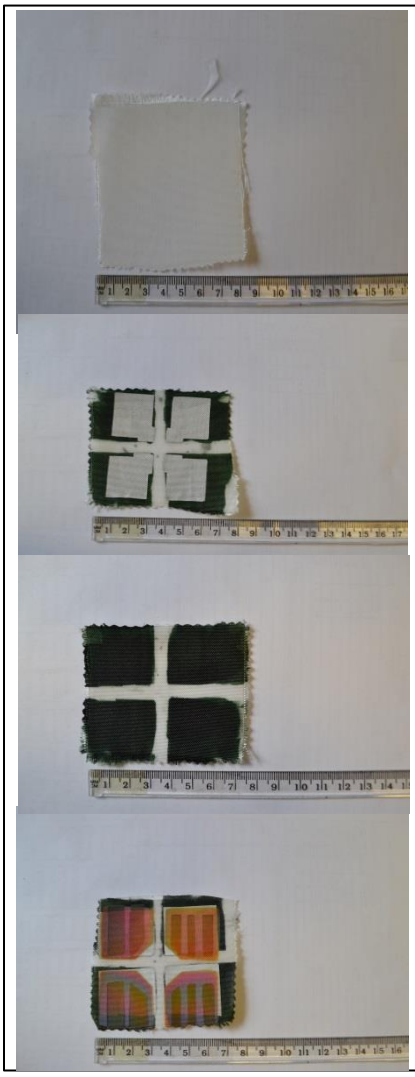

The polyester fabric samples were placed in a solution of 1% detergent (Decon) in deionised water for 30 minutes in an ultrasonic bath. Then the samples were rinsed in running (deionised) water for about 15 minutes before being dried in a flow of hot air.

Calendering process was carried out using a Roaches single head, large plate 8"x8" heater where the textile sample was placed between two plates at about 240^{o}C. Than Low pressure plasma treatments were performed in plasma deposition chamber at room temperature.

A wet coat process was used for a conductive polymer on a laboratory scale using knife to table technique.

Around 100nm of aluminium was evaporated on the polymer coated sample using an Edwards E306A vacuum evaporator and tungsten filament. The base pressure generally used in this work was about 10^{-6} mbar

n-i-p configurations of (a-Si:H) were made onto Al/polymer coated fabrics using PECVD system.

To form top contacts, ITO films were deposited by RF sputtering using an Edwards AUTO 360 system.

Appendix C. Vacuum process procedures

C.1. RF- Sputtering process

Edwards Auto 306 RF Sputter Coater

1. Switch on the main, turn to 1.

2. Check that the "Water Cooling" and "Control Cabinet" green interlock lights are ON.

3. Switch on Argon supply at the wall and make sure the Nitrogen supply is on.

4. Vent the chamber (press *Seal* and then *Vent*). Then open the chamber and place targets in the RF magnetrons.

5. Place the sample in the chamber and close the door.

6. Push *Cycle* which starts to seal to vacuum of $1.3x10^{-6}$ mbar. That takes around 2hours.

7. Switch on the RF generator and matching box.

8. Push *Process* button, use the argon needle valve set pressure to $6x10^{-3}$ mbar.

9. Push *ON* button in RF generator to trigger the plasma and adjust the power required for the radio frequency. Set to Auto mode.

10. Sputtering process start by opening shutter. Timing should start.

11. When time is reached close the shutter and close Argon supply.

12. Press *Cycle* and leave the system for around an hour and then push *Vent* to open the chamber.

13. As soon as the chamber opened press *Seal* and *Stop*. Switch off machine by turn to 0.

14. Take sample out. Close chamber, Start power and push *Cycle*. With this process ended.

C.2. Evaporation

Edwards E306A Thermal Evaporator

1. The initial state of the system should be: Diffusion and Rotary Pumps *ON*, "*Air Admit*" off and chamber pressure below 10^{-2} mbarr.

2. Break the chamber vacuum by pressing *Air Admit* ON. When chamber reaches room pressure, remove the shield, the lid, and then the glass. Turn *Air Admit* off.

3. Load the target substrate onto the target plate and the sample. Position the shutter so that the target substrate is shielded from the metals to be evaporated. Return the glass, lid, and shield.

4. Turn the lever to *Roughing* and leave to pump down for around half an hour.

5. Turn lever to *Backing*.

6. Turn lever to *Open*. This will engage the diffusion pump.

7. Fill the trap with liquid nitrogen.

8. Set the film thickness monitor with: Acoustic Impedance and Density of the metal to be evaporated.

9. Make sure the current control is set to zero, then press *Reset* and *LT* to ON.

10. Increase the current till source metal begins to melt, stop increasing the current.

11. Press Start on the thickness monitor, then open shutter to begin aluminium deposition.

12. When the desired thickness is reached, close the shutter, press *Stop*, and slowly reduce the current. Press the "Trip" button.

13. Turn off *LT* and turn handle to *Backing*. Push *Air Admit* and open the chamber. With this process ended.

Appendix D. Deposition process form.

Process Run:			Date:			
Sample Quality:			Supplier Code:			
Supplier Name:						
Purges of Carrier Gas/ Cold	Before					
Purges of Carrier Gas/ Hot	Before					
Purges of Carrier Gas/ Hot	After					
Purges of Regulator/ ( )	Before			After		
Purges of Regulator/ ( )	Before			After		
Purges of Regulator/ ( )	Before			After		
Purges of Regulator/ ( )	Before			After		
Flow Meter setting (sccm)/ Gas	( )	( )	( )	( )	( )	( )
Flow Meter (sccm)/ Zero Level						
Flow Meter (sccm)/ Target Rate						
Flow Meter (sccm)/ Total Rate						

Process Parameters During the Run

Layer On/ Off	Time (min)	Temp- erature/ °	Valve Angle/ °	Reflected Power/ W	Forward Power/ W	Heat Power/ %	Pressure (mbar)	*Plasma Condition

* S= Stable Plasma/ SF= Slight Flickering/ VU= Very Unstable/ O&O= Plasma On and Off.

Comments regading process, see back of the sheet.

Appendix E. Publication List
E.1. Poster Presentations

1. EPS Poster Event for PG Research student, 5 October 2011. Heriot-Watt University, Edinburgh.
2. Second Annual SU2P Symposium 28th and 29th March 2011. University of St Andrews, St Andrews.
3. New Generation: Powering the Future, 2 February 2011. Heriot-Watt University, Edinburgh.
4. SISER Workshop on Solar Thermal and PV Systems. July 2012. Napier University, Edinburgh.
5. APEX Excitonic Solar Cell Symposium. June 2012. Heriot- watt university, Edinburgh.
6. 3rd Vacuum Symposium UK . Coventry October 2012.
7. SISER meeting in St Andrews University October 2012.
8. SISER Workshop on Thin Film PV, March 2013, at the Thin Film Research Centre at the University of the West of Scotland, Paisley, Scotland.
9. The 9th Photovoltaic Science Application and Technology (PVSAT-9) April 2013, Swansea University, Swansea, Wales.
10. Printed Electronics Europe 2014, 1st-2ndApril 2014, Berlin, Germany.

E.2. Papers and conferences

1. **Diyaf. A**, Mather. R, and Wilson. J.I.B, *Contacts on Polyester Textile as a Flexible Substrate for Solar Cell*, PVSAT-9, Proceedings, editors M. G. Hutchins, A. Cole, T. M. Watson pp119-122 (Swansea, 2013).

2. Wilson. J.I.B, Mather. R, Lind. H and **Diyaf. A**, *Flexible solar cells on textiles*. Modern Energy Review, 2012. 4(1): p. 66-68.

3. **Diyaf. A**, Wilson. J.I.B and Mather. R, *Fabricating Robust Electrically Conductive Coatings for Solar Textiles*, International Conference: Advances in Functional Textiles, July 2013, Manchester. UK.

4. Wilson. J.I.B, Mather. R, Lind. H, and **Diyaf. A**, *Development of Flexible Solar Cells on Fabrics*, Energy Learning, 2013, www.energy-learning.com.

5. **Diyaf. A**, Mather. R, and Wilson. J.I.B, *Contacts on Polyester Textile as a Flexible Substrate for Solar Cell*, IET Renewable Power Generation, Manuscript ID: RPG-SI-2013-0236, Accepted 04-Feb-2014.

6. Zhang.Z, He.Z, Liang.C, Lind. H.N, **Diyaf. A**, Peng.Y, and Wilson J.I.B, *A preliminary development in hybrid a-silicon/polymer solar cells*. Renewable Energy, 2014. 63(0): p. 145-152.

7.Peng, Y., He, Z., **Diyaf, A**., Ivaturi, A., Zhang, Z., Liang, C. and Wilson, J.I.B., *Manipulating hybrid structures of polymer/a-Si for thin film solar cells*. Applied Physics Letters, 2014. 104(10)